NTNU – Trondheim
Norwegian University of
Science and Technology

Well Log and Seismic Data Interpretation

Rock Physics Study of Poorly Consolidated
Sandstones in The North Sea

Walter Roye Taju Fanka

Petroleum Geosciences
Submission date: June 2012
Supervisor: Per Åge Avseth, IPT

Norwegian University of Science and Technology
Department of Petroleum Engineering and Applied Geophysics

THE NORWEGIAN UNIVERSITY OF SCIENCE AND TECHNOLOGY

Rock Physics Study of Poorly Consolidated Sandstone in The North Sea

A Thesis Presented to The Department of Petroleum Engineering and Applied Geophysics, Norwegian University of Science and Technology in Partial fulfilments of the Requirements for the Master of Science Degree

By Walter Roye Taju FANKA

Supervisor: Per Avseth

10th of June 2012

Table of Content

ABSTRACT

We use rock physics models for poorly consolidated rocks to diagnose reservoir sandstones in the Alvheim Field, North Sea. Geological factors that will control the rock physics and seismic properties include clay content, sorting, diagenesis, mineralogy, and bedding configuration. The various geologic factors will affect the fluid and stress sensitivity in these rocks. We investigate the interrelationships between various geological factors and seismic fluid and stress sensitivity, by combining well log data and rock physics models. Finally, we determine inter-well characteristics in terms of varying geological factors at different locations and discuss the results in terms of expected seismic signatures in the area.

Three wells have been considered for this study but only one well has been studied in detail. Most of the logs are good and in one of the wells, the Greenberg and Castagna empirical relation has been applied to predict shear wave velocity. Two of the wells are from the Alvheim Field and the third well is from the Fram Field with both fields being of the North Sea.

The models that have been applied for this study are mainly the constant cement model (Avseth et al., 2000), the contact cement model (Dvorkin et al., 1994), and the modified Hashmin – Shtrikman bounds plus the Hertz – Mindlin theory. The over-prediction of the shear modulus by the Hertz-Mindlin theory is adjusted by applying a slip-factor correction. The Gassmann fluid substitution has been used to predict the dependence of seismic velocity and impedance on pore fluids as rock modulus changes when the pores are filled with different fluids.

One of the most powerful tools employed in this study, is the P – wave to S – wave velocity ratio, Vp/Vs, which has shown a remarkable sensitivity to both fluids and lithology. We use combinations of this with other parameters to determine possible geologic trends. One of such combinations, is the classical rock physics template (RPT) first presented by Ødegaard and Avseth (2003), of acoustic impedance versus Vp/Vs. With this tool, we have been able to identify up to 5 geologic trends which are fundamental aspects in reservoir characterization.

The results of this study shows that for the same lithology found in different areas, the geologic trends may vary considerably. These changes also have significant implications on the detectability of fluids and on AVO signatures to which much attention should be given. Rock physics parameters are therefore site-specific and each area should be carefully studied in order to acquire sufficient knowledge of the given area before interpretations.

1. INTRODUCTION

1.1. Objective

This thesis is a presentation of a rock-physics study of a poorly consolidated sandstone reservoir of the North Sea. The main objective is to use appropriate rock physics theories and models to diagnose rock physics trends for a given area of study. We explain how these trends are altered by rock properties such as, cementation, mineralogy, porosity (and sorting), pressure, temperature, and fluid saturation. We also show how understanding the effects of these factors on fluid and lithology sensitivity, would help the seismic interpreter to avoid some of the pitfalls in conventional interpretation.

1.2. Motivation

Well log and seismic data interpretation are a fundamental part in reservoir characterization. Geologists are able to understand subsurface rock composition by detail analysis of core samples that are logged from within the earth. Detail knowledge of these subsurface rocks helps petroleum geoscientists who, in search of hydrocarbons, are able to improve their interpretation skills in quantifying and qualifying hydrocarbons. These interpretations have led to the many discoveries of hydrocarbon reservoirs around the world such as in the Gulf of Mexico and the North Sea, amongst several others. However, there is still a great need for new and more advanced technology as some of the methods already employed today, are not a hundred percent accurate. The introduction of rock physics and AVO analysis has helped to detect fluid and lithology at various depths and has become an integral part of hydrocarbon exploration. Several rock physics models have been developed to help in this search. Probabilistic though they may be, some of these theories have been proven very useful.

In this study, we employ the modified Hashmin-Shtrikman bounds using the Hertz-Mindlin theory. Also included are the contact cement theory, and the constant cement model. We try to use these models to link elastic and seismic properties with geologic properties and to estimate the extent to which these geologic trends may influence the lithology and fluid sensitivity of the seismic parameters. We have limited the use of the models to specific target zones within the area of study and have taken into consideration, the underlying principles and assumption(s) on which each of the models is based, in order to avoid misinterpretation during the data analysis. Focus has been on deriving models for clean sands, shaly sands, sandy shales, and shales as these are the lithologies encountered in the wells. We have used the following algorithm:

- Using an appropriate theory to define bounds, we model the given lithology under investigation by first defining end-members. The low-porosity end-member is at 0% porosity where we have the mineral point.

- We derive effective bulk and shear moduli models (and 'dry' velocities, where desired) under given pressure conditions for the given lithology and also add fractions of other possible mineralogical mixture found in the area of study.
- We perform fluid substitution by using Gassmann's relations (1951) to investigate the lithology and fluid sensitivity of elastic and seismic parameters under various conditions such as pressure, temperature, mixed saturations, gas-oil-ratio (GOR), brine salinitiy, etc.
- We superimpose the rock physics models on in situ data from wells using cross-plots to estimate the moduli and velocities that would be needed to match the reservoir sandstone and cap-rock shale data.
- We attempt an estimate about the mineralogical composition of the sandstone and shales and also the possible geologic trends.

One important concept that has been used in the derivation of the rock physics models, is the concept of critical porosity. For most clastic rocks, a porosity separates their mechanical and acoustic behaviour into two domains (the red line in figure 1). This porosity has been referred to as critical porosity (ϕ_c) for instance, Nur et al. (1998). The critical porosity is a porosity of loose sand at which its volume in the shear zone does not change and should therefore be considered an important parameter of a loose sand state. For porosities that are less than ϕ_c, mineral grains are load bearing, while for porosities greater than ϕ_c, the fluid phase is assumed to support the load and the mineral grains in suspension (Nur, 1992). In this study, mention has been made of this concept and has been used for all the lithology type encountered in the region of interest.

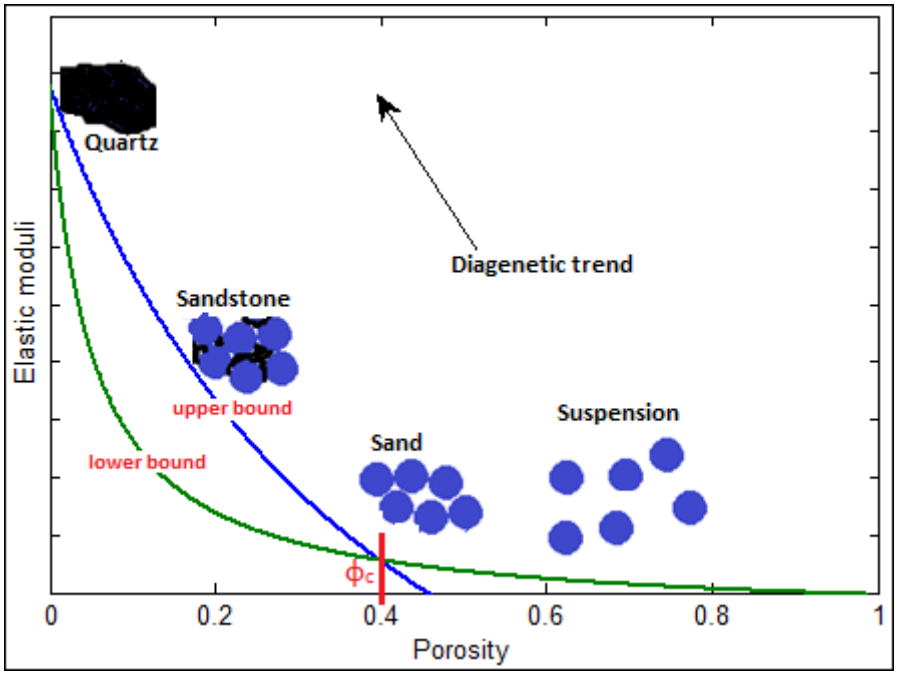

Figure 1: Concept of critical porosity illustrated using an upper and lower bound for sandstone. Notice that above the critical porosity ϕ_c which is the high-porosity end-member (40%), the sediments are in suspension. As we approach the low-porosity end-member (0%), we obtain the elastic moduli for quartz. The y-axis can also be labelled 'velocity'.

We see from figure 1 that at higher porosities, the sediments become more fluid supported (suspension) while at lower porosities, they become more grain supported. Eventually, at zero porosity we have the pure mineral. Studies have shown that above the critical porosity, sediments often exhibit some rigidity and therefore cannot be strictly treated as suspension (Raymer et al., 1980). From a geologic point of view, critical porosity describes the sediment when it is first deposited. This is related to grain sorting and angularity. Compaction and diagenesis later on, reduce the porosity and increase the elastic stiffness. Other factors that affect elastic properties are pressure, pore-fluid and lithology type.

Several wells were provided for this study but only three of them have been considered for this study due to the lack of complete well log data in the other wells. Two of the wells, the Kameleon well 24/6-2 (the main well) and the Kneler well 25/4-7 (a neighbouring well to well 24/6-2) are from the Alvheim field, North Sea while the third well (the Fram well 35/11-10), is from the Fram field, North Sea. In all these wells, both the Heimdal and Lista Formations were encountered, with the Alvheim wells containing oil and gas (with only oil in well 25/4-7) while the Fram well is brine saturated within the same Heimdal Formation, located in another area. We therefore have used the Fram well to compare the two Formations found at different depths and areas, to estimate any mineralogical differences or similarities. We also investigate the geologic trends within the Formations in the wells and finally, the results are also discussed in terms of expected seismic signatures.

Table 1: Various wells for this study and the intervals of investigation. Also included are the fluids within the intervals.

Well s	Field	Lista Formation (cap-rock shales) interval (m)	Heimdal Formation interval (m) (embodying reservoir fluids)	Fluids investigated
24/6-2	Alvheim	2054 – 2099	2099 – 2535	Gas/oil
25/4-7	Alvheim	2039 – 2085	2085 -	Oil
35/11-10	Fram	1578 – 1713	1713 – 1777	Brine

1.3. Field Location and Description

The Alvheim field is located on Production License 203 and extends into neighboring PL088 and PL036. The field is situated on the Norwegian Continental Shelf, west of Haugesund and close to the UK border in a water depth of 125 meters (410 feet). The field consists of three principal oil and gas discoveries named Kneler, Kameleon and Boa, each of which contains hydrocarbons in the Paleocene sandstones. Our focus in this study is on the Kameleon well 24/6-2.

Based on information published by the Norwegian Petroleum Directorate, the hydrocarbons in well 24/6-2 were found within the Heimdal T60 sand. In the gas zone; which is the upper part of the reservoir, we have massive channel sands. From 2010m (lower part of the Balder Formation Tuff Member) through the Sele Formation and Upper Lista Formation shale, right down to 2192m in the Heimdal formation, twelve cores were previously cut from the well for analyses. It was found, especially in the lower cores, that the sands are generally unconsolidated and friable. We have however realised in the course of this study these sands may also be described as poorly cemented due to the small amount (which would have a significant effect on velocities) of cement present. The quality of the reservoir is generally excellent but the small amount in the sands would reduce this quality.

The Kneler well 25/4-7 is a neighbouring well to well 24/6-2 and was designed as an exploratory test of an irregular 4-way closure midway between the Kameleon structure that was discovered by well 24/6-2 in 1998, and the Gekko structure (discovered by well 25/4-3 in 1974). The primary reservoir target was the Paleocene Heimdal formation. It was designed to provide local structural control to reduce uncertainty in field size and also provide stratigraphic control, particularly the position and character of a shale horizon at the base of the Upper Heimdal reservoir.

Well 35/11-10 is located on the western edge of the Uer Terrace, about 9 km north of the Troll Field. It was drilled to appraise the oil and gas discovery made in the exploration well 35/11-4, which encountered hydrocarbons in the Upper Sognefjord Formation separated from an oil column in the Lower Sognefjord Formation, in the Fensfjord Formation, and in the Brent Group. A gas oil contact was identified at 1987 m and an oil water contact at 2011 m. (Archives: The Norwegian Petroleum Directorate).

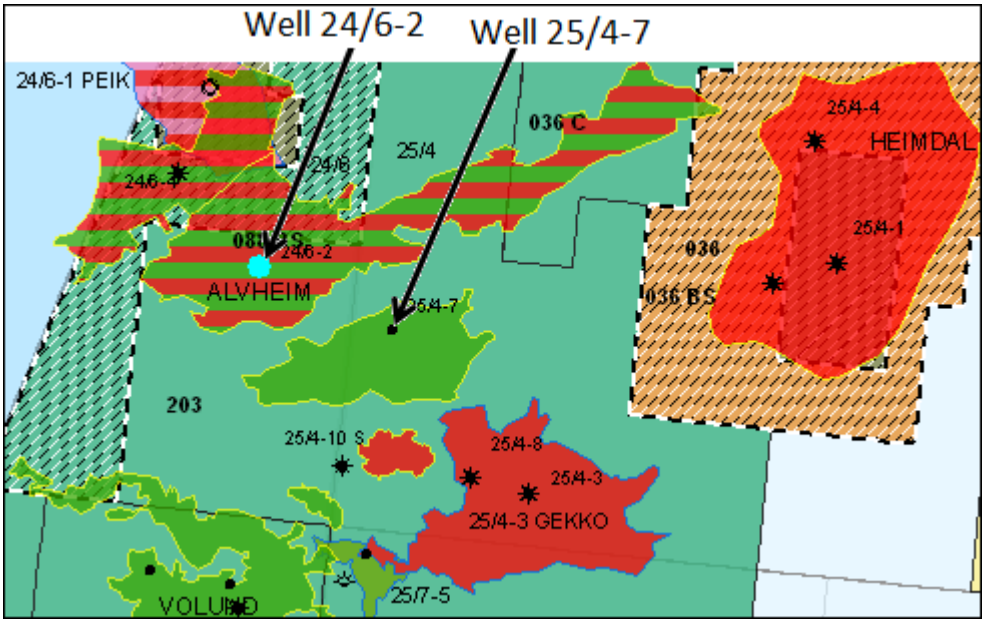

Figure 2: Location map of the Alvheim field, North Sea, showing well 24/6-2 and well 25/4-7.

2. BACKGROUND THEORY

2.1. Geophysical Well Log Analysis

Geoscientists use several types of logging such as cutting-logging, core-logging, petrophysical logging and geophysical logging etc. It is a key technology in the petroleum industry and widely used for exploration activities. Well logs need to be carefully conditioned or pre-processed prior to their use in a modelling workflow. This step is termed Geophysical Well Log Analysis (GWLA). Such analyses give us information of the sub-surface such as composition, physical properties around the borehole and how physical parameters vary.

The basic GWLA consists of:

- Collect and organize input data
- Perform geophysical log interpretation for volume minerals, porosity, and fluids
- Edit logs and perform mud filtrate invasion correction (as required)
- Generate missing curves
- Determine fluid properties (oil API, brine salinity, etc.) and reservoir pressure-temperature
- Perturb reservoir properties using rock physics effective medium models (pseudo-well modelling)
- Compute synthetic seismic traces
- Generate trend curves and cross-plots
- Create graphics and digital output files

The specifics of each project or job can be varied to suit the needs of the client and the characteristics of the data available.

2.2. Rock Physics Diagnostics

To infer porosity from seismic data, we need to understand the relations between the elastic rock properties and porosity and how varying elasticity influences the seismic properties. By elastic properties, we mean the bulk modulus (K), the normal shear constant (G), and the Poisson's ratio, (ν). We try to get the most information we can from these relations to ensure better interpretation of our data. During this research, we will apply rock physics theories to the results obtained from the available data. These theories include empirical or heuristic models. It is worth noting that the interpretations made by applying these models are not the best because the models themselves may originally be based on some assumptions and so, leading to some degree of uncertainty. They however, give us useful insight for further analysis.

Porosity modelling may not accurately describe the underlying velocity-porosity systematics for many reservoirs, especially over large ranges in porosity. This is because there is often no unique relationship between porosity and velocity in sedimentary rocks, due in large part

to variable pore geometries as well as the presence of highly variable concentrations of micro-cracks in the rock matrix (Smith et al., 2010). The presence of clay and its contribution to the total porosity of the rocks is considered. The porosity contributed by clay is not interconnected and therefore does not lead to permeability. If this is not carefully assessed and utilized in the development of the porosity model(s), such empirical or heuristic models may impose an unrealistic or non-existing velocity-porosity relationship on the reservoir. The amount and types of diagenetic cements and alteration is as well important. It would require that the geophysicist acquire sufficient knowledge of geology of the subsurface involved. We would make better interpreters if this is fulfilled because this may serve as a gateway to understanding some irregular trends during analysis.

Figure 3 illustrates the influence of microstructure on porosity where the P-wave velocity is plotted versus porosity for a shaly-sand system.

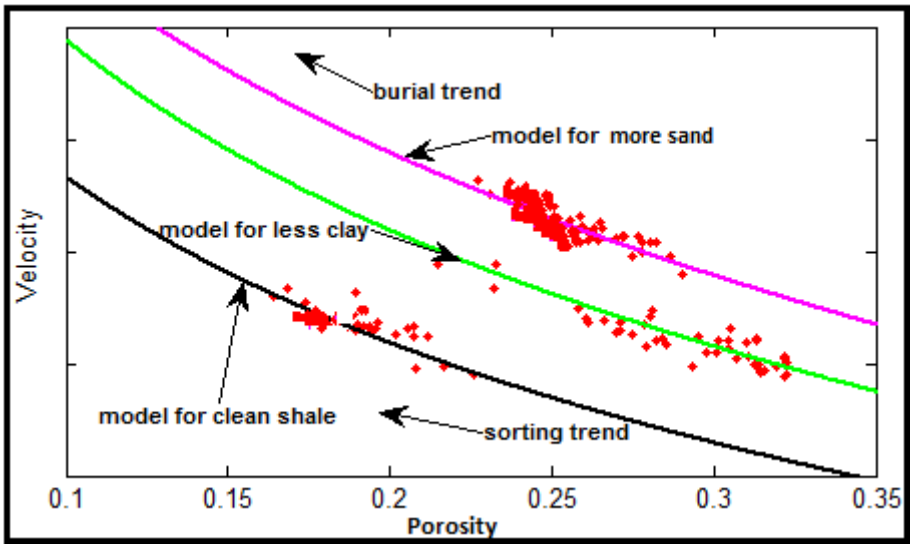

Figure 3: A depiction of elastic-wave velocity versus porosity for a shaly sand system showing the use of models in this rock physics studies. The data points on the black line would be shales while those on the green and magenta lines would be shaly and sands respectively.

From figure 3 we can see that rock physics models can help us understand some trends that from our data. Burial trend would correlate with cementation and compaction trends. Sorting trend would correlate with clay content within sandstones with a relatively small change in velocity. By superimposing theoretical model curves on figures in this study, we have diagnosed the data into the following:

- Sands with small amounts of cement.
- Sands from the same formation in different wells showing both similarities and differences in clay content – shaly sands.
- Friable sands and friable shales (estimated).
- Sandy shales.

The texture of these mixtures could be such that clay minerals, for instance, kaolinite, may fill up available pore spaces between quartz grains without affecting velocity, resulting to sorting (Avseth et al., 1999). Dvorkin and Brevik (1999) used this method to assess rock strength and permeability in a North Sea well.

From the works of Avseth et al., 1999, we read how rock physics diagnostic has been applied to well log data from two wells drilled through the sands of the Heimdal formation in the North Sea. As we go through this study, we also make comparison with such previous works that have earlier been carried out within the same area of study.

2.3. Rock Physics Models

This section presents some rock physics models that are mostly applied today in rock physics studies for fluid and lithology investigation. Due to the numerous models that exist for this purpose, we have limited our choice to the models that are relevant for this study. They are;

1. The friable sand model
2. The contact cement theory
3. The constant cement theory

2.3.1. Friable sand model

This theoretical model was introduced by Dvorkin and Nur (1996). It describes changes in the velocity – porosity relation with deteriorating sorting. Furthermore, it assumes that the porosity decreases from the initial porosity (critical porosity) due to the deposition of solid matter away from the grain contacts. Such a reduction may correspond to deteriorating grain sorting. This non-contact additional solid matter, weakly affects the stiffness of the rock (Dvorkin and Nur, 2000).

The theoretical effective-medium model connects two end-points in the elastic modulus-porosity plane. One end point is at critical porosity. The elastic moduli of the dry rock at that point are assumed to be the same as of an elastic sphere pack subject to confining pressure. These moduli are given by the Hertz-Mindlin theory (Mindlin, 1949):

$$K_{HM} = \left[\frac{n^2 \left(1-\phi_c\right)^2 {G_{MIN}}^2}{18\pi^2 \left(1-v\right)^2} P \right]^{\frac{1}{3}} \qquad (2.1)$$

$$G_{HM} = \frac{5-4v}{5\left(2-v\right)} \left[\frac{3n^2 \left(1-\phi_c\right)^2 {G_{MIN}}^2}{2\pi^2 \left(1-v\right)^2} P \right]^{\frac{1}{3}} \qquad (2.2)$$

$$n = 20 - 34*\phi + 14*\phi^2$$

where K_{HM} and G_{HM} are the 'dry' rock bulk and shear moduli respectively at critical porosity, ϕ_c. P is the effective pressure (i.e., the difference between the overburden

pressure and the pore pressure). G_{MIN} and v are the shear modulus and Poisson's ratio of the solid phase respectively, and n is the coordination number (the average number of contacts per grain) and can be determined at any given porosity, ϕ . From this we see that at the critical porosity, $\phi = \phi_c$. .

At the poor sorted end (zero porosity), the moduli represent the mineral point. Values between the poorly-sorted and the well-sorted end members are computed using the Hertz-Mindlin theory plus the modified Hashmin-Shtrikman lower bound. We use the equations:

$$K_{dry} = \left(\frac{\phi / \phi_c}{K_{HM} + 4G_{HM}/3} + \frac{1 - \phi / \phi_c}{K_{MIN} + 4G_{HM}/3} \right)^{-1} - 4G_{HM}/3 \qquad (2.3)$$

$$G_{dry} = \left(\frac{\phi / \phi_c}{G_{HM} + z} + \frac{1 - \phi / \phi_c}{G_{MIN} + z} \right)^{-1} - z \qquad (2.4)$$

where $z = \left(\frac{G_{HM}}{6} \right) \left(\frac{9K_{HM} + 8G_{HM}}{K_{HM} + 2G_{HM}} \right)$

K_{MIN} = bulk modulus of the mineral.

The upper bound can be computed by replacing G_{HM} with G_{MIN} in equation 2.3, and z with Z_{MIN} in equation 2.4 where,

$Z_{MIN} = (G_{MIN}/6) \left(\frac{9K_{MIN} + 8G_{MIN}}{K_{MIN} + 2G_{MIN}} \right)$. This gives us:

$$K_{dry} = \left(\frac{\phi / \phi_c}{K_{HM} + 4G_{MIN}/3} + \frac{1 - \phi / \phi_c}{K_{MIN} + 4G_{MIN}/3} \right)^{-1} - 4G_{MIN}/3 \qquad (2.5)$$

$$G_{dry} = \left(\frac{\phi / \phi_c}{G_{HM} + Z_{MIN}} + \frac{1 - \phi / \phi_c}{G_{MIN} + Z_{MIN}} \right)^{-1} - Z_{MIN} \qquad (2.6)$$

However, using the Hertz – Mindlin theory over-predicts the shear modulus. We have applied a simple slip factor correction (based on personal communication with Avseth) by using $G_{HM}=0.5G_{HM}$.

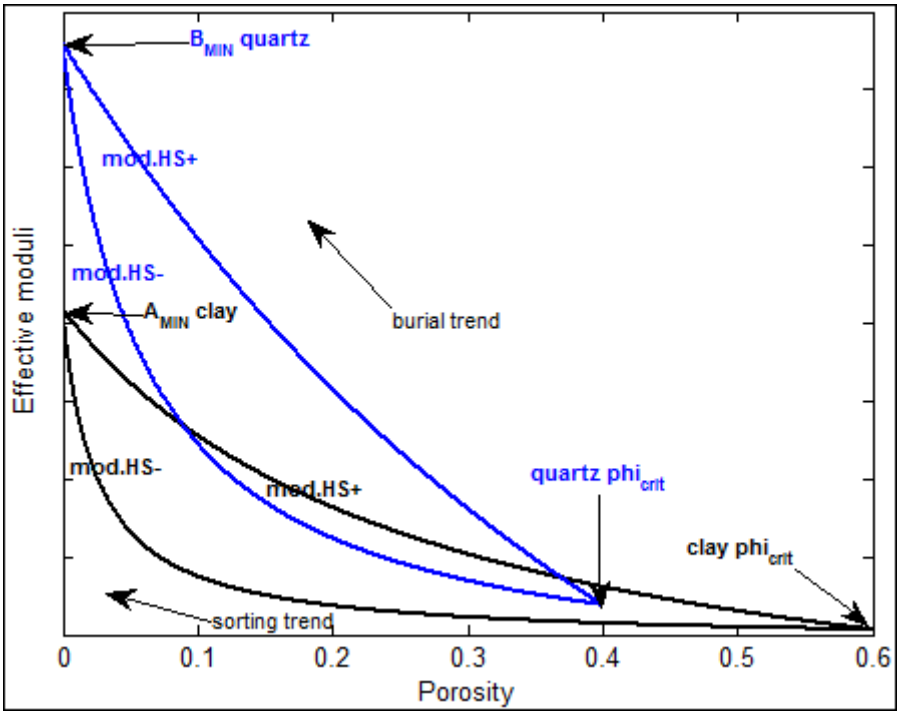

Figure 4: Modified Hashmin-Shtrikman upper (HS+) and lower (HS-) bounds plus Hertz – Mindlin (HM) theory for sandstone (blue lines and labels) and shales (black lines and labels). If we assume 100% clay in the shales, then ***A_{MIN}*** *represents clay mineral moduli while assuming 100% quartz in the sandstone means* ***B_{MIN}*** *represents quartz mineral moduli. We see a lower critical porosity for quartz (40%) than clay (60%) due to inherent porosity of clay minerals. For the same reason, we may never have critical porosity of zero for clay. We interpret data very close to their respective upper bounds as compacted and/or cemented (for quartz) and compacted (for shale). This is because clay is seldom associated to cementation. While data that plot close to their respective lower bounds would be interpreted as friable.*

Constant clay lines for shaly sands can also be modelled using the principles of the friable sand model. The Dvorkin-Gutierrez silty shale model can be used to model sandy shale lines where we replace ϕ_c with ϕ_{sh} i.e., porosity of a clean shale and the fraction of clay in the rock (C) is given by $C = \phi / \phi_{sh}$. Here we assume that the silt (quartz) grains are dispersed in the clay matrix. This gives the equation;

$$K_{sat} = \left(\frac{C}{K_{sh} + 4G_{sh}/3} + \frac{1-C}{K_{qtz} + 4G_{sh}/3} \right)^{-1} - 4G_{sh}/3 \qquad (2.7)$$

$$G_{sat} = \left(\frac{C}{G_{sh} + z_{sh}} + \frac{1-C}{G_{qtz} + z_{sh}} \right)^{-1} - z_{sh} \qquad (2.8)$$

$z_{sh} = (G_{sh}/6)\left(\frac{9K_{sh} + 8G_{sh}}{K_{sh} + 2G_{sh}} \right)$, where K_{sat} and G_{sat} are the bulk and shear moduli of saturated silty shale respectively, K_{sh} is the saturated bulk modulus of pure shale, while G_{sh} is the saturated shear modulus of pure shale. K_{qtz} and G_{qtz} are the mineral bulk and shear moduli

of silt grains (we assumed 100% quartz). The bulk density of the shales with dispersed quartz is:

$$\rho_b = \rho_{qtz}(1-C) + C(1-\phi_{sh})\rho_{clay} + C*\phi_{sh}*\rho_{fl} \quad (2.9)$$

where ρ_{qtz} is the density of quartz mineral and ρ_{clay} is the density of solid clay.

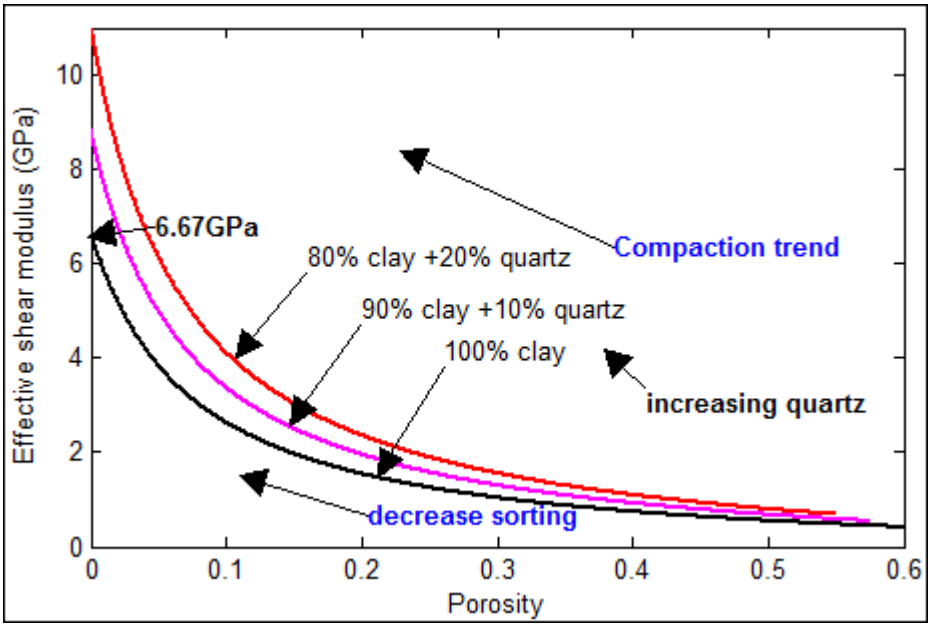

Figure 5: Shear modulus versus porosity for shales with increasing quart content trends using model lines for friable silty shale. We assumed 60% critical porosity for pure shale, 57.5% for an addition of 10% quartz and 55% for an addition of 20% quartz. Models are derived at 18MPa effective pressure.

2.3.2. Contact-cement model

The contact-cement model describes the velocity-porosity behaviour versus cement volume at high porosities. When the contact cement fills the crack-like spaces near the grain contacts, the effect created is the rapid stiffening of the rock with very little change in porosity and thus would tend to eliminate further sensitivity to effective pressure in the model. The high-porosity member is the critical porosity which can vary as a function of sorting. For practical purposes, we assume this porosity to be equal or close to the well-sorted end member of the friable-sand model. More poorly sorted cemented sandstones are then modelled using the constant-cement model. (Avseth et al., 2005).

From our knowledge of geology, we know that effective pressure increases with depth due to the increase in overburden material and reduction in porosity. During this, smaller grains may fill in the pore spaces of the original sediments. In shales, there would be a loss of bound water from the clay as compaction and diagenesis take place. It would therefore be logical to think that, following this trend of increase in pressure with depth in the subsurface, sands are likely to become cemented sandstones as cement 'glues' the grain contacts (Avseth et al., 2005).

The contact-cement model (Dvorkin and Nur, 1996) assumes that porosity decreases from the initial critical porosity value due to the uniform deposition of cement layers on the surface of the grains. This cement may be diagenetic quartz, calcite, or reactive clay (such as illite). The diagenetic cement dramatically increases the stiffness of the sand by reinforcing the grain contacts. The mathematical model is based on a rigorous contact-problem solution by Dvorkin et al., (1994).

$$K_{dry} = \frac{1}{6} n(1-\phi_c) M_c \hat{S}_n, \tag{2. 10}$$

$$G_{dry} = \frac{3}{5} K_{eff} + \frac{3}{20} n(1-\phi_c) G_c \hat{S}_\tau, \tag{2. 11}$$

where

$M_c = \rho_c V_{Pc}^2$, and $G_c = \rho_c V_{Sc}^2$,

ρ_c is the cement's density; V_{Pc} and V_{Sc} and are its P- and S-wave velocities respectively of the cement. K_{dry} and G_{dry} are the effective bulk and shear moduli respectively. Parameters $\hat{S}_n$ and $\hat{S}_\tau$ are proportional to the normal and shear stiffness, respectively, of a cemented two-grain combination. They depend on the amount of the contact cement and on the properties of the cement and the grains. They are computed using the following equations;

$\hat{S}_n = A_n(\Lambda_n)\alpha \wedge 2 + B_n(\Lambda_n)\alpha + C_n(\Lambda_n), A_n(\Lambda_n) = -0.024153\Lambda_n \wedge -1.3646$
$B_n(\Lambda_n) = 0.20405\Lambda_n \wedge -0.89008, C_n(\Lambda_n) = 0.00024649\Lambda_n \wedge -1.9864$
$\hat{S}_\tau = A_\tau(\Lambda_\tau, vs)\alpha \wedge 2 + B_\tau(\Lambda_\tau, vs)\alpha + C_\tau(\Lambda_\tau, vs)$
$A_\tau(\Lambda_\tau, vs) = -10 \wedge -2 * (2.26vs \wedge 2 + 2.07vs + 2.3)\Lambda_\tau \wedge (0.079vs \wedge 2 + 0.1754vs - 1.342)$
$B_\tau(\Lambda_\tau, vs) = (0.0573vs \wedge 2 + 0.0937vs + 0.202)\Lambda_\tau \wedge (0.0274vs \wedge 2 + 0.0529vs - 0.8765)$
$C_\tau(\Lambda_\tau, vs) = 10 \wedge -4 * (9.654vs \wedge 2 + 4.945vs + 3.1)\Lambda_\tau \wedge (0.01867vs \wedge 2 + 0.4011vs - 1.8186)$
$\Lambda_n = 2G_c(1-vs)(1-vc)/[\pi G_s(1-2vc)], \Lambda_\tau = G_c/(\pi G_s)$
$\alpha = [(2/3)(\phi_c - \phi)/(1-\phi_c)] \wedge 0.5$
$vc = 0.5(K_c/G_c - 2/3)/(K_c/G_c + 1/3)$
$vs = 0.5(K_s/G_s - 2/3)/(K_s/G_s + 1/3)$

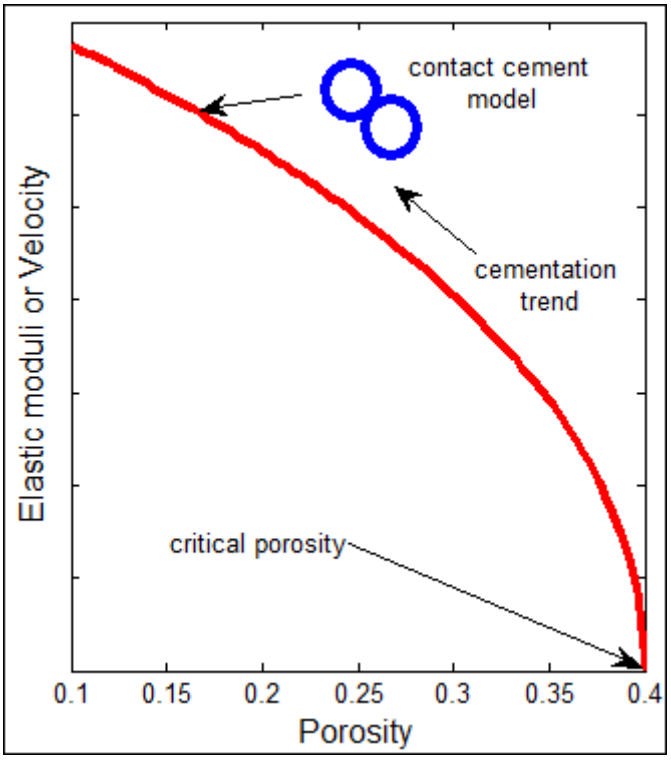

Figure 6: Dvorkin's cement model for consolidated sandstone. We have assumed the well-sorted end (initial sand pack) to have a porosity of 40%. Notice that with initial cement deposition at the grain surface, the curve is relatively steeper than the upper part of the curve as we approach the low-porosity end-member.

The "well-sorted" end member is a well-sorted packing of similar grains whose elastic properties are determined by the elasticity at the grain contacts. It typically has a critical porosity ϕ_C around 40% for sandstone.

2.3.3. Constant-cement model

This was introduced by Avseth et al., (2000), and assumes that sands of varying sorting (and therefore varying porosity) all have the same amount of contact cement. Porosity reduction is solely due to non-contact pore-filling material (e.g., deteriorating sorting). Mathematically, this model is a combination of the contact-cement model, where porosity reduces from the initial sand-pack porosity to porosity Φ_b because of contact-cement deposition, and the friable-sand model where porosity reduces from Φ_b because of the deposition of the solid phase away from the grain contacts.

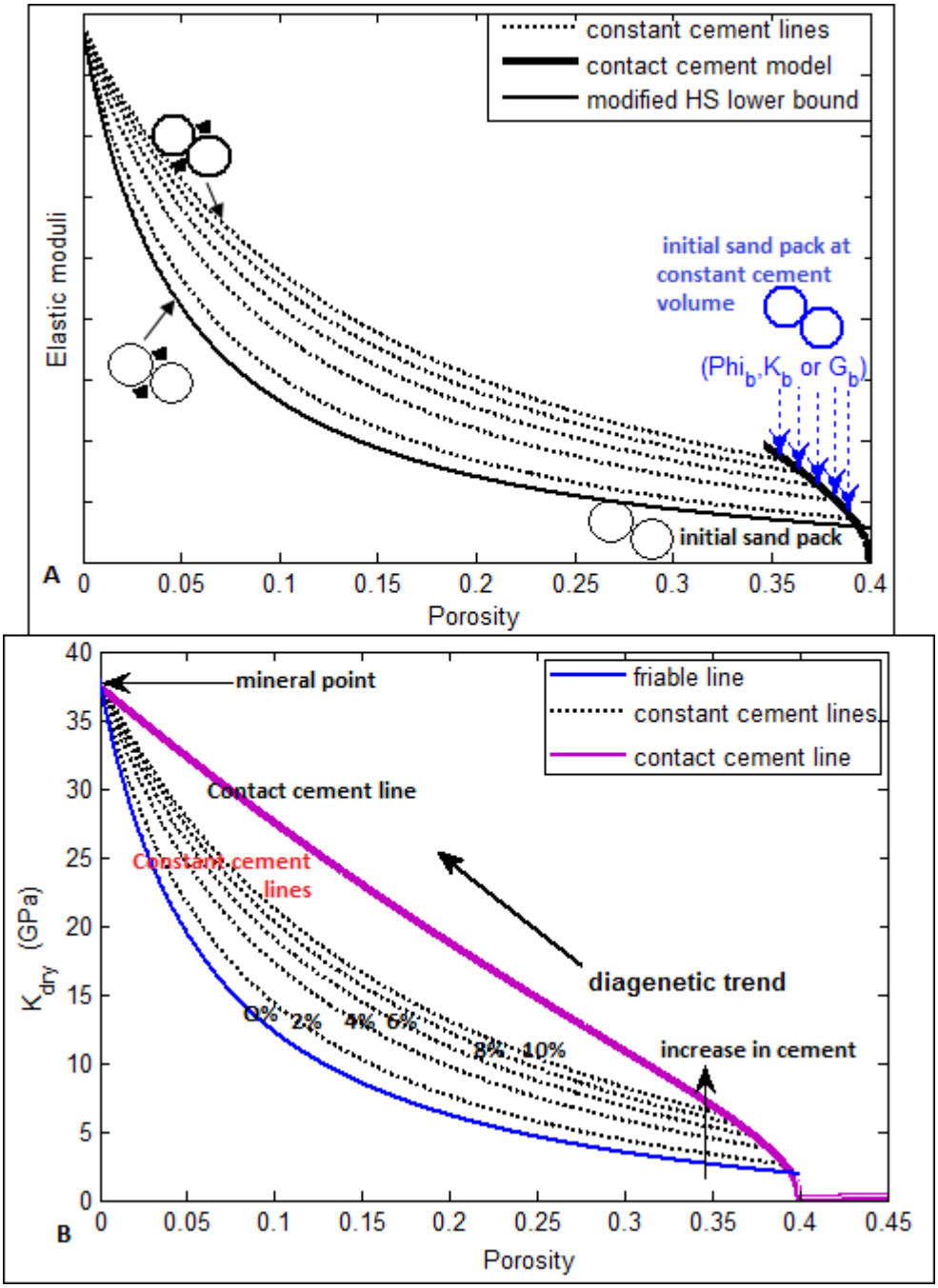

Figure 7: Schematic depiction of constant cement lines for high- and low-porosity end-members for sandstone in the elastic modulus-porosity plane. From the critical porosity (40%), lower porosity members were interpolated using the friable sand model. Notice that the higher end-members vary as cement increases. These are estimated using the contact cement theory. The 0% line is the friable sand line and was modelled at 70^{0}C and 20MPa effective pressure using the Hertz – Mindlin theory plus modified Hashmin – Shtrikman lower bound.

Figure 7 shows a model for the friable sand, contact cement, and constant cement lines for clean sands on effective bulk modulus-porosity cross-plot. The points at the well-sorted end where the constant cement lines intersect the contact cement line were computed using the contact cement model. The contact cement model shows that initial cementation increases modulus relatively steeply from the high porosity end (40%) up to about these

intersection points and then. We also see that at zero porosity all the lines plot at the mineral point of 38GPa. Notice that the presence of very little cement, for instance, 2%, results in an increase of the bulk modulus and this would cause a significant increase in velocities. From bottom to top, the constant cement lines are: 0% (friable line), 2%, 4%, 6%, 8%, and 10%.

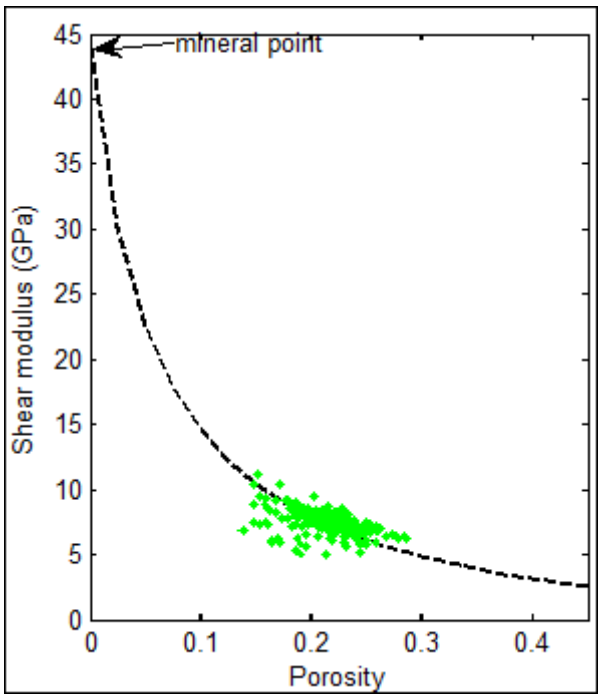

Figure 8: Shear modulus versus porosity to illustrate how well log data could be diagnosed using a constant cement line. Data is in situ from a gas zone of a poorly cemented sandstone reservoir of the North Sea. The curve is a constant cement line with 2% cement.

Figure 8 shows how the constant cement model can be used to diagnose the cement percentage within a given reservoir. Several lines of constant cement can be modelled to find the best fit for a given data. Since we relate amount of cement to burial depth, the constant cement model may be most suitable for providing an insight to infer cement content for a given reservoir. This model has been referred to as a *constant-depth* model for clean sands (Avseth et al., 2005). However, it is possible that cement can have a local source and therefore cause a considerable lateral variation in velocity.

We need to first adjust the well-sorted end-member porosity, $\emptyset_b$. Then we compute the dry-rock bulk (K_b) and shear moduli (G_b) at this porosity from the contact-cement model. Equations for the dry-rock bulk (K_{dry}) and shear (G_{dry}) moduli at a smaller porosity $\emptyset$ are then interpolated with a lower bound:

$$K_{dry} = \left[\frac{\emptyset / \emptyset_b}{K_b + (4/3)G_b} + \frac{1 - \emptyset / \emptyset_b}{K_{MIN} + (4/3)G_b} \right]^{-1} - \frac{4}{3} G_b \qquad (2.12)$$

and

$$G_{dry} = \left[\frac{\emptyset / \emptyset_b}{G_b + z} + \frac{1 - \emptyset / \emptyset_b}{G_{MIN} + z} \right]^{-1} - z \qquad (2.13)$$

where

$$z = \frac{G_b}{6} \left(\frac{9K_b + 8G_b}{K_b + 2G_b} \right)$$

K_{MIN} = bulk modulus of the mineral grain,

G_{MIN} = shear modulus of the mineral grain.

Avseth et al. (2005), also state that if more poorly sorted sands means increased grain contacts, the amount of contact cement will be somewhat correlated with degree of sorting. In this work, the constant cement model has been the most used model in several of the cross-plots as the main well was found to be poorly cemented. We model several lines containing different amount of cement and try to logically interpret our data taking into consideration the effects of rock properties such as, sorting, clay content, burial depth, pressure, temperature, and mineralogical alterations.

3. METHOLOGY

In this section, we present the various steps and methods we have employed for this study. This algorithm can be used for any depth interval within the area of study as follows:

- Estimate the mineral moduli of the sands and shales.
- Estimate the high-porosity end-member. The low-porosity end-member is zero. Using the modified Hashmin-Shtrikman lower bound, model the reservoir sandstones for clean sands and shaly sands. Also model the modified Hashmin – Shtrikman bound, contact cement model, and the constant cement lines from 0% to 10% (as may b e required)
- We derive effective bulk and shear moduli models (and velocity models) for shaly sands by adding fractions of clay to the sandstones. Assuming the clay particles fill up the pore spaces between the sand grains, for increasing fractions of clay, we reduce the critical porosity accordingly.
- We derive effective bulk and shear moduli models (and velocity models) for sandy shales by adding fractions of quartz to clay. For increasing quartz fraction we reduce the critical porosity by estimation depending on the given silt fraction.
- Apply Gassmann's substitution to estimate the bulk moduli with various fluid saturations. Also model velocities using the elastic moduli and estimated bulk densities. The shear property for every mixture of lithology remains constant.
- Superimpose the rock physics models on in situ data from wells using cross-plots to estimate the moduli and velocities that would be needed to match the reservoir sandstone data.
- Attempt an estimate about the mineralogical composition of the sandstone and also the possible geologic trends using a rock physics template of acoustic impedance versus Vp/Vs.
- Account for the effects of these geologic trends on AVO signatures.

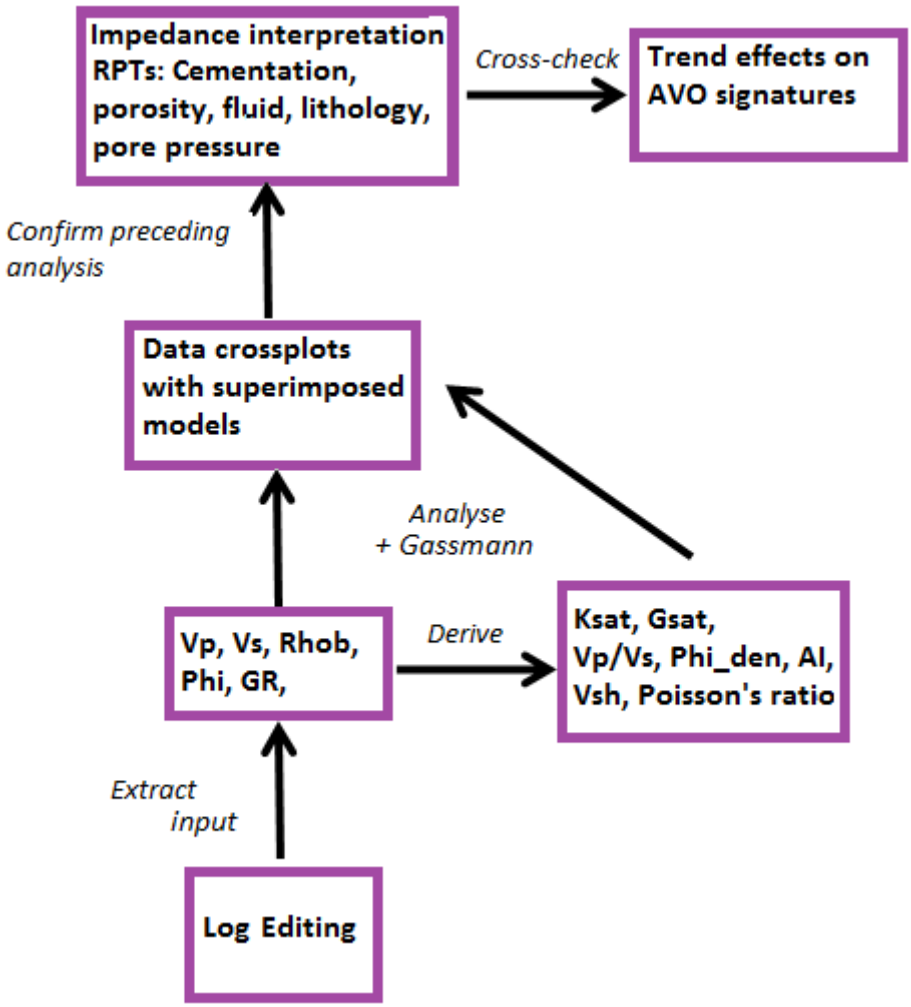

Figure 9: A simplified algorithm for achieving the objective of this rock physics study

3.1. Well Logs Edition and conditioning

This process is often overlooked or oversimplified prior to the application of a rock physics or geophysical model. Frequent editing of well log data would require depth shifting, estimation of pseudo-data to replace bad log data, and invasion corrections (if necessary). (Tad M. Smith, 2011). Although geophysicists often oversimplify the editing process because these edits are below seismic resolution, and are therefore unimportant, it is the opinion of the above author that these edits should be performed with care anytime we are generating log-based seismic models or using log data to interpret seismic responses. Failure to this effect could lead to erroneous assumptions and expectations from seismic amplitudes.

In this thesis, most of the well logs provided are of good quality. We estimate the porosity from the density porosity and the shale volume from the gamma ray log with assumption that gamma ray is a proxyl for the volume of clay. We use Greenberg – Castagna empirical formula for shear prediction for one of the wells due to an observed slight mismatch with the measured P-velocity. The main well and its neighbouring well seemed to have good shear velocities. Other logs that have been generated include, volume of shale and sorting logs (using ratio of logged porosity/critical porosity for sorting).

3.2. Fluid Substitution

Fluid substitution provides the interpreter with a reliable tool for modelling and quantifying the various fluid scenarios which might give rise to an observed AVO or 4D response (Smith, 2011). Fluid substitution is a rock physics problem of understanding and predicting how seismic velocity and impedance depend on pore fluids (Avseth, 2010). It uses Gassmann's equation to calculate elastic properties at the desired saturation, from either the dry rock or a rock saturated with another fluid (Sheriff, 2006). It is remarkably accurate and robust (Mavko et al., 1998) for porosities greater than 10%.

To compare theoretically modelled results with in situ data, fluid substitution has been applied. The Gassmann equations have particularly been introduced for this purpose.

$$\frac{K_{sat}}{K_{\min} - K_{sat}} = \frac{K_{dry}}{K_{\min} - K_{dry}} + \frac{K_{fl}}{\phi(K_{\min} - K_{fl})} \tag{3. 1}$$

$$G_{sat} = G_{dry}, \tag{3. 2}$$

where,

K_{dry} = effective bulk modulus of rock;

K_{sat} = bulk modulus of the saturated rock with pore fluid;

$K_{\min}$ = bulk modulus of the mineral grain;

K_{fl} = bulk modulus of pore fluid;

G_{dry} = effective shear modulus of rock;

G_{sat} = shear modulus of rock with pore fluid;

ϕ = porosity

Using the theoretically derived 'dry' bulk modulus described in section 2.3, we are able to determine the bulk modulus for a given lithology that is saturated with a given fluid or fluid mixture. Since the dry bulk modulus of a given lithology would remain the same regardless of the type of fluid in the available pores, we can invert the Gassmann equation to compute the bulk modulus of the rock saturated with any other fluid (s) of known bulk modulus.

$$\frac{K_{sat.A}}{K_{\min} - K_{sat.A}} - \frac{K_{fl.A}}{\phi(K_{\min} - K_{fl.A})} = \frac{K_{sat.B}}{K_{\min} - K_{sat.B}} - \frac{K_{fl.B}}{\phi(K_{\min} - K_{fl.B})} \tag{3.3}$$

where subscript **A** and **B** represent the different fluids being substituted from one to the other i.e., $K_{fl.A}$ is the bulk modulus of A and $K_{fl.B}$ is the bulk modulus of B. $K_{sat.A}$ is the initial

rock bulk modulus saturated with fluid A and $K_{sat.B}$ is the rock bulk modulus saturated with substituted fluid B (to be determined).

We can find the bulk modulus of various fluids and minerals from the vast number of published literature. For a mixture of fluids, A and B, we assume a fine scale mixture and use the Wood's equation to compute the bulk modulus of the fluid mixture, $K_{fl.mix}$.

$$K_{fl.mix} = \left[\frac{S_A}{K_{fl.A}} + \frac{(1-S_A)}{K_{fl.B}} \right]^{-1}, \tag{3. 4}$$

where,

$K_{fl.mix}$=bulk modulus of fluid mixture.

$S_A =$ saturation of fluid A,

$1-S_A =$ saturation of fluid B.

In hydrocarbon exploration we assume that for a hydrocarbon reservoir, there exist some amount of irreducible water in the fluid mixture. If the hydrocarbon is oil, then we assume some amount of dissolved gas in addition to the water.

For computing the elastic moduli of mixed lithology, we have used Hill average (Mavko et al., 1998), given by:

$$K_{mix} = 0.5\left[\left(f_A * K_A + (1-f_A) * K_B \right) + \left(\frac{f_A}{K_A} + \frac{(1-f_A)}{K_B} \right)^{-1} \right] \tag{3.5}$$

Where

$K_{mix} =$ bulk modulus of the mixed lithology,

f_A =volume fraction of mineral A,

$1-f_A$ =volume fraction of mineral B

Next, we can compute the velocities of saturated rocks using the equations:

$$V_P = \sqrt{\frac{\left(K + \frac{4}{3}G \right)}{\rho_b}}; \tag{3.6}$$

$$V_S = \sqrt{\frac{G}{\rho_b}} \tag{3.7}$$

where K and G represent bulk and shear moduli of the saturated rock respectively. We also use the equation to derive the initial moduli from well logs by using the well log velocities and bulk density.

The bulk density is given by:

$$\rho_b = \rho_{ma}(1-\phi) + \phi\rho_{fl} \tag{3.8}$$

where,

ρ_{ma} = density of the matrix (mineral grains)

ϕ = porosity.

In this study we assume sand grain density = 2.65g/ccm

Although the proper choice of porosity for shaly sands in Gassmann substitution is not clear, in this study, we use total porosity for both clean sands and shaly sands and superimpose the Gassmann relations to apply using effective properties for shale formations.

The properties of hydrocarbons are more variable and depend strongly on temperature, pressure, and composition (Murphy, 1993). We computed the Fluid properties to reservoir conditions using the Crewes fluid properties calculator which employs the empirical relations described by Batzle and Wang (1992).

CREWES Fluid Properties Calculator

1) Enter temperature and pressure of the fluids, and indicate the units

Temperature 70 ◉ celsius ○ Kelvin ○ Fahrenheit

Pressure 20 ◉ MPa ○ bar ○ atm ○ psi ○ kbar

2) Complete calculations individually for each desired fluid (gas, oil and/or brine)

Gas Phase				**Oil Phase**			**Brine Phase**	
1. Enter composition:				1. Enter information:			1. Enter information:	
○ by mole fractions: (Solves Peng-Robinson equation of state)				STP density: 19 ◉ API ○ g/cm3			Salinity (NaCl): 090000 ◉ ppm ○ weight fraction	
CH4	1	CO2	0	Gas-Oil Ratio 100 ◉ L/L ○ % of max			2. Click here to calculate brine properties	
C2H6	0	H2S	0	G for saturating gas 0.6			3. Calculated brine properties	
C3H8	0	N2	0	2. Click here to calculate oil properties			**Density:**	1.049786 g/cm3
C4H10	0	O2	0	3. Calculated oil properties			1049.786 kg/m3	65.536 lb/ft3
◉ by density ratio: (B&W, 1992)		G	.6	**Density:**	0.81316525 g/cm3		**Acoustic speed:**	1664.9816 m/s
2. Click here to calculate gas properties				813.1652 kg/m3	50.764256 lb/ft3		1.6649816 km/s	5462.538 ft/s
3. Calculated gas properties				**Acoustic speed:**	1150.2212 m/s		**Bulk modulus:**	2910.1787 MPa
Density:	0.1354222 g/cm3			1.1502212 km/s	3773.6917 ft/s		29.101786 kbar	422085.9 psi
135.4222 kg/m3	8.454133 lb/ft3			**Bulk modulus:**	1075.8247 MPa		**Viscosity:**	0.57321954 cP
Acoustic speed:	548.5348 m/s			10.758247 kbar	156035.25 psi		0.0057321955 Poise	
0.54853475 km/s	1799.6548 ft/s			**Viscosity:**	3.7154078 cP			
Bulk modulus:	40.74724 MPa			0.03715408 Poise				
0.40747237 kbar	5909.8896 psi			**Maximum Gas-Oil Ratio: 63.30638 L/L**				
Viscosity:	0.021861594 cP							
2.1861595E-4 Poise								

Figure 10: The Crewes fluid properities calculator

The value for the fluid density, ρ_{fl}, takes into consideration the total amount of pore space filled with individual fluid types. This is defined by:

$$\rho_{fl} = S_w \rho_w + (1 - S_w)\rho_{hc} \quad (3.11)$$

where,

$S_w =$ water saturation,

$\rho_w =$ density of formation water,

$\rho_{hc} =$ density of hydrocarbon,

($1-S_w$)=hydrocarbon saturation.

By using the Gassmann's theory, we have included the following assumptions by Wang, 2001:

- The rock is macroscopically homogeneous and monomineralic.
- All the pores are communicating (pressure is able to equilibrate, which relates to zero frequency assumption).
- The pores are filled with frictionless fluid (the viscosity of the saturating fluid is zero).
- The rock-fluid system is closed (undrained).
- There is no interaction between solid and fluid (no hardening or softening the frame due to interactions with fluid).

Clay-rich sandstones actually violate the monomineralic assumption, so we end up 'superimposing' the Gassmann's relations to apply by adapting the porosity and/or the effective mineral properties (Avseth et al., 2005).

3.3. Rock Physics Templates (RPTs) Analysis

The *Rock Physics Templates* (RPTs) technology that was presented by Ødegaard and Avseth (2004) has become a tool for lithology and fluid prediction. The main goal of RPT analysis is to use rock physics models constrained by local geology to interpret and classify well-log and seismic data. Avseth et al., (2005), have described how a combination of depositional and diagenetic trend models with Gassmann fluid substitution can be used to make these templates of rock physics models for this purpose. This technology has been applied by petrophysicists (for formation evaluation), seismic interpreters (for analysis of inversion results), and rock physicists (for evaluation of seismic detectability from well logs).

In this work, we have applied this technology as a Vp/Vs ratio versus acoustic impedance discrimination of lithology and fluids and the effects of geologic trends on our reservoir sands. There exist a wide range of applications of RPT analysis as outlined below.

The wide range of applications of RPT analysis (Avseth et al., 2005)

- Interpretation of well-log data and assessing seismic detectability of observed facies and fluid variations.

- Petrophysical quality control of well-log data.
- "Quick and dirty" qualitative feasibility studies of various rock physics "What if" scenarios, both in terms of lithology and fluid substitutions.
- Calibration and validation of rock physics models to local conditions.
- Interpretation and classification of elastic inversion results.

The RPT plots are intuitive and link rock physics properties to geologic trends.

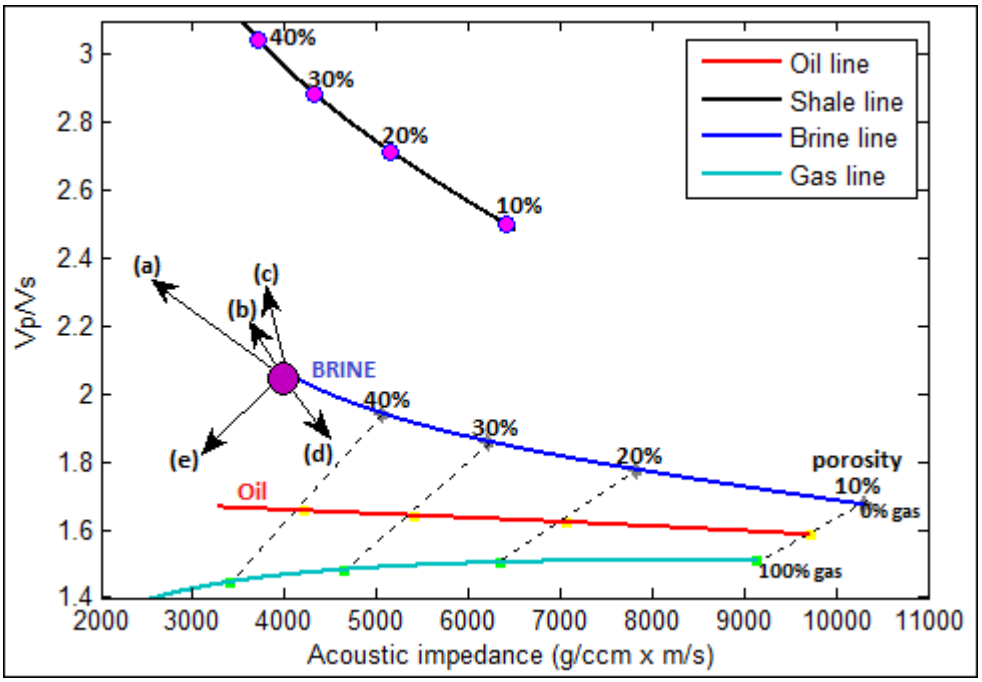

Figure 11: Illustration of a rock physics template of Vp/Vs versus acoustic impedance employed for the wells in this study from the Alvheim field, North Sea. The lines are constant cement lines of 2% saturated with different fluids: brine (blue), oil (red), and gas (cyan). The upper black line is the clay saturated constant clay line. Background trend is brine. The sand lines are computed at 70 degrees Celsius and 20MPa pressure while shale line is computed at 50 degrees Celsius, 18 MPa pressure.

Figure 11 shows a rock physics template of Vp/Vs versus acoustic impedance with brine as the background trend. The various trends shown represent the following geologic characteristics:

a. Increasing porosity
b. Decreasing effective pressure
c. Increasing cement volume
d. Increasing gas saturation
e. Increasing shaliness

3.4.AVO Attribute

The AVO technology had previously been considered as an unreliable tool after some unsuccessful applications. Today, it has been used in the petroleum industry to detect fluids

owing to the development of the technology. Before its application, we would need to find out if it is the appropriate tool to be used. It will work only if the rock physics and fluid characteristics of the target reservoir are expected to give a good AVO response (Avseth et al., 2005). Without having this done, AVO signatures may be misinterpreted when using real data.

We would investigate the effects of fluids, lithology and cementation in terms of changes in rock physics properties, on AVO signatures. To do this we would use the equations by Shuey (1985), for intercept, $R(0)$ and gradient, G :

$$R(0) = \frac{1}{2}\left(\frac{\Delta Vp}{Vp} + \frac{\Delta \rho}{\rho} \right) \tag{3.12}$$

$$G = \frac{1}{2}\frac{\Delta Vp}{Vp} - 2\frac{V_s^2}{V_p^2}\left(2\frac{V_s}{V_s} + \frac{\Delta \rho}{\rho} \right) \tag{3.13}$$

For two layers; layer 1 and layer 2, with velocities Vp1, Vs1 and Vp2, Vs2 respectively, and densities, $\rho 1, \rho 2$, respectively, then:

$\Delta V_p = V_{p2} - V_{p1}$ and $V_p = \left(V_{p2} + V_{p1}\right)/2$. Similarly,

$\Delta V_s = V_{s2} - V_{s1}$ and $V_s = \left(V_{s2} + V_{s1}\right)/2$

$\Delta \rho = \rho 2 - \rho 1$ and $\rho = \left(\rho 2 + \rho 1\right)/2$

With these formulae, hydrocarbons can be classified on the gradient – intercept plane.

The various classes shown on figure 12 are described in the table below:

Table 2: AVO classes, after Rutherford and Williams (1989), extended by Castagna and Smith (1994), and Ross and Kinman (1995). (Avseth et al., 2005).

Class	Relative impedance	Quadrant	R(0)	G	AVO product
I	High-impedance sand	4th	+	-	Negative
IIp	No or low contrast	4th	+	-	Negative
II		3rd	-	-	Positive
III	Low impedance	3rd		-	Positive
IV	Low impedance	2nd	-	+	negative

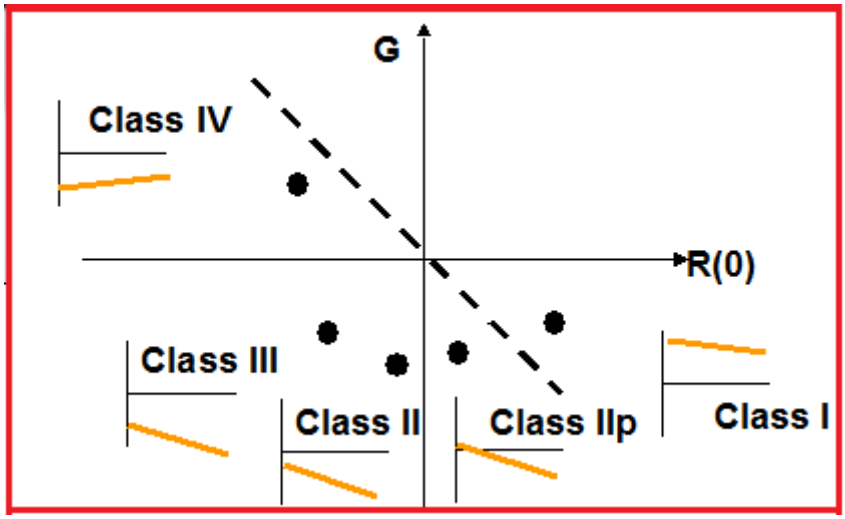

Figure 12: Illustration of the various classes of AVO signatures on an intercept – gradient plane. (Avseth, 2012, lecture notes, NTNU)

4. RESULTS AND DISCUSSION

This section presents the data analysis using the rock physics models superimposed on data plots. The results of the fluid substitutions that were carried out during this work have also been presented. The focus is on the target zone in selected wells, with emphasis on well-A. First, various rock physics models are presented and discussed. Next, the models are superimposed and compared with well log data for interpretation of different geologic trends. The results are also discussed in terms of expected seismic signatures in the area.

4.1. Theoretically Modelled results

In rock physics modelling need to define the end members between which other members are interpolated. The mineral point which is at zero porosity is the low porosity end member while the high porosity member would depend on the lithology being investigated. Due to the inherent porosity of clay minerals in shales, shales are usually deposited with a higher initial porosity (critical porosity) than sands. This critical porosity defines the high porosity end-member at a given pressure. We estimate the elastic stiffness at this porosity by using the contact theory or some other alternative theory such as the Hertz-Mindlin theory. In this study, we define the critical porosity of 40% for clean sandstones and 60% for clean shales.

Most sands rich in quartz have bulk modulus of the mineral matrix ranging from 35 – 40 GPa and shear modulus of the mineral matrix from 35 – 44 GPa (Smith, 2011). Two possible reasons for these variations are as follows:

a) Presence of minerals other than quartz in most sands.
b) The presence of cracks that leads to micro-structural defects in most framework grains, lowers the effective bulk and shear moduli of the mineral material.

In this work, we assume a solid bulk modulus and shear modulus of 38GPa and 44GPa respectively, for quartz and a solid bulk modulus and shear modulus of 20.9GPa and 6.67GPa respectively, for clay. Their mixed moduli are computed by the Hill average (equation 3.7).

The table below shows the elastic constants and other parameters used in this thesis work. However, where other values have been used other than the one in table 1 will be mentioned.

Table 3: Some parameter values for the lithology and fluids used in this study. The table does not include values for mixed lithology and fluids.

Parameter	Sand	Shale	Calcite cement	brine	Oil	Gas
Bulk modulus (GPa)	38	20.9	129,53	2.81		0.035
Shear modulus (GPa)	44	6.67	35	0	0	0
Density (g/ccm)	2.65	2.7	2.71	1.05	1.08	0.13
Critical porosity	0.4	0.6				
Coordination number (n)	8.6 at critical porosity	4.6 at critical porosity				
Salinity (ppm)				90000		

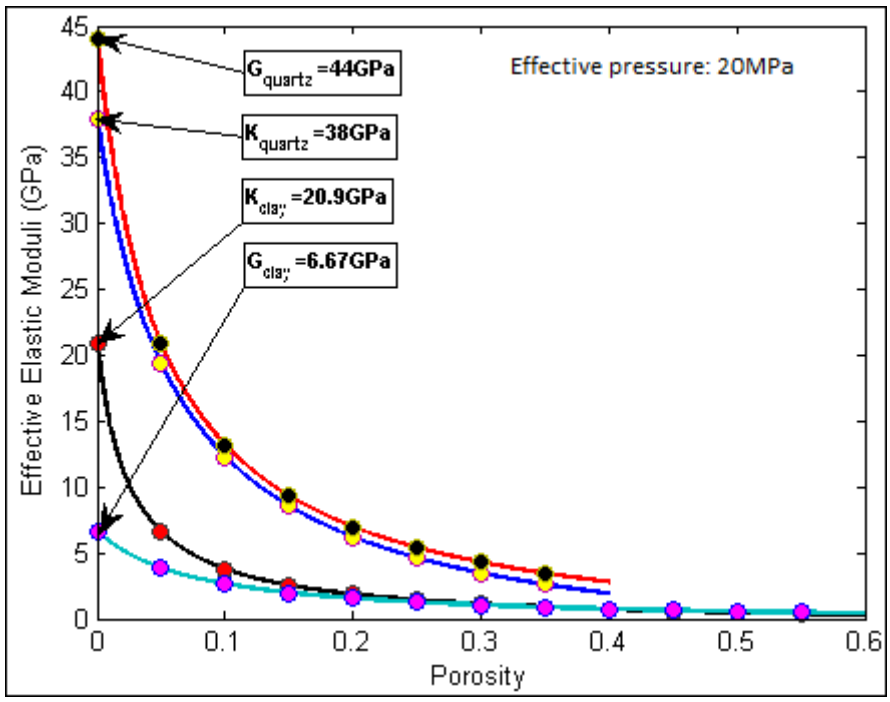

Figure 13: Theoretically predicted effective moduli vs. porosity for unconsolidated sandstones and shales at effective pressure 20MPa using the Hertz-Mindlin plus modified Hashmin-Shtrikman lower bounds. Critical porosities are 40% for sandstones and 60% for shale. The red and blue lines represent the effective shear and bulk moduli of sandstones (assuming 100% quartz) respectively while the cyan and black lines represent the effective shear and blulk moduli of shales respectively (assuming 100% clay).The bulk moduli (K_HM) and shear modului (G_HM) at the critical porosities are 1.908GPa and 2.789GPa respectively for sandstone and 0.452GPa 0.346GPa respectively for shale.

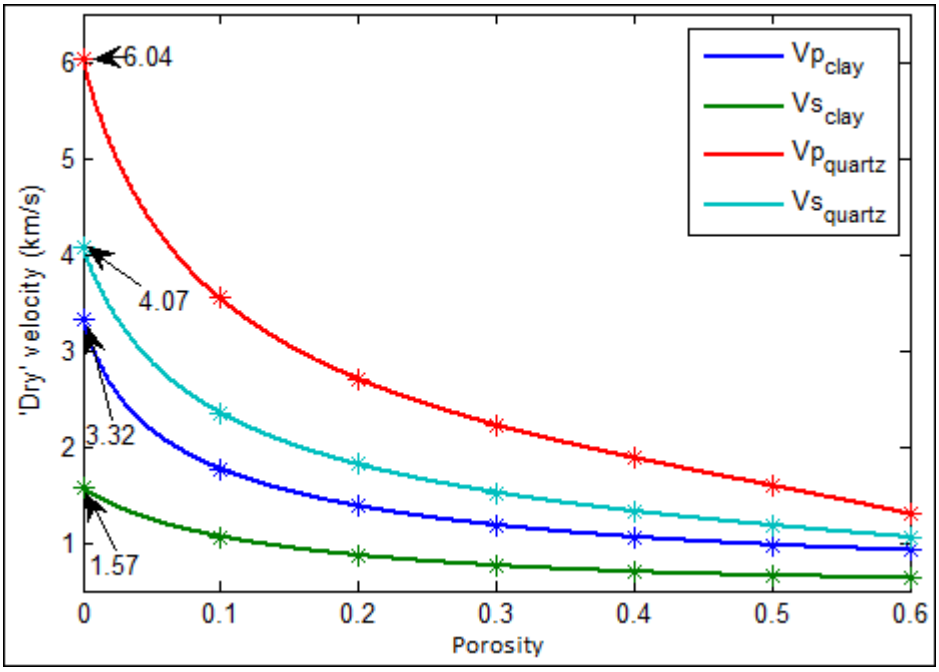

Figure 14: Effective velocity vs porosity as predicted theoretically for unconsolidated sandstones and shales at effective pressure 20MPa using the Hertz-Mindlin plus modified Hashmin-Shtrikman lower bounds. Critical porosities are 40% for sandstones and 60% for shale. The red and cyan lines represent the effective Vp and Vs of sandstones (assuming 100% quartz) respectively while the blue and green lines represent the effective Vp and Vs of shales respectively (assuming 100% clay).

We observe from figure 14 that the separation between the velocity lines is decreasing from the low-porosity end to the high porosity end.

4.2. Sensitivity Results

This section presents the results from fluid substitution by Gassmann's relations. We illustrate the sensitivity of moduli and velocities to fluids.

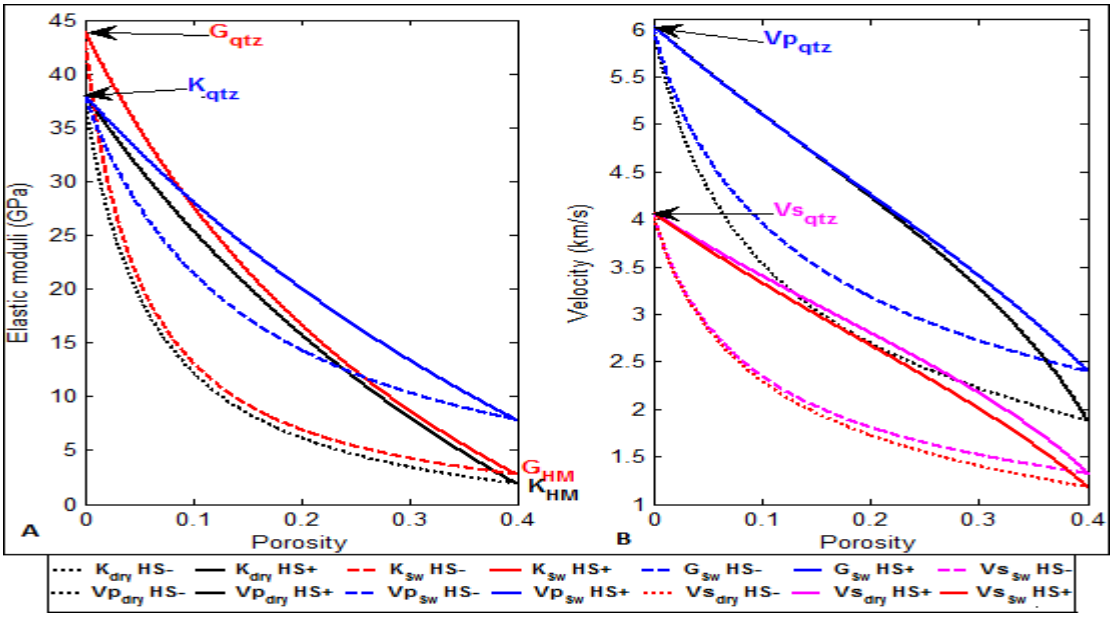

Figure 15: Theoretical illustration of how rock modulus (of sandstones assuming 100% quartz) and seismic velocities change as fluids fill up available pores in the rock using modified Hashmin – Shtrikman upper (HS+) and lower (HS-) bounds. The continuous lines represent the upper bounds while the broken and dotted lines represent the lower bounds. Effective pressure is 20MPa and 70^{0}C.

On plot figure 15 (**A**), blue lines represent brine-saturated bulk modulus (K_{sw}HS+ and K_{sw}HS-) while the corresponding 'dry' bulk modulus (K_{dry}HS+ and K_{dry}HS-) are represented by the black lines. The red lines represent the shear modulus (G_{sw}HS+ and G_{sw}HS-) where the 'dry' shear and saturated shear moduli are identical (assuming fluids have a zero shear modulus). On plot **B**, blue lines represent brine-saturated Vp (Vp_{sw}HS+ and Vp_{sw}HS-) while the corresponding 'dry' Vp (Vp_{dry} HS+ and Vp_{dry}HS-) are represented by the black lines. Red lines represent brine-saturated Vs (Vs_{sw}HS+ and Vs_{sw}HS-) while the corresponding 'dry' Vs (Vs_{dry}HS+ and Vs_{dry}HS-) are represented by the magenta lines. Notice the increase in bulk moduli from 'dry' to brine-saturation which has also resulted in an increase in Vp from 'dry' to brine-saturation as well. Contrarily, as we move from 'dry' rock to brine-saturated rock, Vs has decreased. This is due to the change in the bulk density from 'dry' (lower) to brine-saturated (higher) bulk density. However, the change in the shear velocities is very small compared to changes in Vp and bulk modulus. The elastic moduli (G_{HM} and K_{HM}) represent shear and bulk moduli respectively at the high-porosity end-member (40%) using the Hertz – Mindlin theory. For all saturation lines at the low-porosity end-member (0%), we obtain the mineral point assuming the rock is made up of 100% of the given mineral.

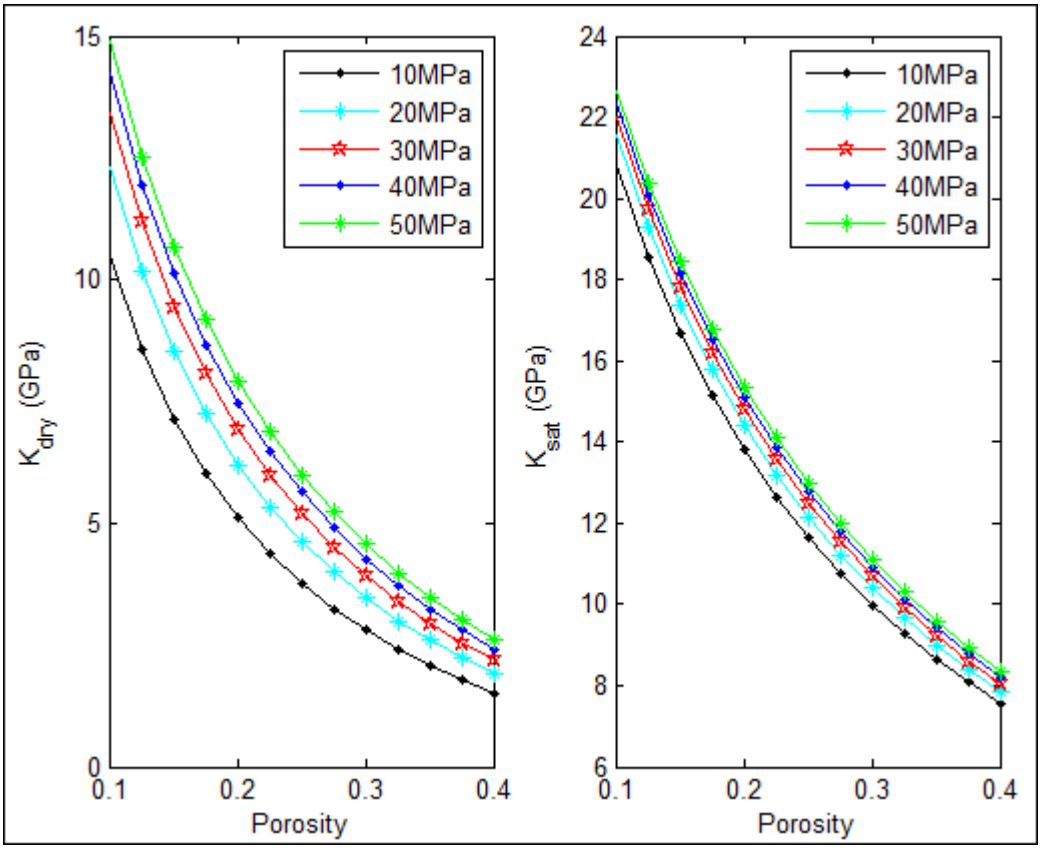

Figure 16: Theoretically derived effective modulus at various effective pressures using the Hert–Mindlin theory plus modified Hashmin – Shtrikman lower bounds for unconsolidated sandtone. Left: 'Dry' bulk modulus (K_{dry}) versus porosity. Right: Brine-saturated bulk modulus. Temperature (70 ^{0}C) and brine salinity (90000ppm) were kept constant. The pressures (MPa) are; 10 (black), 20 (cyan), 30 (red), 40 (blue), and 50 (green).

Figure 16 shows the effect of effective pressure on the rock bulk modulus for both 'dry' and saturated scenarios. Observe that both 'dry' and brine-saturated bulk modulus increase with increasing effective pressure. A possible reason for this is that as the effective pressure increases, the rock loses it porosity causing the sediments to become more compacted. With this increase in compaction (with depth), the rock frame increases (if cracks are present, the pressure may act normal to the cracks thereby, closing the crack pores). Notice that the sensitivity to fluids is decreasing with increased effective pressures.

Our conclusion from this was that for a given area of study, it is important to properly investigate the target depth to be able to estimate the effective pressures at this depth interval. Failure to accomplish this would be a pitfall during analysis as model responses would not be representative of the area of study.

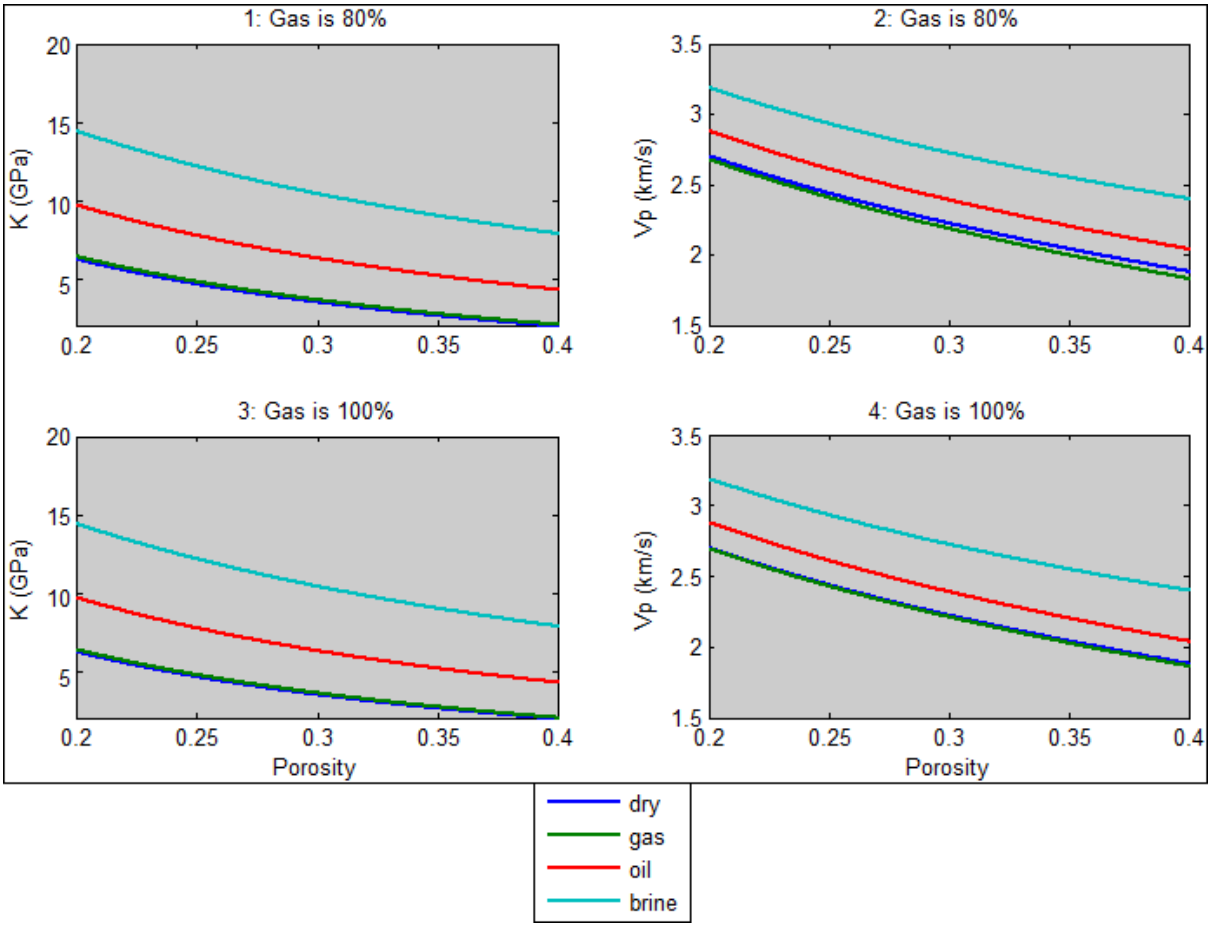

Figure 17: Comparison between varying gas-saturated models (green) for unconsolidated sandstones. The oil- (red) and brine- (cyan) saturated lines are constant at 100% saturatiom. We notice that at both gas saturations, (80% and 100%), the 'dry' (blue) and gas-saturated bulk moduli are almost inseparable. At 80% gas saturation (i.e., 5% oil and 15% brine), the separation between the 'dry' and gas-saturated P-wave velocities visibly increase at the well sorted end. At 100% gas saturation, the separation shown by the velocity is very poor. Effective pressure is 20MPa and temperature is 70^0C.

Figure 17 shows comparison between varying gas-saturated models (green) for unconsolidated sandstones. We notice it seems really difficult to distinguish between the 'dry' (blue) and gas-saturated (green) bulk moduli. At 80% gas saturation (i.e., 5% oil and 15% brine), the separation between the 'dry' and gas-saturated P-wave velocities visibly increase at the well sorted end. This small increase could have significant impact on interpretation. So a gas saturated rock should not be considered as 'dry'.

During this work, we noticed that at 80% gas saturation, the P-wave velocity was slightly lower than the 'dry' P-wave velocity. To account for this, we suggested that it was due to the increase in bulk density over the bulk modulus since gas has very low bulk moduli. The most unlikely scenario in gas wells would be cases (3) and (4) because we usually have some saturations of irreducible water and some oil.

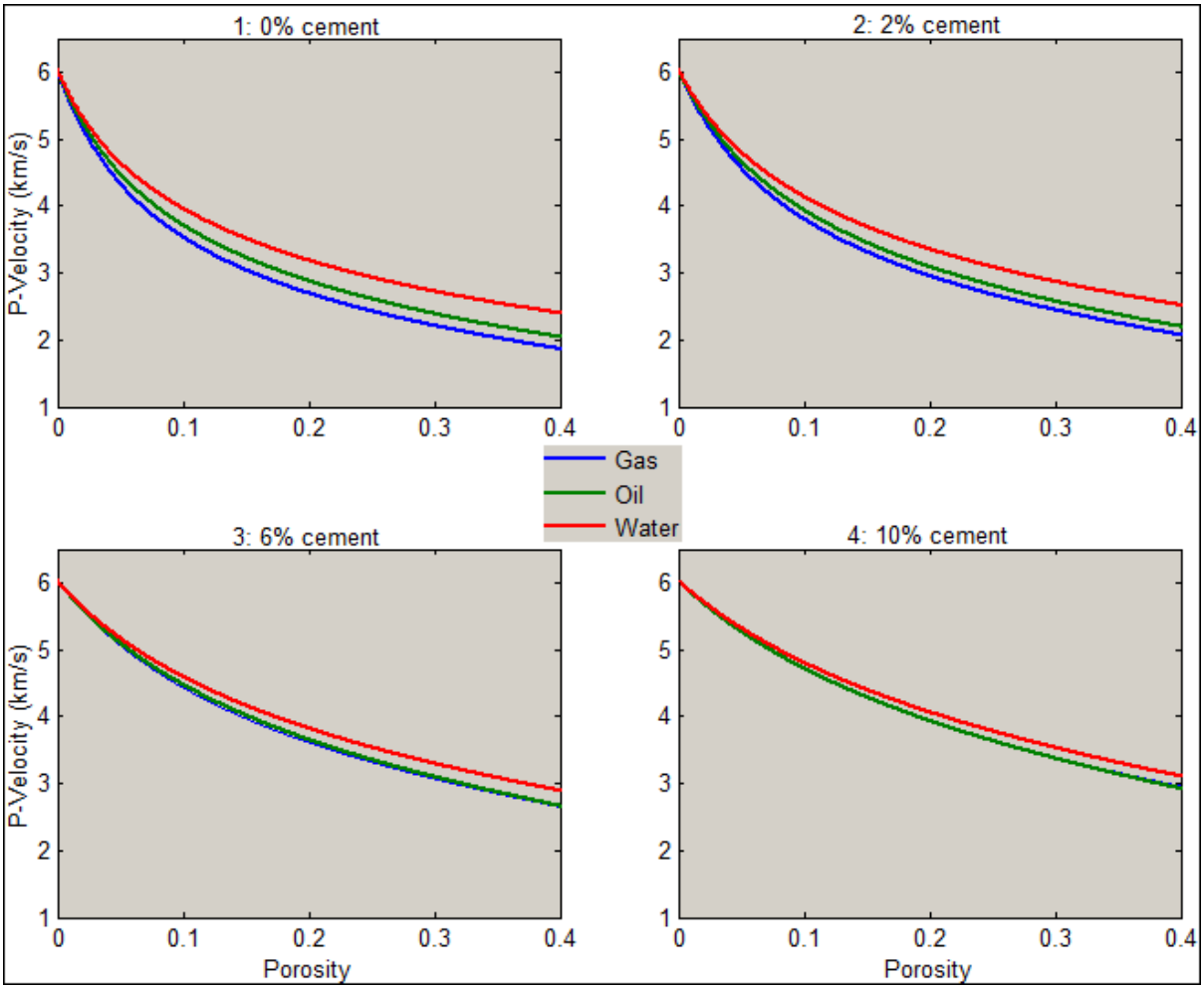

Figure 18: Model results showing 1: Friable sand model. 2: Constant cement (2%) model. 3: Constant cement (6%) model. 4: Constant cement (10%) model in a P-wave velocity vs. porosity cross-plot. notice the decrease in fluid sensitivity as we increase cement content. Effective pressure is20MPa and temperature is 70^{0}C. The lines represent 100% saturations for water (red), oil (green), and gas (blue).

Figure 18 shows the constant cement lines of various cement volume as P-wave velocity plotted against porosity. We notice there is a gradual decrease in fluid sensitivity as we increase cement content. The hydrocarbon-saturated lines are almost indistinguishable beginning from about 6% cement volume while brine remains distinct even at a relatively high cement volume. The decrease in fluid sensitivity with increase in cement is due to the effect cement has on the elasticity at the grain contacts and/or surfaces of the sandstones. The elasticity at grain contacts of the friable sand model is higher than that of the cement lines. This further declines as more cement is added, resulting to lower fluid sensitivity of the parameters.

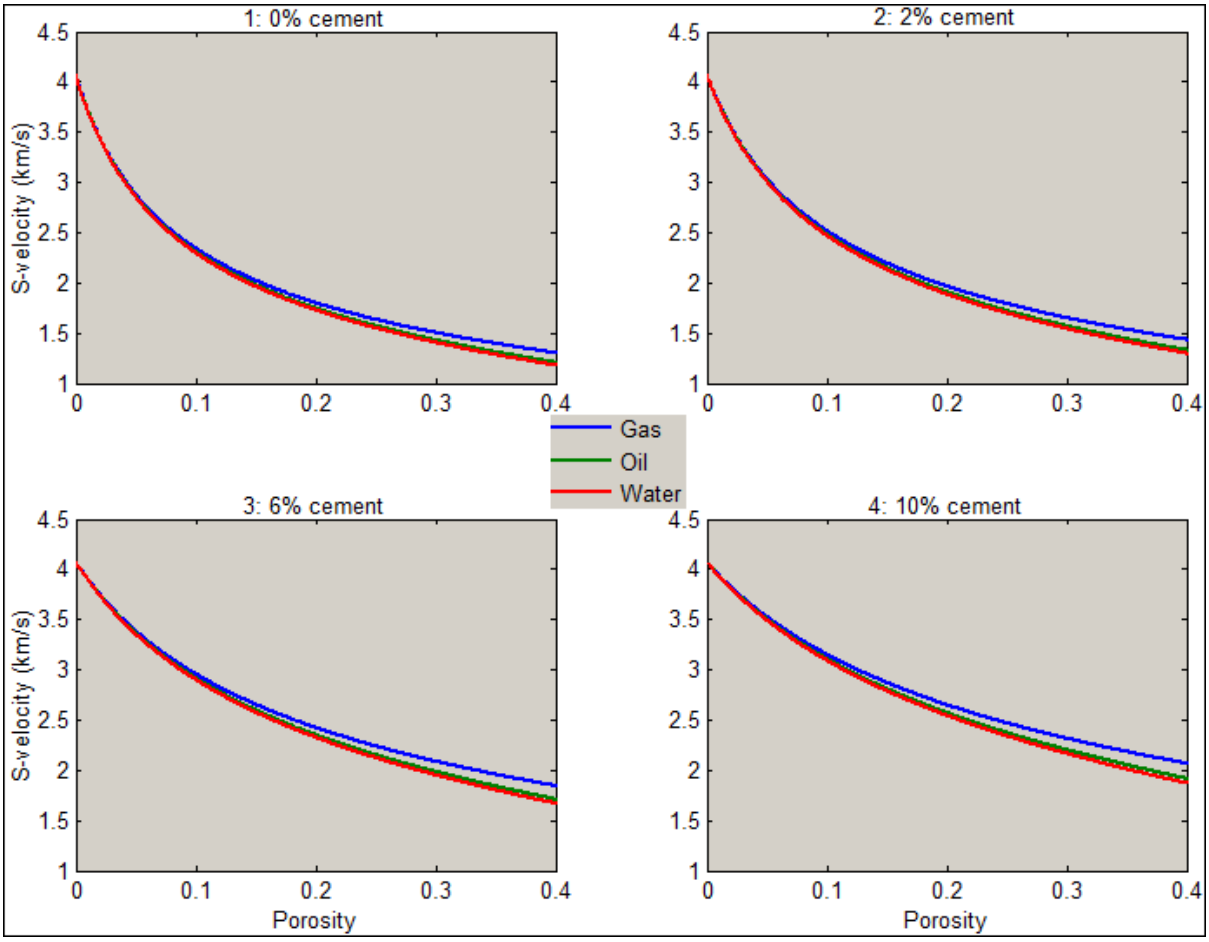

Figure 19: Shear wave velocity vs. porosity for sandstone. The models are constant cement lines and represent 100% saturations for water (red), oil (green), and gas (blue). Effective pressure is20MPa and temperature is 70^0C. The shear velocity is increasing with increase in cement but the separation between the lines is almost constant.

Figure 19 illustrates the degree of insensitivity of shear wave velocity to fluids. We see that unlike the P-wave velocity that showed good separation between the saturated lines, we can assume that there is a constant separation of the lines on the shear wave velocity vs. porosity cross-plot. The increase in velocity from 1 – 4 on the figure, is caused by the increase in cementation. We have seen that in both velocities, increase in cement volume increases the velocities. We see that as cement increases, the shear wave velocity is also increasing but the separation of the fluid lines is almost insignificant. The change in the shear velocity is mainly due to the change in the composition of lithology. Also notice that the dense fluids on figure 19 plot at lower velocities regardless the cement volume. This is because the shear modulus is approximately constant for all fluid saturations and increasing the fluid density therefore would increase the bulk density, resulting to a lower shear velocity.

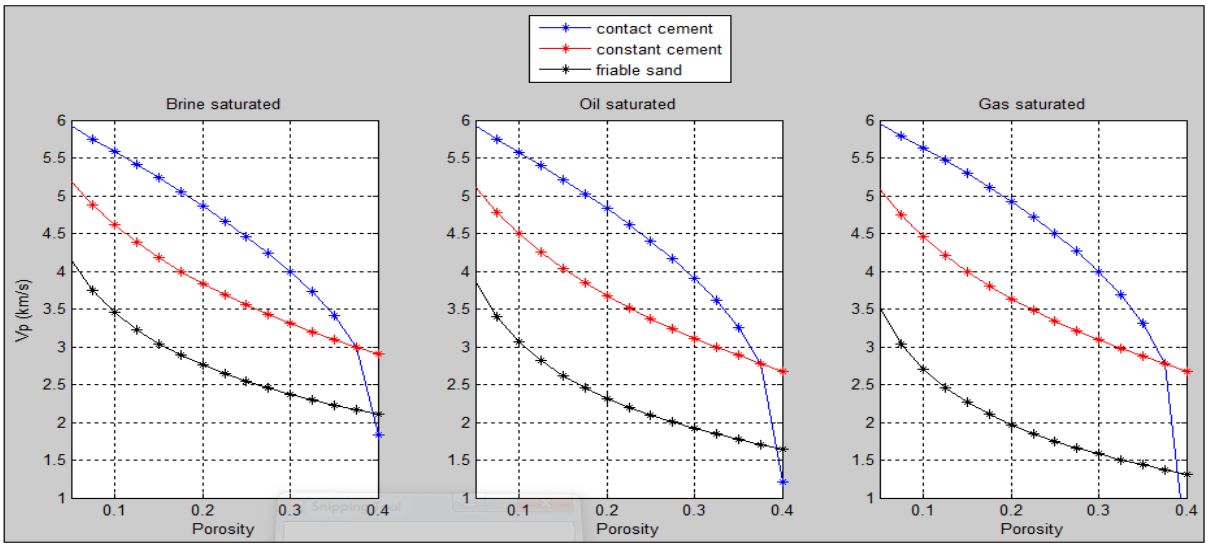

Figure 20: Vp versus porosity for various fluid substitution using the friable sand (black), contact cement (blue), and constant cement (red) models for clean sands. The friable line is modelled at 70^0C and pressure of 20MPa. All fluid parameters for the models are also measured at same temperature and pressure conditions. We also notice here that Vp is sensitive to fluid changes and the effect is higher when we have less cemented lithology.

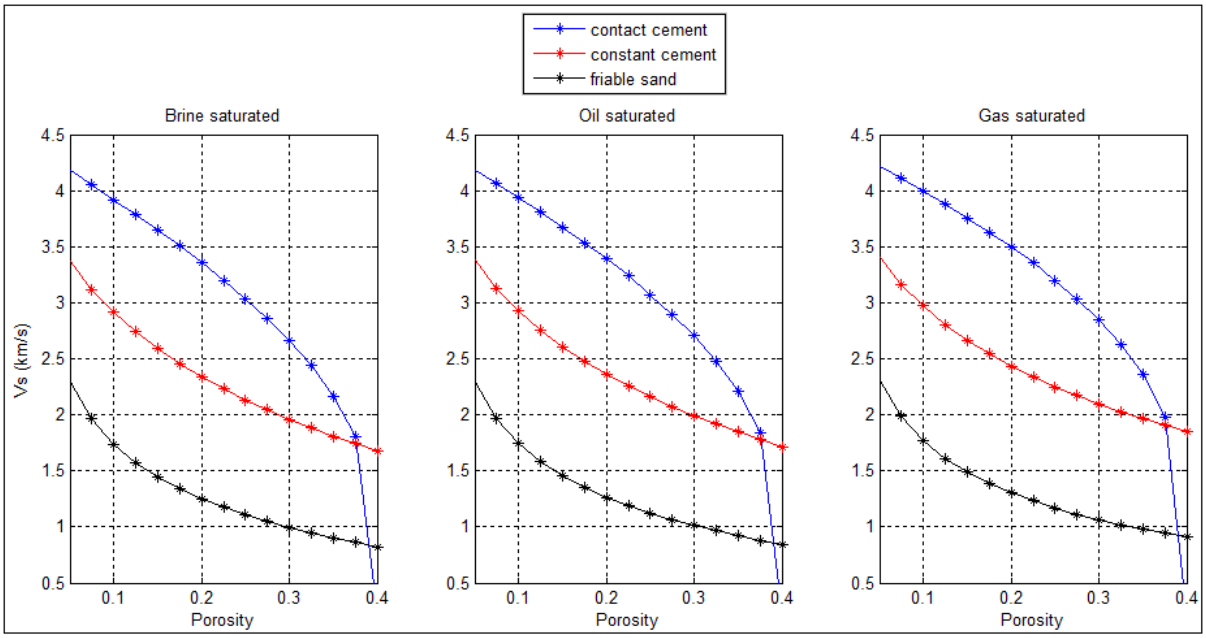

Figure 21: Vs versus porosity for various fluid substitution using the friable sand (black), contact cement (blue), and constant cement (red) models for clean sands. The friable line is modelled at 70^0C and pressure of 20MPa. All fluid parameters for the models are also measured at same temperature and pressure conditions. We notice again that for all the models, changes in the fluids results to only small changes in the shear velocity.

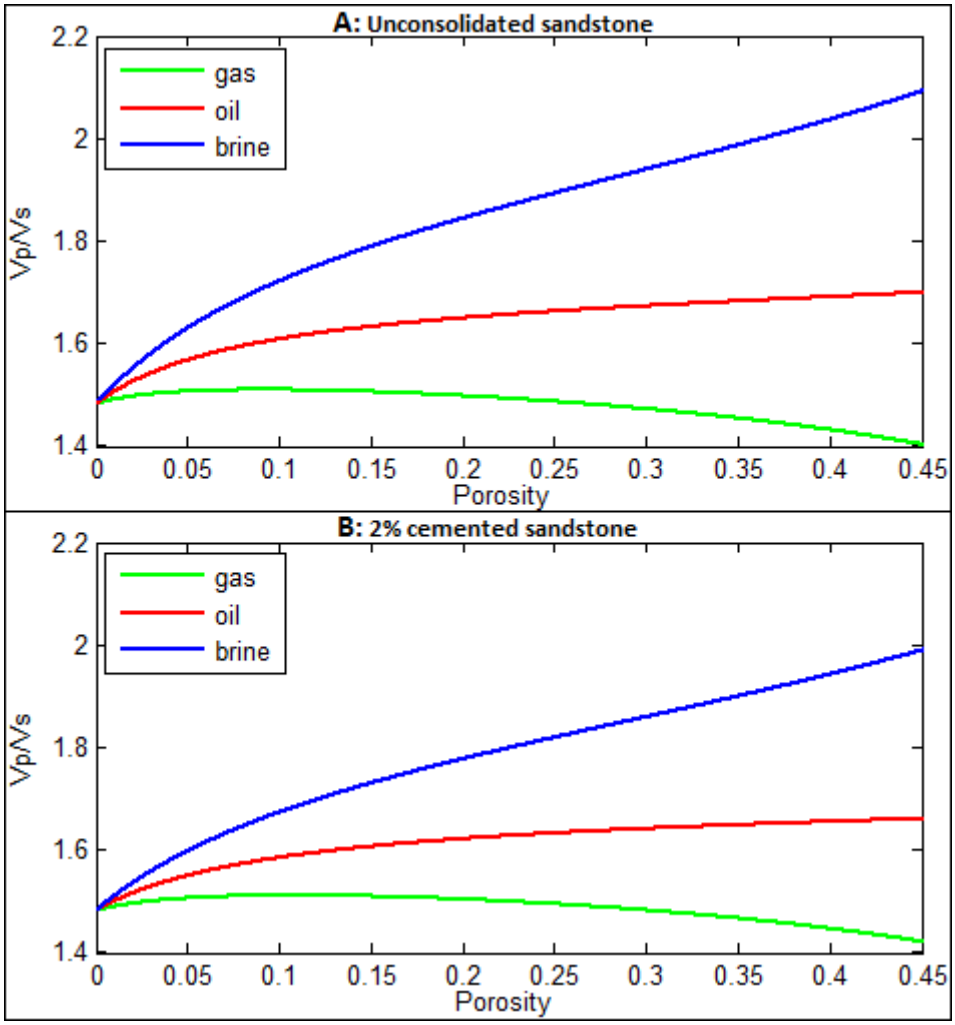

Figure 22: Theoretically derived model for velocity ratio versus porosity. The lines are constant cement models saturated with water (blue), oil (red), and gas (green). A remarkable separation was observed for both unconsolidated (A) and poorly cemented (B, 2% cement) sandstone models. The sensitivity was however higher in the unconsolidated model. From this, we see that Vp/Vs seems to be very sensitive to both fluid and lithology. This presented us a useful tool for our final analysis as we interpret both effects together with geologic trends. Effective pressure is20MPa and temperature is 70^0C.

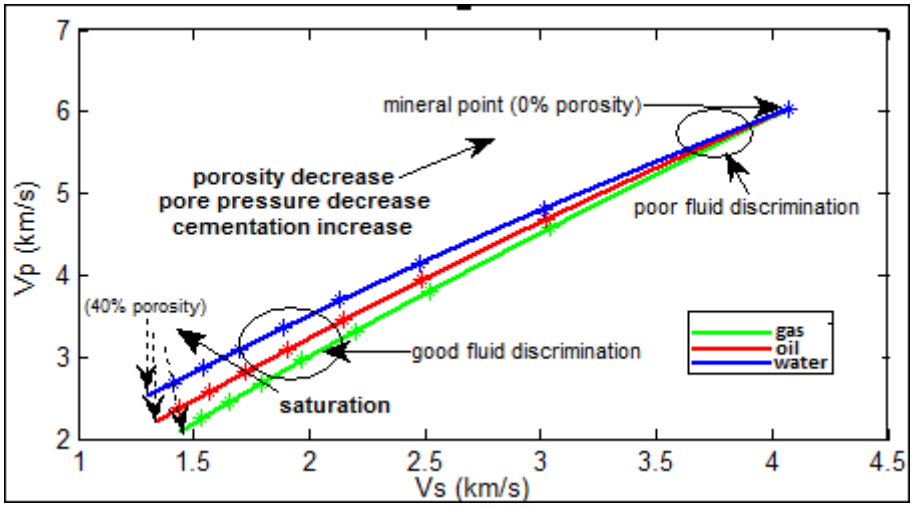

Figure 23: Theoretically derived Vs vs. Vp with constant cement lines of 2% cement. The lines are constant cement models saturated with water (blue), oil (red), and gas (green). The isolated lobes represent regions of good fluid discrimination (approaching high porosity end-member) and poor fluid discrimination (towards low porosity end-member).

Figure 23 shows a plot for Vs vs. Vp. At very high velocities (as we approach zero porosity) we see that the fluid discrimination is very poor. As porosity increases, the rock becomes softer and we see a clear discrimination of the fluids; water (blue), oil (red), and gas (green). This also ties with the illustration of Avseth et al., 2005. In this study we have made use of the Greenberg – Castagna sandstone and shale lines by superimposing them on in situ data. Comparisons of these have been made with the famous mud-rock line and also the dry rock line. This is shown in section 4.6.1.

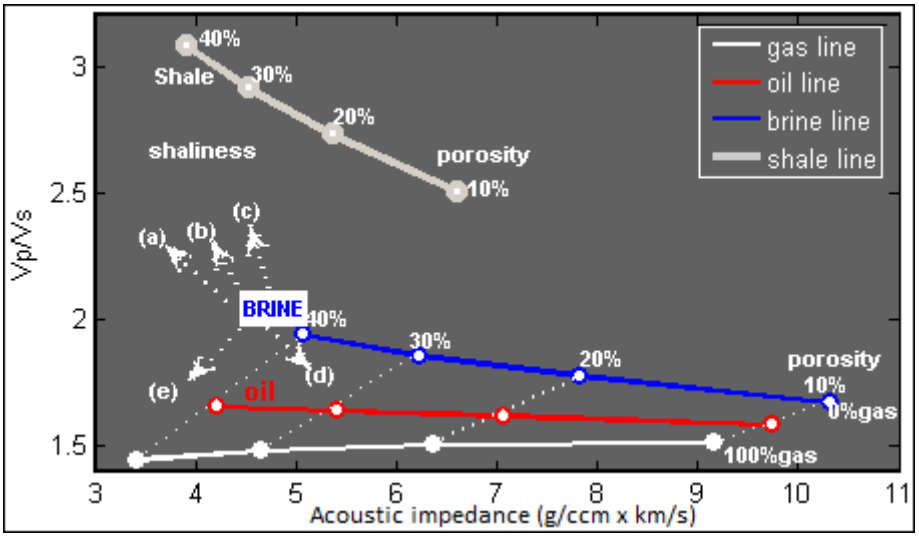

Figure 24: Acoustic impedance vs. velocity ratio predicted theoretically as a rock physics template. The white (gas), red (oil), and blue (brine background) lines are sands while the grey line is shale. The oil- and brine lines are 2% cemented while the gas line is not cemented. Effective pressure is 20MPa and 70^{0}C for the sands while effective pressure is 18Mpa and 50^{0}C for the shale. The following trends are observed: (a) Increasing porosity (b) Decreasing effective pressure (c) Increasing shaliness (d) Increasing cement volume (e) Increasing gas saturation.

Figure 24 shows the classical rock physics template employed for this study. The brine line (blue), oil line (red) and the gas line (white) are the constant cement models. The values of fluid bulk moduli and densities were computed at pressure 20MPa and temperature 70 degrees Celsius. The shale line (grey) is the friable shale model computed at pressure, 18MPa and temperature, 50^0C. It was observed that the higher the rock bulk modulus relative to the shear modulus, the higher the Vp/Vs ratio. Hence, the shale line plots at higher ratios. This means that for the same lithology saturated with different fluids, the lithology containing the fluids with higher bulk modulus will plot at higher Vp/Vs ratios. Hence the gas sands are lower than the oil sands, and the oil sands are lower than the brine sands in terms of Vp/Vs as we observe on figure 25. This makes Vp/Vs a very good fluid and lithology discriminator.

The trends observed can be used as a guide during seismic interpretation as failure to understand these trends could be a pitfall in interpretation.

4.3. Well Log Analysis

Several logs have been provided for well-A including the shear wave log. Greenberg – Castagna empirical relations were used for shear wave prediction and the result showed that the provided shear log was good. Only the logs needed for rock physics studies were extracted from the provided logs. The main input logs were the P-wave velocity (Vp), S-wave velocity (Vs), and the density (Rho) logs. The given data had a good porosity log. To check this, another porosity log was created and the result was also identical to the given porosity log. Larinov's 1969 non-linear empirical method for estimating volume of shale was employed, using the gamma ray (GR) log as source log and was assumed a proxy for the volume of clay in the rock. The main working intervals focused within the reservoir sandstones but other working intervals were created for shale data analysis. Both the MATLAB and ROKDOC softwares have been used for data plots.

In this work, 5 wells were provided but some of the wells did not have sufficient logs. Only one well, N24/6-2, has therefore been considered for detail studies. We will denote this well as **well-A**. However, some of the other wells have also been analysed in some regard and compared with the main well.

The main well.

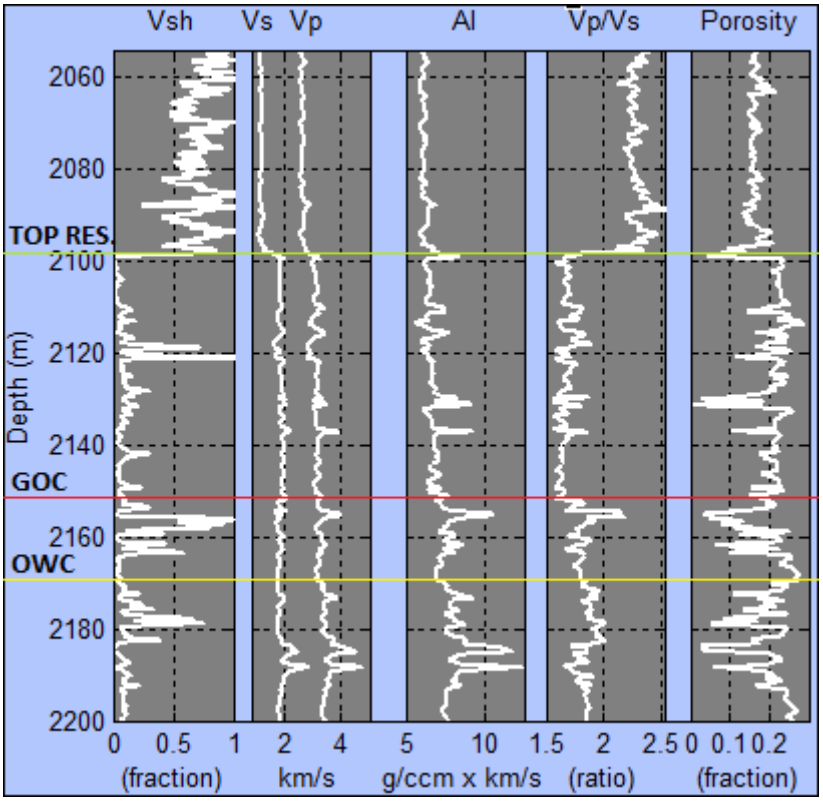

Figure 25: Log Check Plot. This is the view of the some logs used for this study. The depth interval shown includes the Lista Formation cap-rock shale (2054m – 2099m) and part of the Heimdal Formation (2099m - 2200m). The whole log interval is between 1250m to 2750m (MD) but most of the shallow depth has been cut off due to some misleading data. The horizontal lines represent the top reservoir (green; 2099m), the gas-oi-contact (red; 2151), and the oil-water-contact (yellow; 2168).

Figure 25 shows some of the input well-A logs that have been used for data analysis. Volume of shale (Vsh) was estimated from the gamma ray which was assumed to indicate the presence or absence of clay because the GR log measures radioactivity and most clay minerals are usually associated with radioactive elements. Contrary to this, the high Vsh readings down in the oil zone could be misinterpreted as shale. They actually are laminations made up of much more finer sediments. This could be misleading especially if we do not have fore-knowledge about the geology of the subsurface we are interested in. The clay particles present here could be hardened in the sands. In fact, here we have shaly sands. Where the Vsh log shows very low values has been assumed to be sand and depending on the fraction, we have described various zones as sand (close to the reservoir top), shale (above the reservoir) and shaly sands (at depth about 2120m). From figure 25, we see that the at depth before 2100m, the clay content is relatively very high and this could be shale. This drops drastically at depth of about 2100m, where we have the top reservoir (green horizontal line). Such a drop in Vsh would suggest a transition from a clay-rich to an almost-clay-free lithology. More detailed studies have been carried out in this well by Avseth et al., 2009 who have analysed thin section from samples of the well at depth 2154m. Their analysis showed that the sandstones exhibit some clay material at this depth and together with organic matter, these clay materials coat the sand grains. There is some

initial cement at the target zone. For this reason, we have described the sandstones in well-A as poorly cemented. We would later see the significant effect of the small amount of calcite cement on the elastic properties of the rock during cross-plot analysis. Results from other cross-plot analysis also show the presence of some clay in the reservoir as we have observed from the logs.

The P-wave velocity (Vp) and the acoustic impedance (AI) logs show some good correlation. Slight differences would be due to the density since AI depends on both Vp and density. Vp shows similar trends as the shear wave velocity (Vs) but they differ very much at the gas-oil contact (GOC) as can be observed on figure 26.

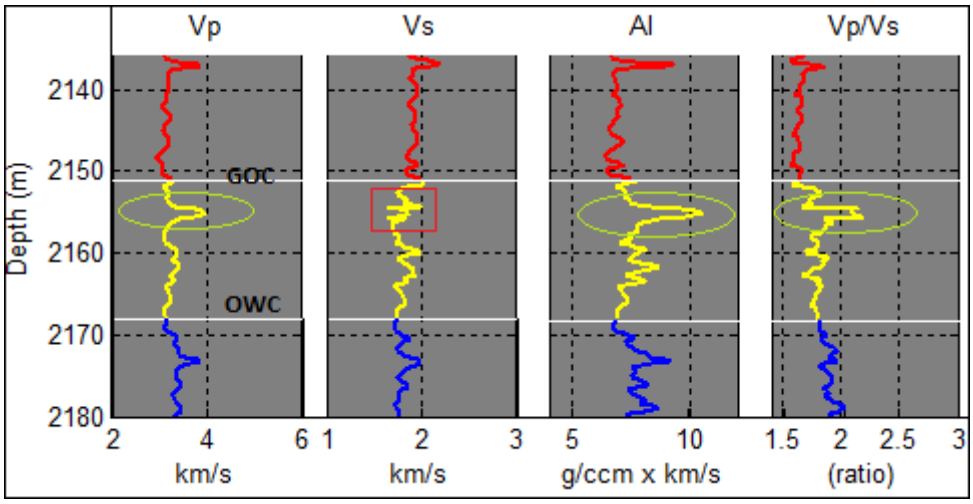

Figure 26: A closer look at the velocities, acoustic impedance and velocity ratio at fluid contacts. The red curves represent part of the gas zone above while the blue curves represent the water zone below the oil-water-contact. Between them is the oil zone. Notice that Vs is relatively not changing (red rectangle) as the other logs at the fluid contacts (lobes). Increasing Vp with an almost constant Vs means increase in Vp/Vs as we observe and without a change in lithology (difference in density), AI would increase accordingly.

At about depth where we find the gas oil contact, we notice considerable difference between Vp and Vs. The GOC has been indicated at depth 2151 as given from literature studies (Norwegian Petroleum Directorate, NPD). If we consider a kelly bushing value of 23.3, we may further have our GOC closer to the lobes in figure 26. Here we see a clear increase in Vp but not in Vs. Within the same lithology, such increase in Vp would suggest a movement from a fluid with low velocity to one of higher velocity. The corresponding increase in Vp/Vs ratio indicates that the fluid below has a higher bulk modulus (we assume they both have zero shear

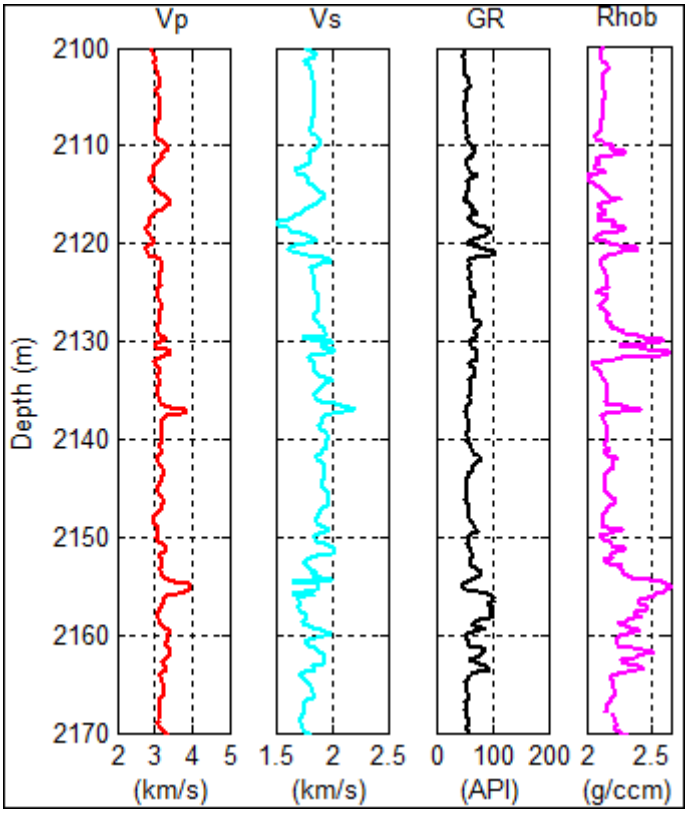

Figure 27: Log responses of velocities, densities and gamma ray within the depth interval that embodies the reservoir in well-A.

Figure 27 shows in situ data for velocities, gamma ray and density. For the mixed lithologies, the volume of shale log was used to deduce fraction of shale in the lithology. From a general perspective, we get the impression that Vp and Vs are curves are almost similar in shape. Both Vs and Vp are higher in the sandstones than embedding shale, even though the densities are lower. This shows that the mineral moduli and elastic stiffness of the sands is much higher than for the embedding shale.

4.3.1. Generating other logs

As already mentioned, the volume of shale log was generated using the gamma ray as a proxy for clay fraction. It was estimated using both linear and non-linear empirical responses. The non-linear responses include Larinov (1969) for Tertiary rocks and older rocks, the Steiber (1970), and the Clavier (1971) response equations. These equations are based on the geographic area and age. For this study, the Larinov (1969) response equation for Tertiary rocks has been used to calculate volume of shale.

The sorting log was also determined using the simple equation;

Sorting = porosity/critical porosity

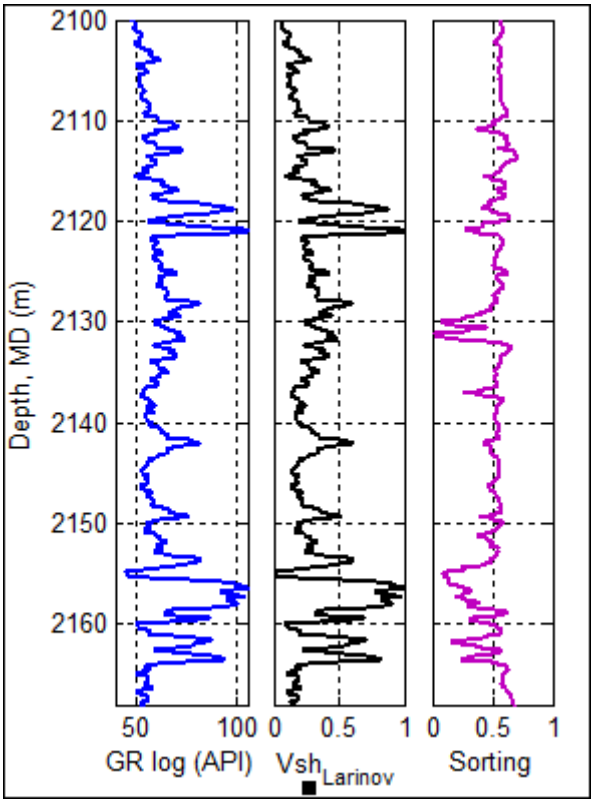

Figure 28: Figure showing the gamma ray, the derived non-linear Larinov (Tertiary) shale volume, and sorting logs for the target zone in well-A.

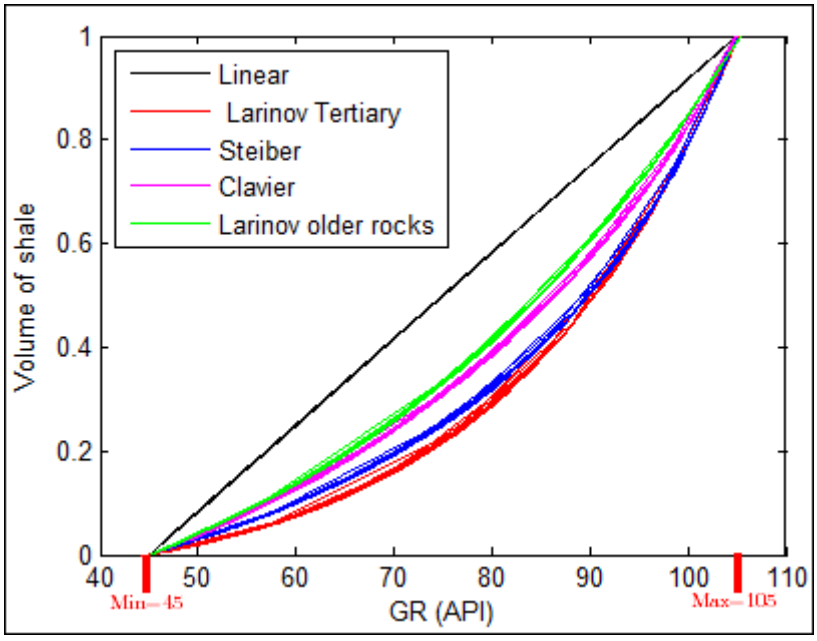

Figure 29: Comparison of shale volumes derived from various response equations plotted against gamma ray. We see that the Larinov curve for Tertiary rocks is the most curved while the Larinov curve for older rocks is the least curved. The Linear response curve plots as one would expect.

4.4. Cross Plot Analysis

Cross-plot analysis in rock physics shows us how the rock physics parameters vary with fluid and lithology. We also investigate the effect of geologic factors such as mineralogy, clay content, sorting, diagenesis, and bedding configuration on fluid and stress sensitivity in the rocks. In this section superimpose rock physics models on in situ data for more detail analyses.

Table 4: The depth intervals embodying target zones to be analysed.

Fluid	Interval
Gas	2099 – 2152.37m
Oil	2152.37 – 2168m

4.4.1. Porosity modelling

Here we are going to show how rock physics models discussed in the preceding sections are superimposed on in situ data for analysis. We have used elastic moduli for porosity modelling. These moduli have then been used after fluid substitution to calculate the velocity trends for different fluids. The data have been analysed using mostly the Hertz-Mindlin plus modified Hashmin-Shtrikman bounds for unconsolidated sands because we have used data from a poorly-consolidated sand reservoir. However, we also investigate the presence of a few cement materials which could account for the relatively high velocities at some regions within the reservoir as we earlier observed on the velocity logs.

The gas zone

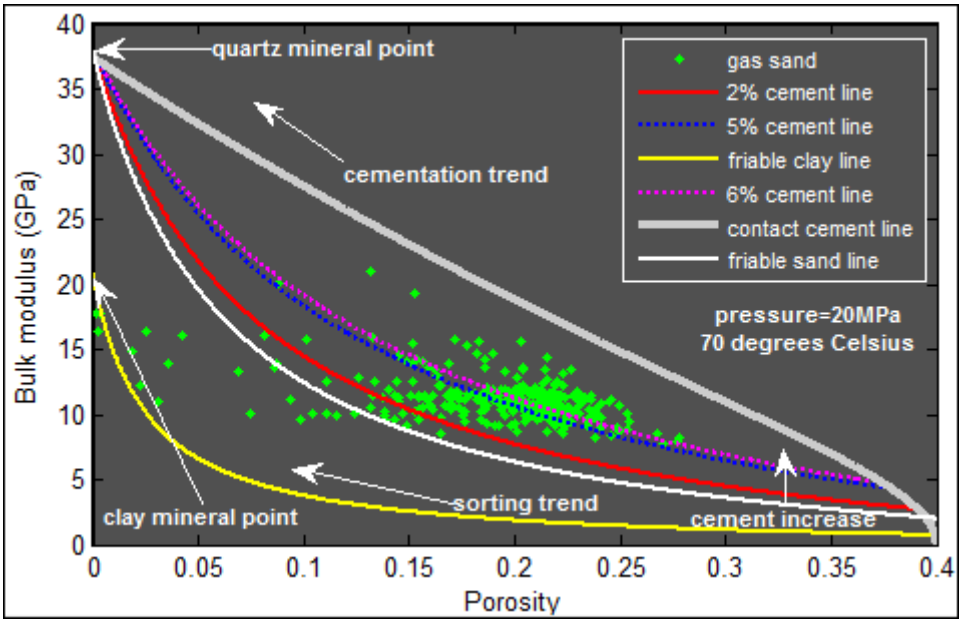

Figure 30: Bulk moduli versus porosity cross-plot for gas zone in well-A with rock physics models superimposed on in situ data. The constant cement lines are 2% (red), 5% (blue), and 6% (magenta). The white line is the friable sand line while the yellow line is the friable clay model. The contact cement model is grey. All sand and cement lines gas-saturated. The 5% and 6% cement lines fall nicely on the data.

Figure 30 shows data for the gas zone in well-A superimposed with gas-saturated rock physics models. The constant cement lines for 5% 6% cement fall nicely on the data. We see that the higher the cement content, the higher the rock stiffness. We also notice that data are plotting towards the contact cement line. From the figure, one would think that the sandstones are more than just slightly cemented. One reason for this is that at shallower depth, shear wave velocity picking could sometimes be lower. This would give us low shear modulus values and would lead to increase in the bulk modulus.

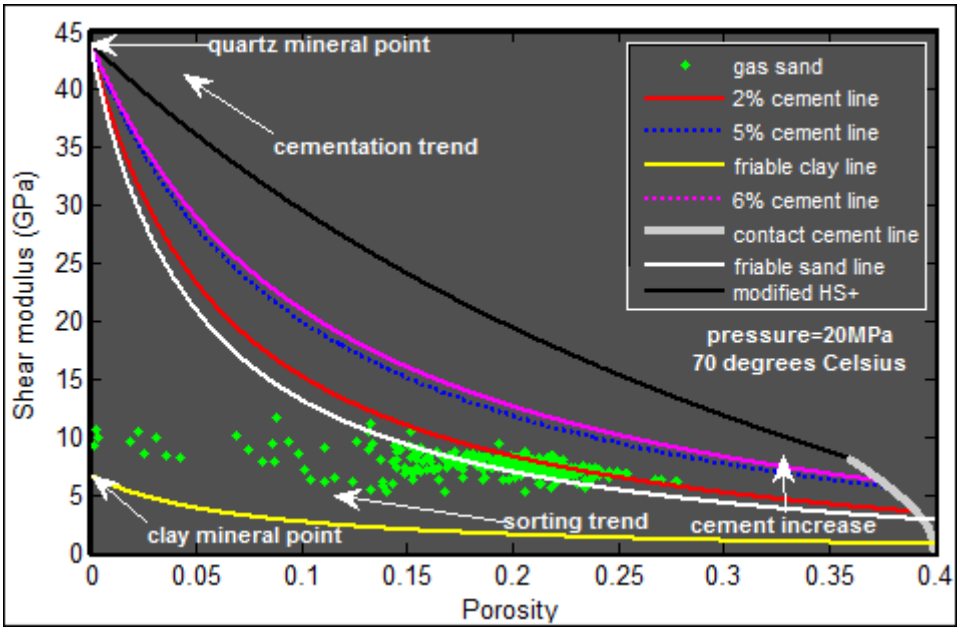

Figure 31: Shear modulus versus porosity using in situ data from well-A with superimposed rock physics models. The constant cement lines are 2% (red), 5% (blue), and 6% (magenta). The white line is the friable sand line while the yellow line is the friable clay model. The contact cement model is grey. The black line represents the modified Hashmin – Shtrikman upper bound. We see the data fitting well on lower cement line (about 2%).

Unlike on figure 30 where we had the constant cement line for 5% and 6% cement falling nicely on the in situ data, figure 31 shows the 2% cement line as the best fit of the cement lines shown. The friable sand line (0%) also falls on some data. None of the sandstone reservoir sandstones plots close to the 5% constant cement line. As we mentioned earlier, the shear information could actually be a bit lower than we would have expected due to shallow depth velocity picking. We would take a look at the velocity – porosity relations of the same zone and thereafter, analyse the oil zone and also compare any observed differences.

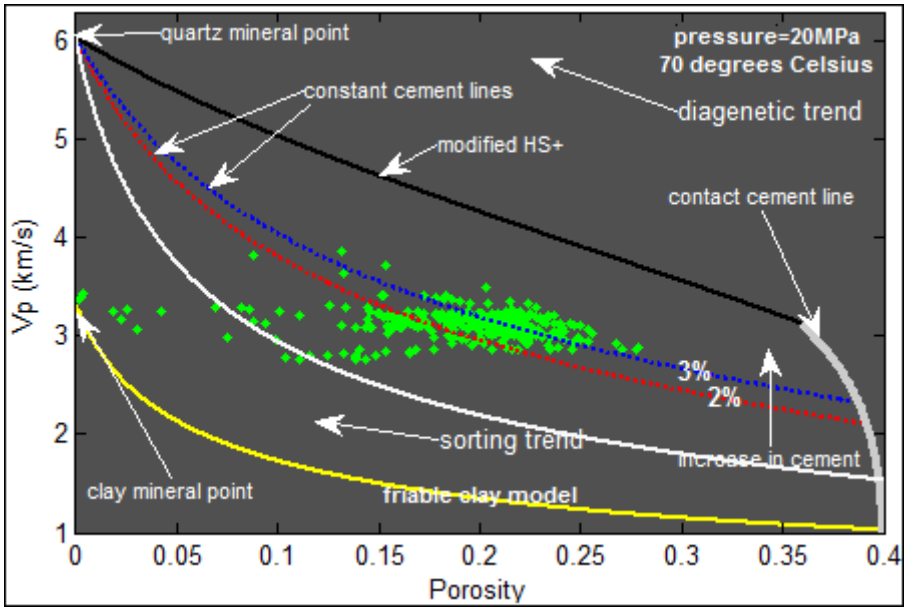

Figure 32: Vp versus porosity for gas sands in well-A with rock physics models superimposed on in situ data. We see a good match of the data with the 3% cement line (blue) with some data falling on the 2% cement line (red). The white line represents the friable sand line (slip factor applied). Observe that the sorting trend of the data shows almost no change in the velocity and shows some scattering effect towards the friable clay line (yellow). This may be the effect of clay in the gas sands as we saw from the volume of shale log.

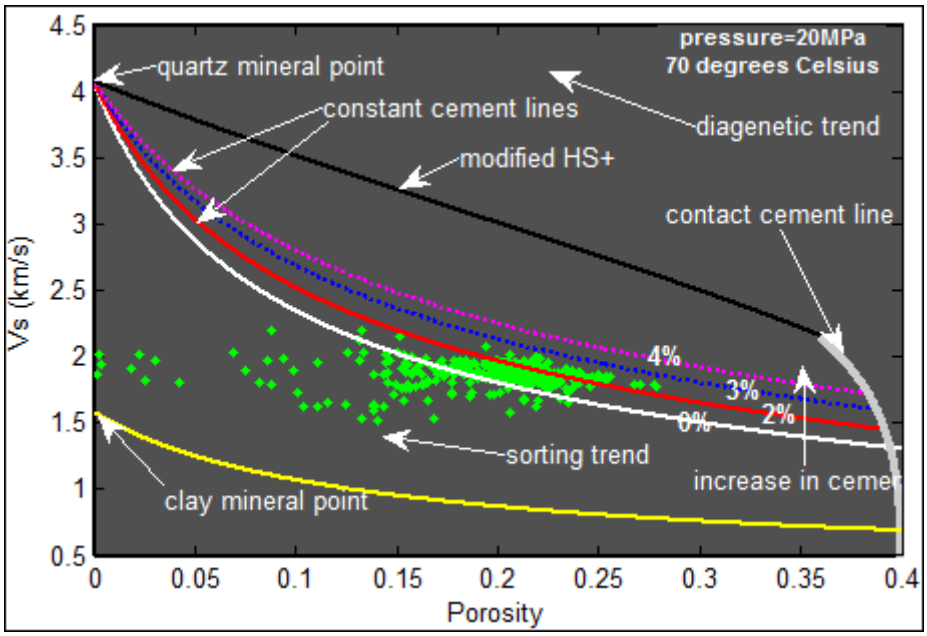

Figure 33: Vs versus porosity for gas sands in well-A with rock physics models superimposed on in situ data. We see a good match of the data between the friable sand line with no slip factor (white) and the 2% cement line (red). We noticed that without the slip factor applied, the presence of as small as 1% cement may not be noticed which would cause a significant effect on velocities. Again observe that the sorting trend of the data shows almost no change in the velocity and shows some scattering effect towards the friable clay line (yellow). This plot looks similar to that of the shear modulus – porosity plane in figure 31 in terms of which cement lines fit on the data. So, picking low Vs would lead to low shear modulus as well. The various lithology lines reach their respective mineral points at zero porosity.

The oil zone

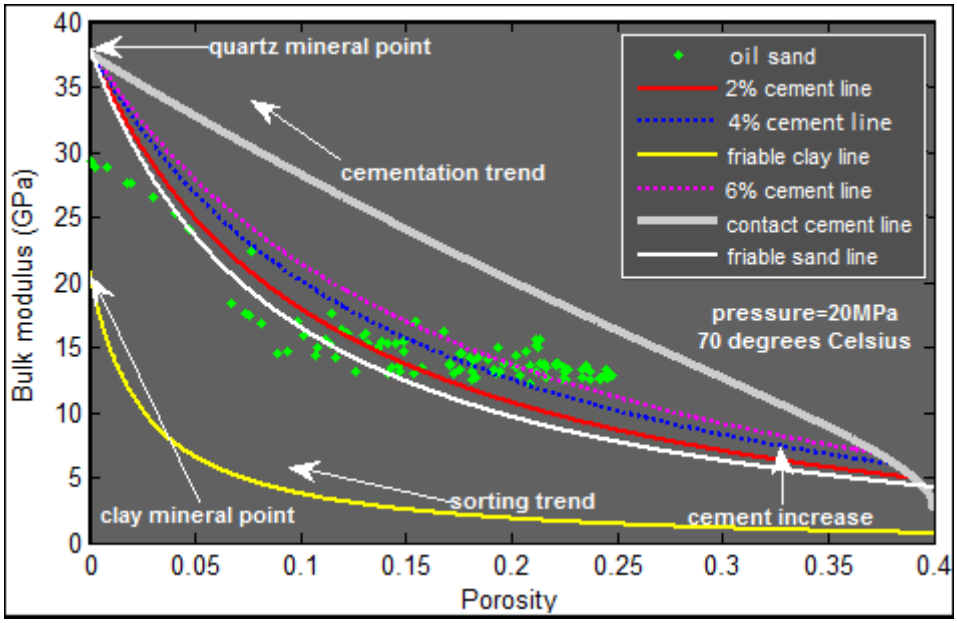

Figure 34: Bulk modulus versus porosity with rock physics models superimposed on in situ data at oil interval from well-A. The fitting constant cement lines here are around 4% (blue) and 6% (magenta). We observed a similar fit on the bulk modulus – porosity plane for the gas zone. This suggests that they may contain similar cement volumes. The grey line is the contact cement model.

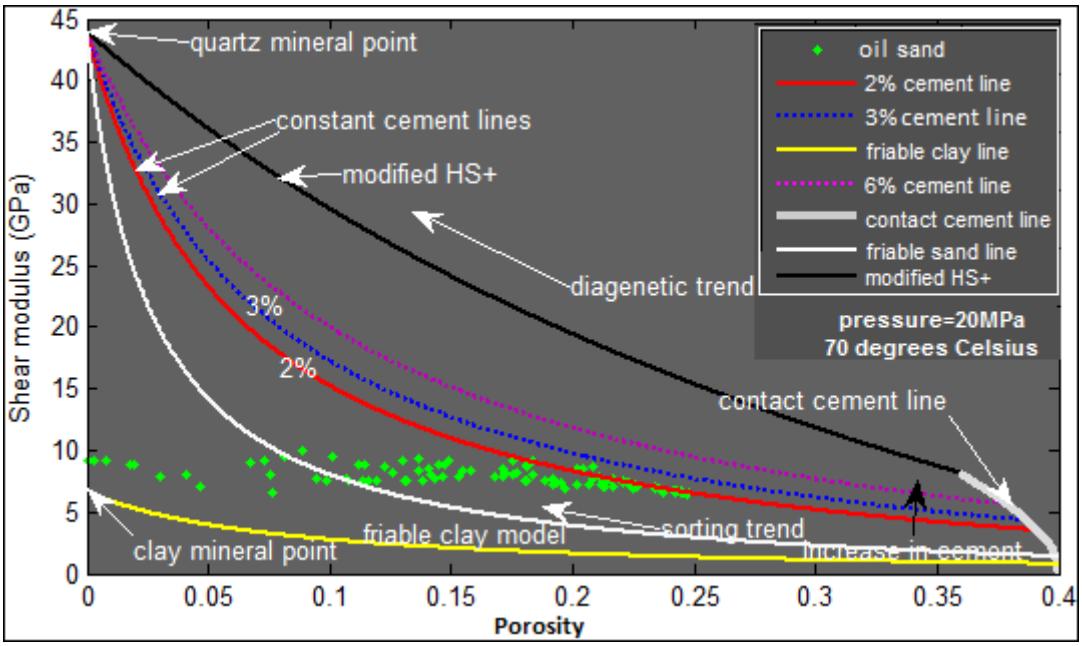

Figure 35: Shear vs. Porosity for oil sands in well-A using rock physics models superimposed on in situ data. Notice the similarity here with the gas zone in figures 31 and 33. The most data are plotting between the friable sand line (white, slip factor was applied) and the 2% constant cement line (red). The upper cement lines are 3% (blue) and 6% cemented (magenta). The black line is the modified HS bound while the grey line is the contact cement line. We also see the effect of shale as data move towards the shale line (yellow) with the effect of decrease in sorting.

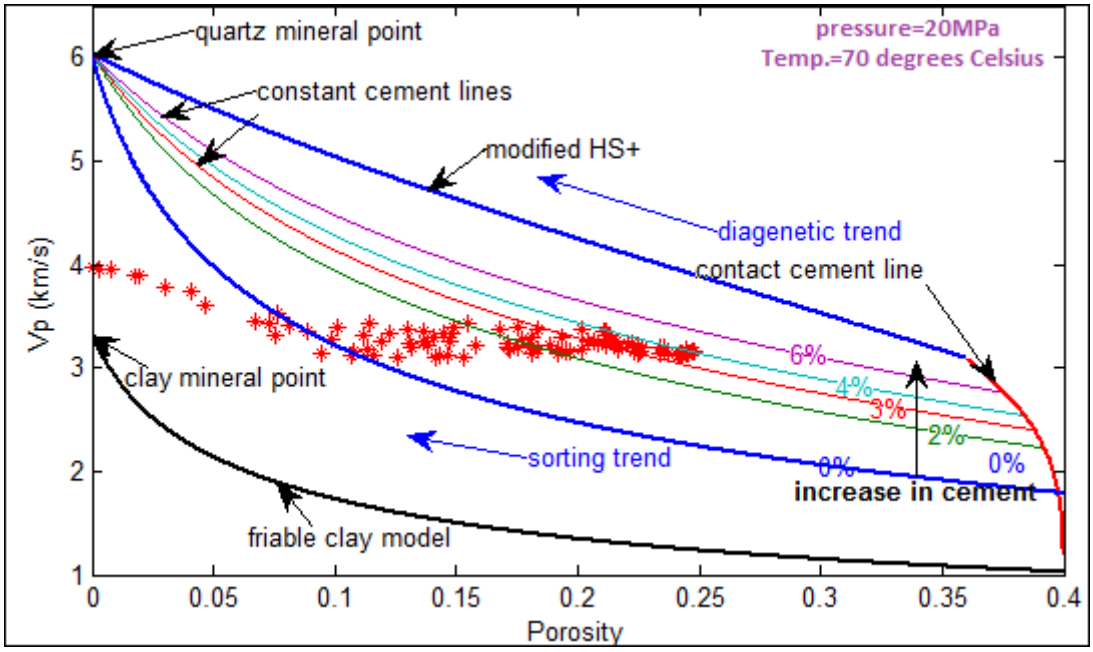

Figure 36: P – wave velocity versus porosity for oil sands in well-A using rock physics models superimposed on in situ data. We see that the most clustered data plot between 3% (thinner red line) and the 4% (cyan line) constant cement lines. Almost no change in velocity as the sorting decreases. This suggests that we may have laminations of clay material although we do not also notice any evident reduction in the velocity. The 0% cement line (lower blue) and upper blue line represent the modified Hashmin – Shtrikman lower (with slip factor) and upper bounds + Hertz – Mindlin theory for unconsolidated sandstone respectively. The few data points plotting at relatively high velocities at the low-porosity end-member may be some effect of noise in our data.

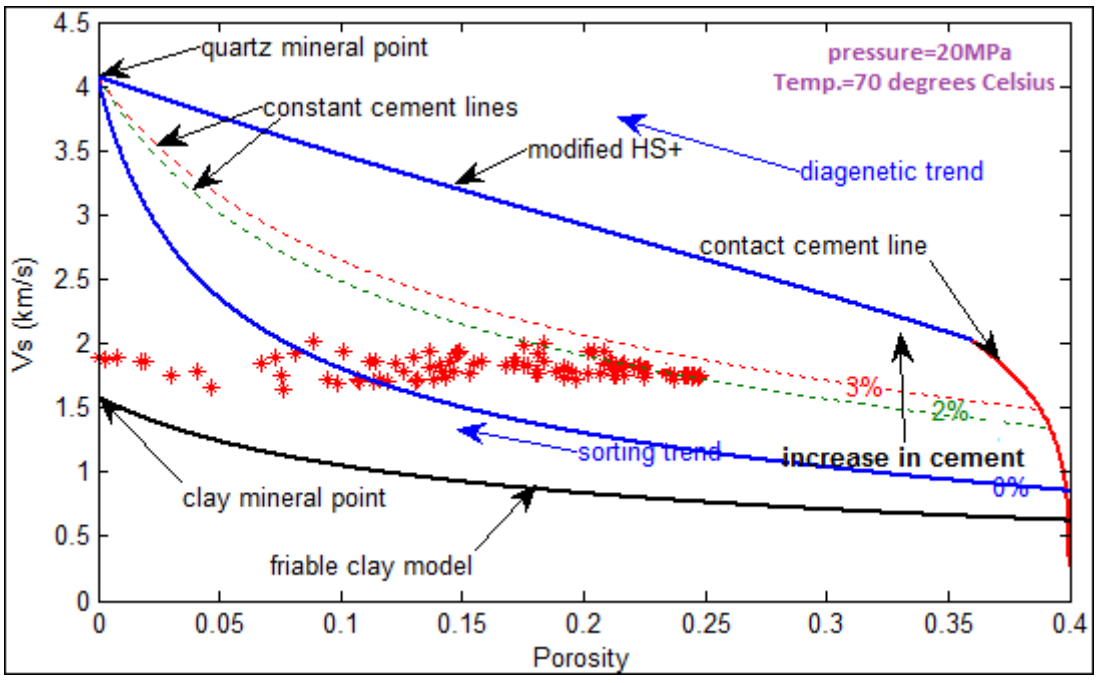

Figure 37: Vs versus porosity for oil sands in well-A with rock physics models superimposed on in situ data. The 2% cement (green), 3% cement (red), and the 20% shaly sand (grey) lines fall on data points. We interpret this as shaly sands with some cement between 2% and 3%. The lower blue line is the modified Hashmin – Shtrikman lower bound plus Hertz – Mindlin theory and slip factor correction has been applied. Contact cement model (grey) and modified HS upper bound (top blue) are also superimposed. We see that most data fall above the lower bound suggesting some cement and some towards the shale line (suggesting some clay).

4.5. Analysis of Lithofacies

As mentioned earlier, the gamma ray log has been assumed a good indicator of clay content in rocks or sediments. This has provided a platform for the possibility to use the gamma ray log in the determination of the various facies within the subsurface. In this study, sand content has been assumed to be mainly quartz while shale has been assumed to be mainly clay. This may differ in other studies where more detailed analysis is carried out as rocks usually contain not only single minerals.

We present our arguments and illustrate the basis of our interpretation of the facies. We would want to mention that conclusions should not be drawn entirely from our interpretation (since core samples analysis may be more reliable) but may however, serve as an insight to further research studies in the same area.

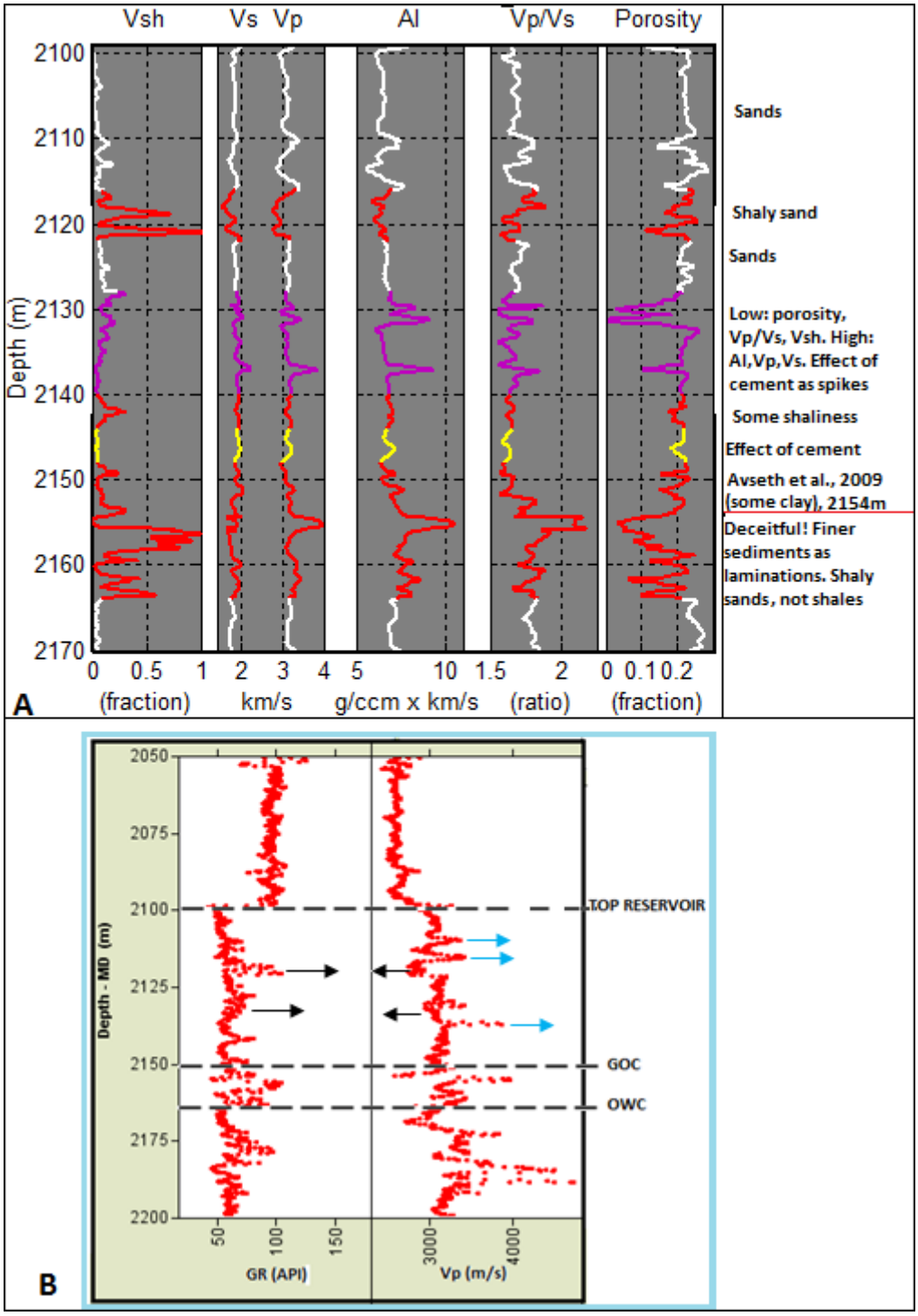

Figure 38: Plot shows the gamma ray and Vp log responses. The relatively very high velocities which look like spikes (blue arrows on bottom figure) within the reservoir do not correspond with the degree of GR decrease. This is probably as a result of some cement (calcite stringers). The top figure (A), presents the possible different groups of lithology with focus within reservoir interval.

From figure 38**B**, we see clearly above the reservoir (about 2100m) that this is shale (almost pure). We see that velocities are very low. Velocities increase remarkably at top reservoir. This suggests a sandstone lithology. But we notice variations in velocities and other parameters shown on figure 38**A**. We think these changes can be accounted for, in terms of

clay content and cement volume in sandstones. There are two possible effects of clay content in our reservoir sandstones on velocities.

1. If the clay particles are pore-filling, then the effect of the clay would cause a small increase in the velocity.
2. If the clay particles occur within the sands as laminations, then we would expect a softening effect of the clay on velocities resulting in low velocity values (possibly in within the oil zone).

Looking at figure 38 within the reservoir sands we can also observe that the velocities are decreasing with increase in clay content. By inference from the two possibilities mentioned above, it is logical to say within our reservoir in well-A, the clay present is laminated. That notwithstanding, we may be able to notice effect of pore-filling clay at a micro-perspective within our sands.

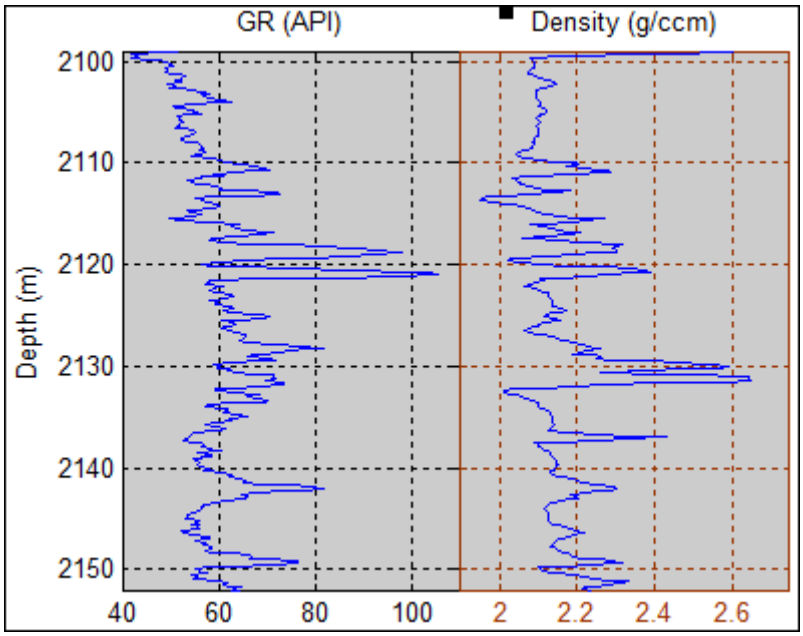

Figure 39: We see a good linear relationship between gamma ray and density. We notice a much higher density response at about 2130m relative to the gamma ray response. This could be related to the microstructure of the rock. It is possible that there is some cementation here and the sediments are losing porosity. This would in turn increase effective pressure thereby reducing the effective porosity. The lower the porosity, the more the bulk density approaches the mineral density (from equation 3.8)

4.6. Vp – Vs combinations

During this study, combinations of Vp and Vs have shown that they are a powerful tool in detecting both lithology and fluid type most especially as a ratio. We have seen from previous sections in this study that modelling porosity with elastic elastic moduli and velocities can tell us much about the stiffness of the rocks we investigate. We saw how the diagenetic trend can influence the rock frame and also how the sorting trend is influence by mineralogical changes. However, we noticed during this study that Vp – Vs relations (especially Vp/Vs) were seemingly better with respect to lithology and fluids. These relations

also serve as a direct seismic identification of pore fluids when analysing data such as in AVO analysis (Avseth et al., 2005).

In this section, we carry out the following;

- Establish some empirical relations between Vp, Vs, Vp/Vs, (Vp/Vs vs. porosity) using brine saturation as a reference pore fluid.
- Then, we use the Gassmann's equations described in section 3.2 to map these relations to oil and gas states.
- Next, we try to interpret geologic trends and their effects on the detectability of fluid and lithology.

Vp versus Vs

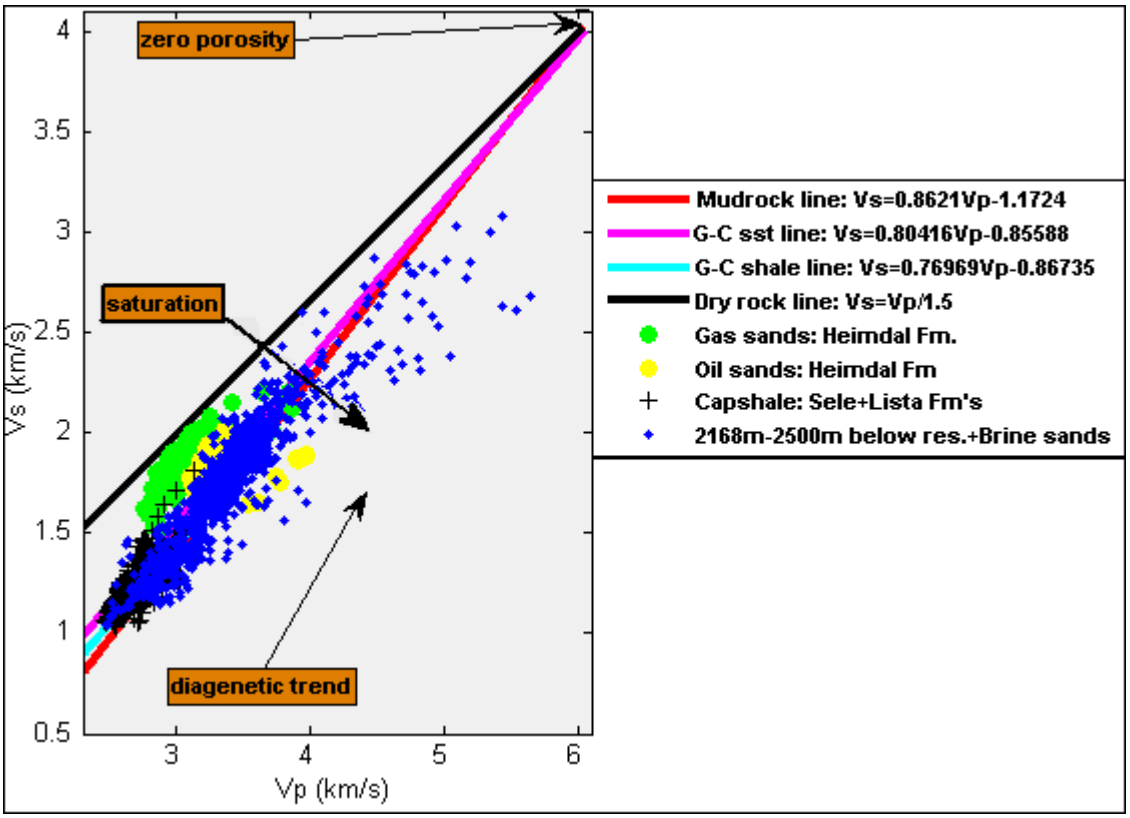

Figure 40: Logged data from well-A with superimposed lines: Greenberg-Castagna sandstone line (magenta), Greenberg-Castagna shale line (cyan), mudrock line (red), and the 'dry' rock line (black line). Notice that there is a better correlation with the in situ data of all the lines than the 'dry' rock line. Observing keenly from the 'dry' line, we could notice an increase in saturation from the gas sands (green), through the oil sands (yellow), and to the brine sands (blue). As we would expect, the cap-rock shale (black crosses) plot at low Vp and Vs values. The diagenetic trend increases with pore pressure decrease.

Figure 40 shows several rock lines superimposed on logged data from well-A. We used the Greenberg – Castagna regressions for sand and shale (Greenberg and Castagna, 1992) on

the in situ data. The sandstone lines are 2% cemented and we assumed 100% quartz sandstones. The shale line is assumed 100% clay. We see a remarkable fit between the shale line and the caprock shale (black crosses). We can notice that the brine sands have higher Vp values than oil and gas sands while gas sands have the lowest Vp values but relative higher Vs values compared to brine and oil sands due to the very low density of gas. We would therefore expect Vp/Vs ratios for the gas sands to be lower than those of oil and brine sands as we later see in the next section. The empiral lines show a diagenetic trend as velocities increase (i.e., decrease in pore pressure and porosity). At intensive diagenetic processes at greater depths (low porosity), we see very poor lithology and fluid discrimination.

Table 5: Regression constants for the Greenberg – Castagna empirical relation ($Vs= A_{i2}Vp^2+ A_{i1}Vp+ A_{i0}$).

Lithology	**A_{i0}**	**A_{i1}**	**A_{i2}**
Sandstone	-0.85588	0.80416	0
Shale	-0.86735	0.76969	0

We somehow found it challenging to make very reliable conclusions from the above figure but used it as an insight into expected Vp/Vs relations which turned out to be a better tool for lithology and fluid discrimination. Our conclusion was therefore that the use of Vp versus Vs would not be sufficient for our final interpretation.

Velocity ratio (Vp/Vs): A tool for fluid and lithology discrimination

During this study we noticed a remarkable fluid and lithology discrimination characteristics using relations between the velocity ratio and other parameters such as porosity and impedance. Here we present the relation with porosity while its relation with impedance is presented in section 4.4, after a careful analysis of the rock physics depth trends.

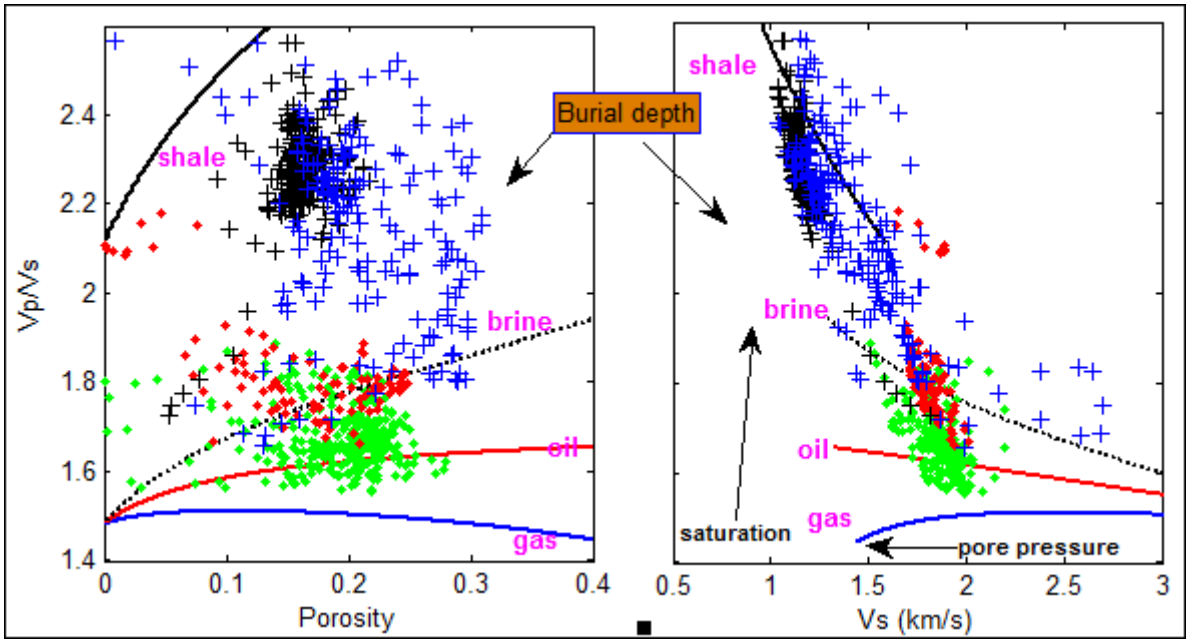

Figure 41: Vp/Vs ratio versus porosity (Left) and versus Vs (Right). Green points represent gas sands, red points represent oil sands, blue crosses represent shaly brine sands, and black crosses represent shales. All data are in situ from well-A. We see a good discrimination both in fluid and lithology. High shale content plots towards the shale line while sands plot at lower ratios depending on the fluid content of the rock. Thus gas sands plot at lowest ratios (due to low bulk modulus) and relatively highest Vs (due to low density) than oil and brine. The black-dotted, blue, and red lines represent constant cement lines of 2% for brine, gas, and oil respectively at 20MPa pressure and 70^{0}C while the upper solid line is the friable clay model at 18MPa pressure and 70^{0}C.

Figure 41 we see the separation of 'clouds'. The black cloud shows where the cap shale plots using in situ data from well-A within the Lista Formation (2054m-2099m). The green clouds represent the gas zone. The red cloud represents the oil zone. Blue crosses represent brine interval between 2210m-2240m. We see that within the sandstone interval, the various fluids are noticeably separated, with gas sands plotting at lowest ratios and brine sands at relatively higher ratios. As one looks at the figure it may look puzzling to describe the whole sandstone trend especially where we observe more scattering. What is responsible for these scattering effects? Why is there a separation between the clouds? Do the trends indicate some geological variability, for instance, depositional and diagenetic trends?

In this section we try to answer these questions and to explain some of the factors that may be responsible for the observe trends. We would focus on the fluid and lithology effects and later on, use the acoustic impedance versus velocity ratio to include other factors.

1. The solid rock

In clastic rocks, such as our reservoir sandstones, we can roughly estimate the Vp/Vs ratio from the clay content. As the lithology changes from shale to sand, the Vp/Vs ratio drops drastically. One probable reason why the sandstones plot at lower ratios, one may say, is because sands have a higher quartz content (which has a Vp/Vs value of about 1.48) than clay which has a higher value. This preceding statement infers that one possible reason to the separation of the two clouds is due to lithology type (mineral composition). This

inference is justified when we found out that shaly regions within the reservoir sandstones containing the same fluid, plotted at higher Vp/Vs ratios than for cleaner sands.

Secondly, in clastic rocks such as sandstones, increase in clay content will decrease sorting and hence porosity. This would mean that the clays in our sandstone reservoir would plot relatively at lower porosity and higher Vp/Vs ratio, thereby causing some scattering effect.

2. ***Fluid effects***

The effect of fluids could be a major reason of separation of the data points. As porosity increases, the available fluids fill up the pores thereby causing a slight increase in the rock frame. The 'stiffest' fluid would have greater effect on the rock frame than the 'softest' fluid. This would result in lower Vp/Vs ratios for the 'soft' fluid and higher ratios for the 'stiff' fluid since the shear modulus remains approximately unchanged. We see from the figure that gas sands plot at lowest ratios while brine sands plot at higher ratios than oil and gas sands.

However, diagenetic processes such as compaction and cementation would remarkably inhibit this discrimination of the fluids. Looking at both sides of the figure, by interpolation we see that increase diagenesis reduces the pore pressure and porosity is approaching zero. The models show very poor fluid discrimination at high diagenetic processes.

3. ***The dry or wet cracks***

The third factor that can influence Vp/Vs ratio values is the presence or absence of cracks. The presence of cracks would increase porosity in the rocks. If the cracks are dry, there would be a negative influence on the Vp/Vs ratio. But if the cracks are wet, for instance, filled with water, the rock tends to be relatively stiff and would show an increase in Vp/Vs ratio.

Our conclusion is that both lithology and fluids have an effect on Vp/Vs ratio as follows;

a. For the same lithology, the presence of fluids would be the determining factor, for instance, sandstones with gas will plot at much lower Poisson's ratios while water-saturated sands will plot at relatively high Poisson's ratios.
b. For different lithologies of the same fluid, the shalier lithology will plot at relatively higher Poisson's ratio than the sandier lithology.

4.7. Rock Physics Depth Trends

Avseth et al., 2008 have demonstrated that characterization of sandstone reservoirs embedded in shale would be enhanced with better understanding of the physical properties of shale and how rock properties of sandstones are affected by compaction with respect to burial depth. Both the shale and sandstones in this study have shown some evidence of depositional and diagenetic trends. We try to diagnose how the various rock physics

parameters vary with depth and how the deviation from normal trends is influenced by geologic factors.

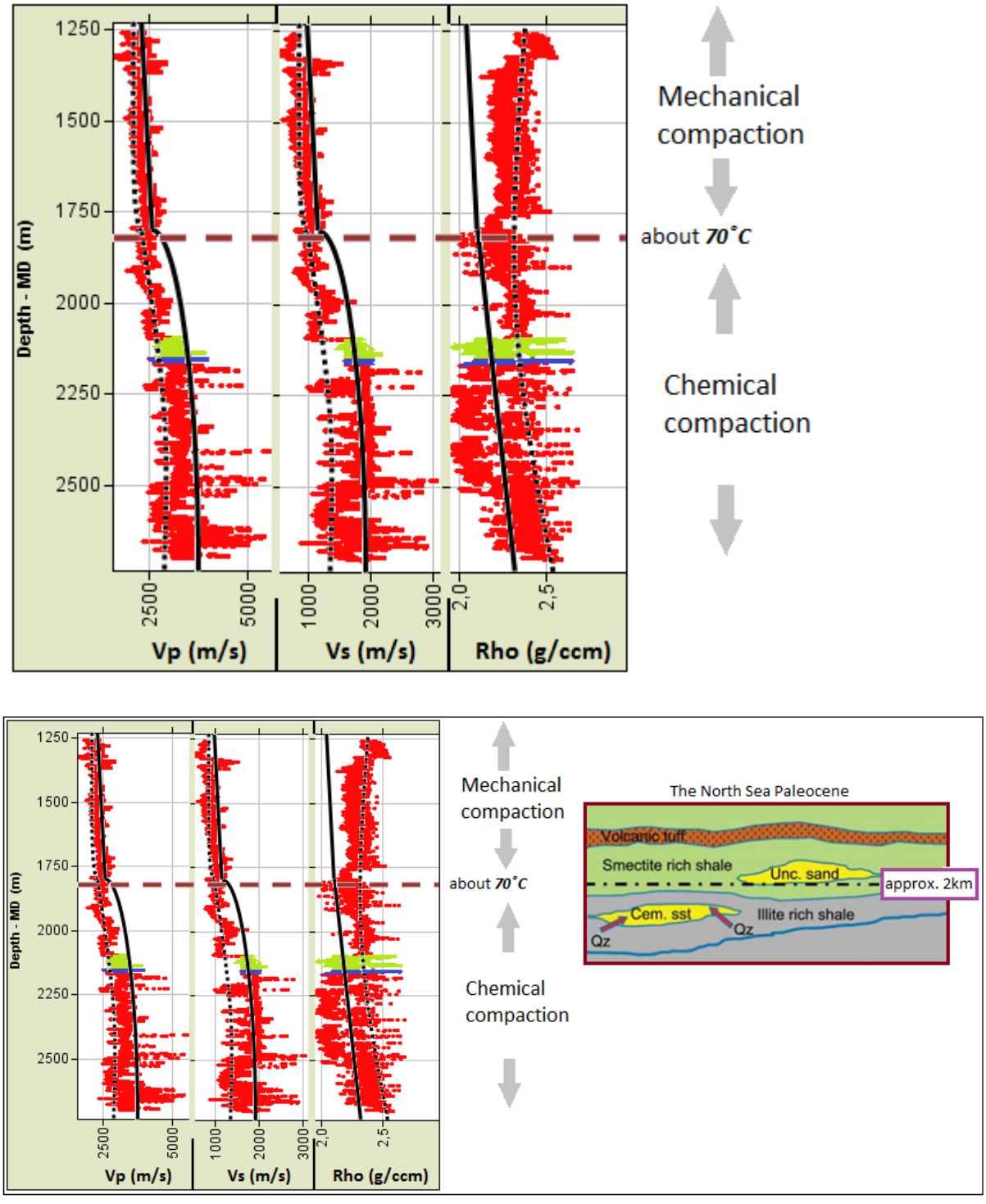

Figure 42: Possible rock physics depth trend for shale (black square-dotted line) and sandstones (black line) superimposed on whole logged data from well-A of. Green interval on the plot is gas zone while indigo interval is oil zone. The brine zone has not been indicated but there is an oil water contact down at the end of the indigo colour. (Adapted from Avseth et al., 2009).

4.7.1. Depth trends for sands.

Figure 42 is an excerpt from Avseth et al., 2008 that has been adapted to this study. The density depth trend on the figure for sand shows an almost steady increase in density with depth as we move from mechanical compaction to chemical compaction. This could be the effect of cementation at higher depths which increases both density and rock stiffness. The effect of cementation would however, be more on the rock frame than the density. Deviation from this trend could indicate increase in pore-pressure which increases pore-fluid densities. The most effect of this pore-pressure increases from brine, through oil and to gas (Avseth et al., 2005). We see from figure 42 that the reservoir sandstones fall more to the right of the density depth trend, indicating the presence of the fluids. However, conclusions about the presence of fluids in the sandstones cannot be solely based on this observation but rather helpful as we make other analysis with the several technologies of interpretation. Our data at shallower depths with respect to the density trends also confirm that we have almost no sands. Had there been sands at the shallower depths, the density values would have moved to the left closer to the density depth trend for sand as observed within the sandstone reservoir.

On the other hand, the velocity depth trends for sand shows a rather almost abrupt increase beginning from the chemical compaction zone. This indicates how sensitive the elastic stiffness could be to the presence of even small amount of cement. We see from the figure that the depth trends show higher velocities for sands than shale at all depths. Following the concept of geothermal gradient, temperatures and pressures at reservoir depth have been assumed to be about 70 degree Celsius and about 20MPa respectively where we begin delving into the zone of chemical compaction. Cements could be of various types such as quartz cement, calcite cement, feldspar cement etc. In our reservoir, stringers of calcite have been found and so we assume that the small cement found is of calcite type. Deviation from the above depth trend for sands would depend on the various shale compositions within the different sands. Deviation could also be caused by the presence of fluids within the sands; an effect which would only be noticeable on the P-wave velocity log as fluids have an approximately zero shear modulus.

4.7.2. Depth trends for shale.

The density depth trend for shale shows a very gradual increase as we move from mechanical compaction to chemical compaction. We see clearly from the figure that the density values for shale are higher than that of sands at all depth point. We also see that the supposedly shaly areas within the sandstone reservoir correlate with this trend. Unlike the trends for sands which have been accounted for by presence of possible cements at greater depths, shale is usually not associated with cementation. This suggests that some other factor than cementation is accountable for this depth trend shown by the shale density. But just what exactly could be the reason behind the observed higher velocities and densities with depth in the shale? Several scientists have attempted an explanation to this. For instance, Bjørlykke, 1998, has shown that at 2km depth, there is transformation from

smectite to illite and so the shale present could be illite-rich. Keith Katahara, 2007, also attempted an answer to whether it is the overpressure unloading or smectite-illite transformation that is responsible for this trend. Even with these explanations, it still remains a puzzle to some authors, about which of the factors precisely should be favoured over the other.

Table 6: various clay minerals and their densities (Deer et al., 1966)

Clay mineral	Density range (g/ccm)
Smectite	2.0 – 2.6
Illite	2.6 – 2.9
Kaolinites	2.61 – 2.68
Chlorites	2.6 – 3.3
Muscovites	2.77 – 2.88

Table 6 shows various clay minerals. Smectite has a lower density range compared to that of illite. At shallower depths, it is probable that we have mainly smectite-rich shale which become transformed into denser illite-rich shale at greater depths and so account for the depth trend shown by the shale curve.

Up to about depths close to 2km from the sea floor, mechanical compaction is the dominant process controlling diagenesis. The sediments here are unconsolidated and most likely do not exhibit any cement material which is resulting to relatively very low velocities. If we had some sands also in this mechanical compaction zone, we would expect to see a slightly higher velocity since quartz have higher velocities than shale. Although the sandstone reservoir contains only a small amount of cement, we still notice that it falls in line with the depth trend for chemical compaction as modelled with a great increase in the velocities. This means that had there been more cement in our sands, we would have observed greater velocities. At about 2km where temperatures get to approximately 70^0C, cementation occurs. This thesis work however, is not focused on these details and so more on this will not be mentioned.

4.8. Impedance characteristic

Impedance has been a fundamental part of interpretation and has been used to image layers. This has given it an edge over the conventional seismic interpretation which rather images interfaces. Based on this advantage of impedance, we are able to interpret lithology in order to understand the rock properties of our area of interest. This section presents acoustic impedance versus velocity ratio, Vp/Vs, as a rock physics template and has been used to indicate fluids (gas, oil, and brine) and lithology related to our reservoir of interest mainly sand and shale, and transitions between them, that is, sandy shale and shaly sands.

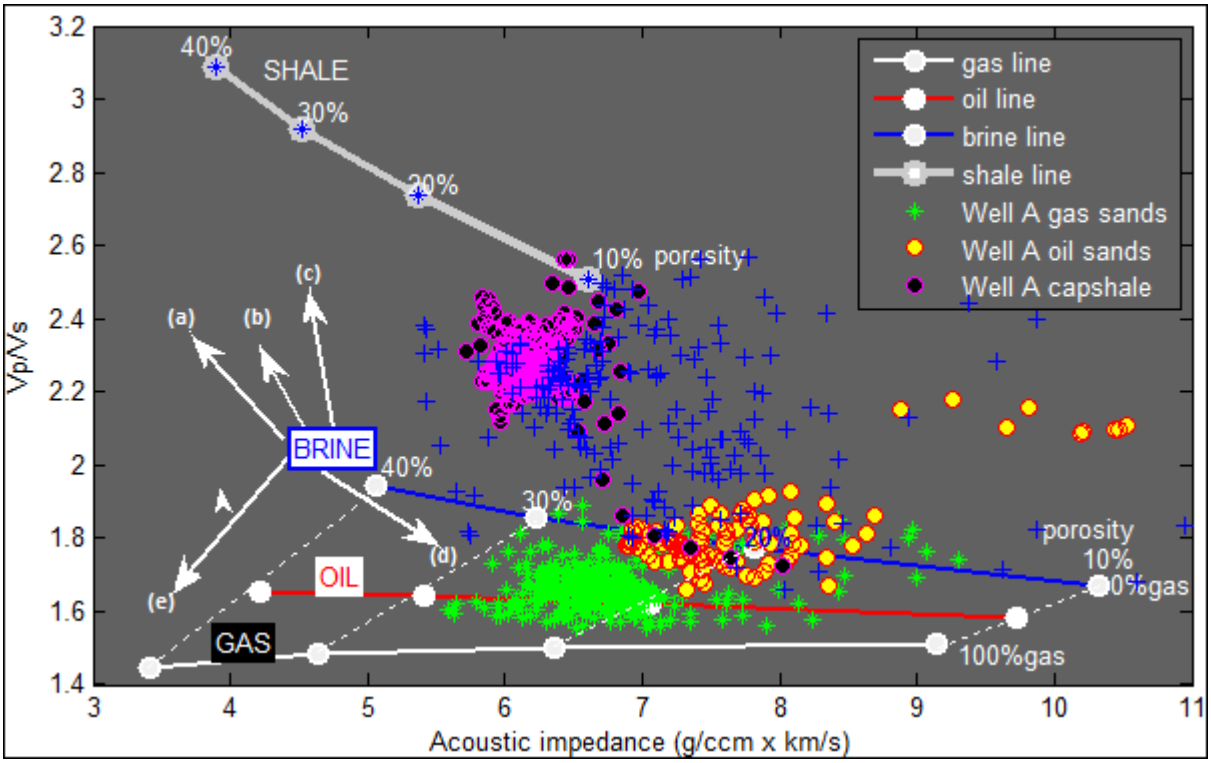

Figure 43: A rock physics template using a cross-plot of acoustic impedance versus velocity ratio (Vp/Vs) of well-A of the Alvheim field. The template includes gas sands (green crosses), oil sands (yellow/red balls), and cap-shale (magenta/black balls). The blue crosses represent the water zone below the reservoir sandstones between 2210m-2240m depth. The sand lines; white (gas), red (oil), and blue (brine), are modelled at 70^{0}C and 20MPa pressure while the friable shale line (grey) is modelled at 50^{0}C, 18MPa pressure. All data are in situ.

Figure 43 employs the rock physics template of acoustic impedance versus Vp/Vs that was first presented by Ødegaard and Avseth (2003). It is a combination of diagenetic and depositional trend models that we have described in the previous sections for the prediction of various lithologies and fluids within the subsurface. We have used in situ data from well-A. The magenta/black balls represent the shale cap-rock within the Lista Formation (2054m – 2099m and upper grey line represents the friable shale line (we assumed 100% clay saturated). The green crosses are the gas sands at depth 2099m – 2152m while the yellow/red balls represent the oil sands at depth between 2153m – 2168m. The blue crosses represent water zone below the reservoir between 2210m – 2240m. The brine (blue) and oil (red) saturated constant cement lines are 2% cemented while the gas (white) saturated line is uncemented. Factors that have been taken into consideration include; lithology, mineralogy, diagenesis, burial depth, pressure and temperature. The pressure and temperature for the reservoir sands were assumed 20MPa and 70^{0}C while those for the shale cap-rock were assumed 18MPa and 50^{0}C respectively. The reason for this for this difference in pressure and temperature for the two lithologies is that, we assumed pressure and temperatures increase with depth of which, if not taken into consideration, could lead to potential pitfalls during our interpretation. The figure shows the following trends;

a. Increasing porosity
b. Decreasing effective pressure

c. Increasing shaliness
d. Increasing cementation
e. Increasing gas saturation

The trend for increasing cementation represents trend for increasing burial depth and compaction. It is important to consider the mineralogical changes with the depth trends discussed previously in section 4.7 such as, smectite being transformed into illite. There are also changes associated with sand minerals but for this study, we have considered sands of pure quartz and have used only properties related to quartz. The figure shows that at lower depths, shale has higher Vp/Vs ratios which decreases at greater depths while the hydrocarbon sands ('soft') show very low ratios at lower depth and increase with depth. If we interpolate the rock physics models to higher impedances, we would have a sand-shale cross-over.

We see on the above RPT that our reservoir sands fall within a porosity range of about 10% - 30% as we saw in the porosity cross-plots. We would expect clean sand saturated with the hydrocarbons to plot further down where we have 100% gas at very low velocity ratios. But we see the effect of the shale as some reservoir sands plot slightly to the north. As we observed on our well logs, at the OWC we saw that acoustic impedance, Vp, and Vp/Vs increased significantly. The oil sand data points (yellow) plotting at very high acoustic impedance, high Vp/Vs and 0% shale porosity could represent this contact. If this is true, then the RPT technology might as well be developed to interpret possible fluid contacts. Another possibility is that, this could be the effect of noise.

RPT's are basin specific (Avseth et al., 2005), and vary from one basin to another as with various depth trends. It is therefore important to understand these trends for a given area under investigation before interpreting. The impedance RPT can serve as a guide to the seismic interpreter who would need to understand the various lithologies likely to be encountered in the subsurface and not to rely only on information about boundaries.

4.8.1. Implications on Fluid Detectability and AVO Signatures

AVO signatures are depth dependent. Following the depth trends, deeply buried hydrocarbon sands will plot at high impedances on acoustic impedance versus Vp/Vs ratio rock physics template and on AVO cross-plots such as reflectivity versus angle. The Vp/Vs ratios will depend on the fluid content of the sands. As earlier mentioned, P-wave velocity is sensitive to fluids while S-wave velocity is approximately not sensitive to fluids. By inference, we would expect gas sands to have low acoustic impedance and Vp/Vs resulting to negative zero offset reflectivity and negative AVO gradient. With increase cementation and burial depth, the porosity is reduced and both velocities increase (so velocity ratio may stay low) but the acoustic impedance increases (since acoustic impedance depends on velocity and density). This would result to relatively positive zero-offset reflectivity and

negative AVO gradient. Without understanding the depth trends of the rock physics parameters within a specific basin of interest could be a major pitfall in interpretation. Such pitfalls may include;

1. A wrong model (e.g. friable sand model) being used on data that involves some cementation (constant cement model is right) due to lack of detail knowledge of the area of interest. These cemented or slightly cemented sandstones could plot on an area where we expect oil sands, leading to misinterpretation.
2. Sandstones of low gas saturation would plot at higher velocity ratios and could be misinterpreted as oil sands even if we use the right model with good data.

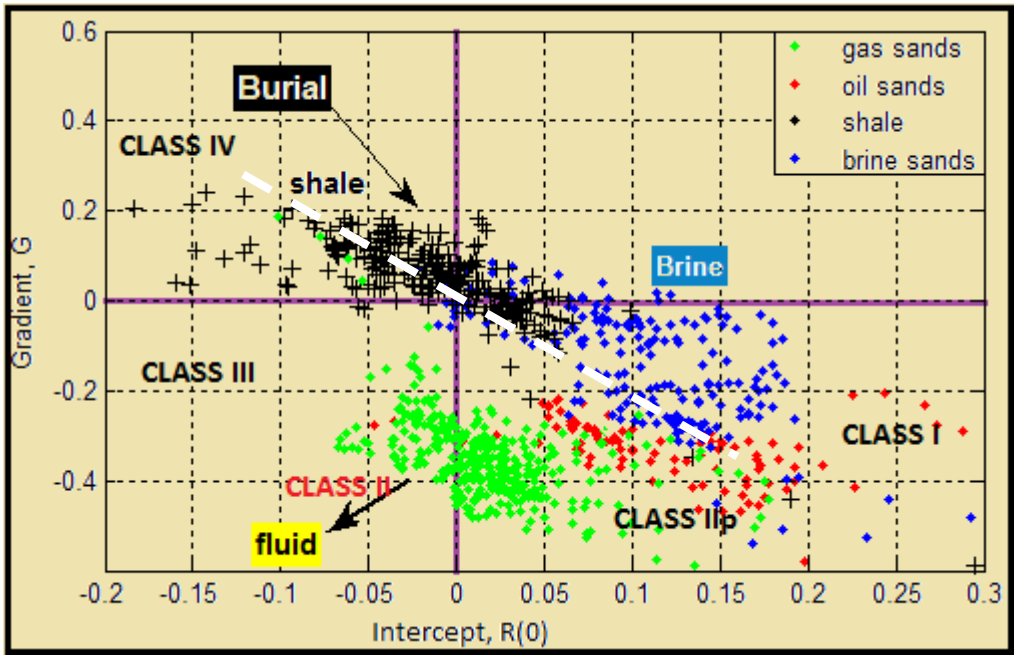

Figure 44: Gradient, G versus intercept, R(0) of well-A lithologies to observe the effects of the geologic trends on AVO signatures. The lithologies are; brine sands (blue), oil sands (red), gas sands (green), and cap-rock shale (black crosses). The classes are show are characterised as; Class I: hard rock, high impedance, low Vp/Vs ratio relative to cap-shale. Class II: weak but negative R(0) and G.Class IIp: weak but positive R(0) and negative G. Class III: soft sands with hydrocarbon. These are associated with bright spots. Class IV: cap-rock shale.

Figure 44 is an AVO cross-plot of gradient versus intercept from well-A. The sands are represented as green (gas), red (oil), and blue (brine). We plotted the various lithology putting shale of the Lista Formation (layer 1, from 2054m – 2099m) on each of them (i.e., layer 2 using the fluid intervals) as described in equations 3.12 and 3.13. Black data points represent the cap-shale derived by putting shale mostly from the Sele Formation (2009m – 2054m) on the Lista Formation cap-rock shale. We see the possibility of cementation having an effect on the direction of the hydrocarbons. From the description of the various classes, we would expect an AVO anomaly to plot in the 1st quadrant (Class II). But we see clearly that the hydrocarbons have almost completely 'drifted' into the 4th quadrant. It seems to us that this is most likely the effect of the few amount of cementation observed during cross-plot analysis in section 4.4, and as observed on the main RPT in figure 43.

Our conclusion is that, ‘masterminding’ the depth trends of a particular basic is fundamental to good interpretations in hydrocarbon exploration. Failure to this may lead to costly decision-making and interpretations. Proper investigations should be carried out on the degree to which the zone of interest could be cemented as it only takes about 1% or 2% for significant effects.

5. COMPARISON OF WELLS

In this section we take a look at two other wells; well 25/4-7 (a neighbouring well to well-A) and well 35/11-10 (found in the Fram field) in comparison to our main well (well-A). We would denote the two wells as ***well-B*** (well 25/4-7) and ***well-C*** (well 35/11-10).We investigate the properties of the cap-rock shales and reservoir sands in each of the wells and present a postulate, based on observations and analysis of the elastic and acoustic properties using cross-plots. The objective is to understand the mineralogic variations of the cap-rock shales (which may cause internal seismic signatures, Avseth et al., 2005) within the same type of formation but located in different geographic regions using rock physics models. We want to understand how to differentiate these shales from other lithologies especially reservoir sandstones.

First, we compare the cap-rock shales from each of the wells (well-B and well-C) encountered in the Lista Formation with the cap-rock shales of the main well-A. Next, we attempt an explanation for their differences and similarities in terms of elastic and seismic responses using cross-plots with superimposed appropriate (by our judgement) rock physics models derived from the equations in section 2.3 and the Gassmann's relations in section 3.2. Then, we try to interpret possible geologic trends such as sorting, porosity, and compaction and finally, we suggest how one may distinguish these shales from sandstone reservoirs based on our analysis and observations.

To acquire this, we present the following algorithm:

- Using the modified Hashmin-Shtrikman lower bound, we model the cap-rock shales assuming a critical porosity of 0.6 which is higher than the critical porosity we used for sandstones (because clay is usually deposited with a higher porosity than quartz due to the inherent porosity of the clay material).
- We derive effective bulk and shear moduli models (and velocity models) for sandy shales by adding fractions of quartz to clay. For increasing quartz fraction we reduce the critical porosity by estimation depending on the given silt fraction.
- We superimpose the rock physics models on in situ data from wells using cross-plots to estimate the moduli and velocities that would be needed to match the sandstone and shale data.
- We attempt an estimate about the mineralogical composition of the sandstone and shales and also the possible geologic trends.

5.1.The Kneler Well 25/4-7

Petrophysical analysis I

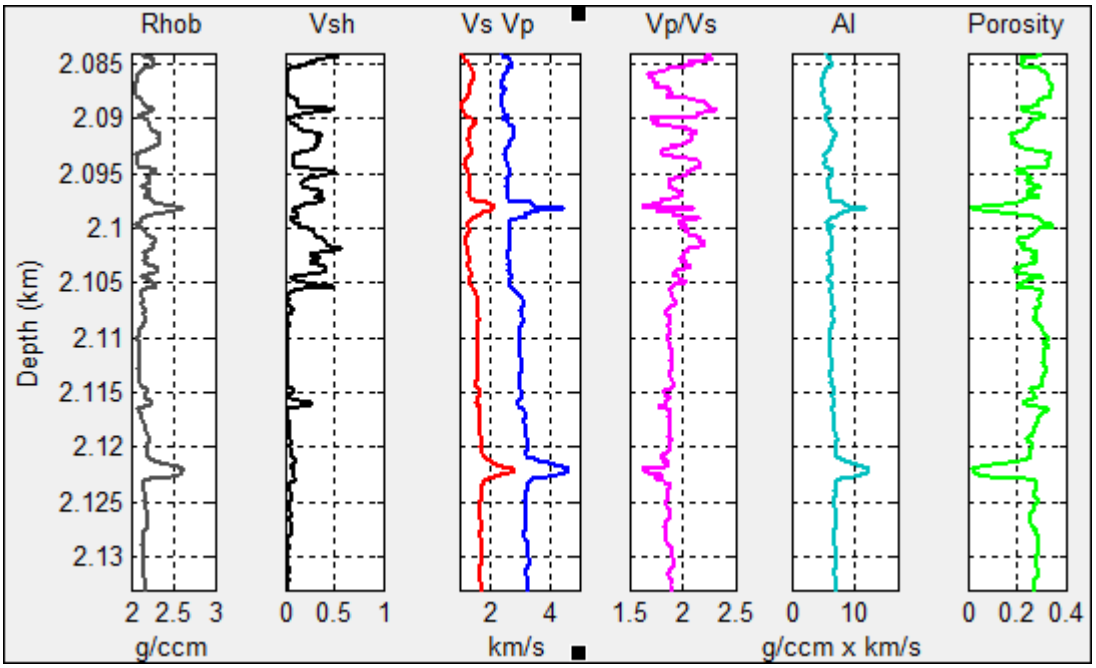

Figure 45: Logs from well-B. The well contains oil and the target zone interval is between 2084.5m to 2132.5m. We have an OWC at 2132.5m. Looking at the volume of shales log, the upper part of the reservoir (about 2084.5m – 2105m) seems to be shaly while the lower part seems to be mainly sandstone. Most of the portions within this shaly interval are showing relatively higher densities than the lower portions since clay is denser than quartz. The velocity land acoustic impedance logs seem to follow almost the same pattern and from a general perspective we do not notice any fluid contacts as was the case in well-A. Within the sandstones at about 2122m, there is a very sharp drop in Vp/Vs and increases in velocities, density, acoustic impedance, and a drop in porosity. This means Vs has increased over Vp and associated with such porosity and density responses, may indicate a diagenetic effect such as the presence of cement. We recall that it only takes about a percent or two of cement to cause significant effects on seismic velocities.

Lista Formation cap-rocks I

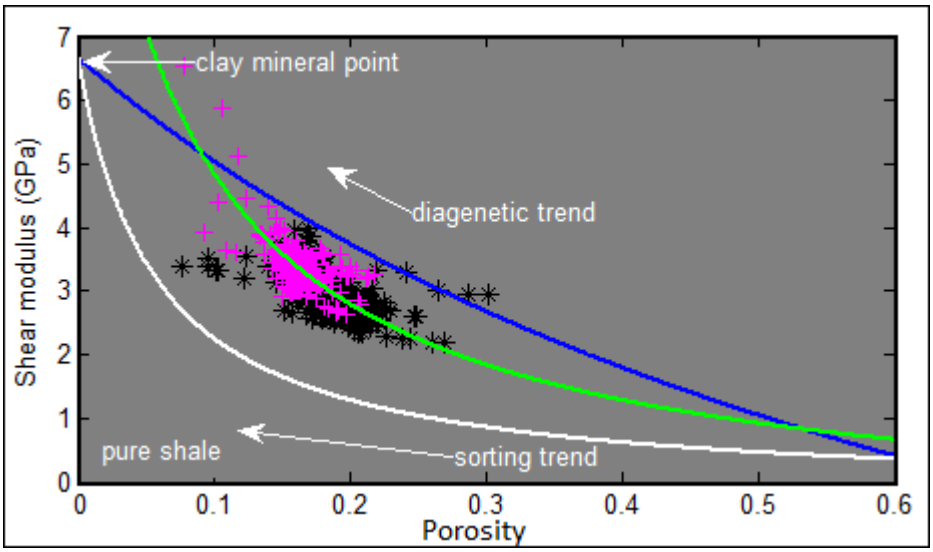

Figure 46: Comparison between cap-rock shales for well-A (magenta colour) and well-B (black crosses) on the shear modulus versus porosity plane with superimposed rock physics models for clean shales (white line; modified Hashmin – Shtrikman lower bound) and sandy shales of 25% silt (green line). The upper blue line is the modified Hashmin – Shtrikman upper bound, HS^+, for clean shales. The models for clean shales were computed at initial porosity of 60% while sandy shales model was computed at initial porosity of 50% because we assumed the sand would reduce the initial porosity of the rock. Notice that the green line (25% quartz) fits nicely on both well-A cap-rock shales and well-B cap-rock shales. The rock physics models show us that these shales have very similar mineral composition of 25% silt but have different degrees of compaction. The diagenetic trend shown by the HS^+ bound (blue) indicates that well-A cap-rock shales have been subjected to a relatively higher compaction than well-B cap-rock shales and this has reduced its porosity to lower values than well-B.

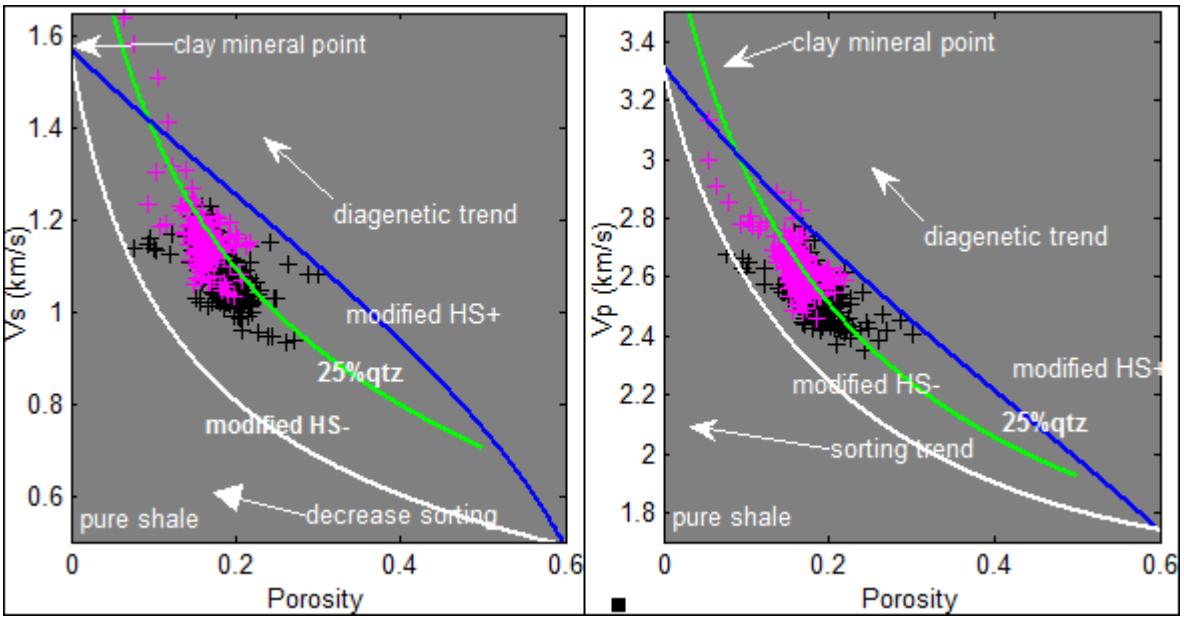

Figure 47: Comparison between cap-rock shales for well-A (magenta colour) and well-B (black crosses) on the velocity versus porosity plane with superimposed rock physics models for clean shales (modified Hashmin – Shtrikman bounds) and sandy shales of 25% silt (green line). The upper blue line is the modified Hashmin – Shtrikman upper bound, HS^+, for clean shales while the white line is the friable clay model. The models for

clean shales were computed at initial porosity of 60% while sandy shales model was computed at initial porosity of 50%. Once again we notice the good fit of 25% silt on both plots with a better fit on Vp. A possible reason for the difference is that at shallower depths, low Vs values may have been picked. We conclude from this that 25% silt fraction may be more representative of the cap-rock shales. The diagenetic trend shown by the HS $^{+}$ bound still reveals that well-B cap-rock shales are located at shallower depth than well-A cap-rock. They have probably been subjected to lesser compaction.

Heimdal reservoir sandstones I

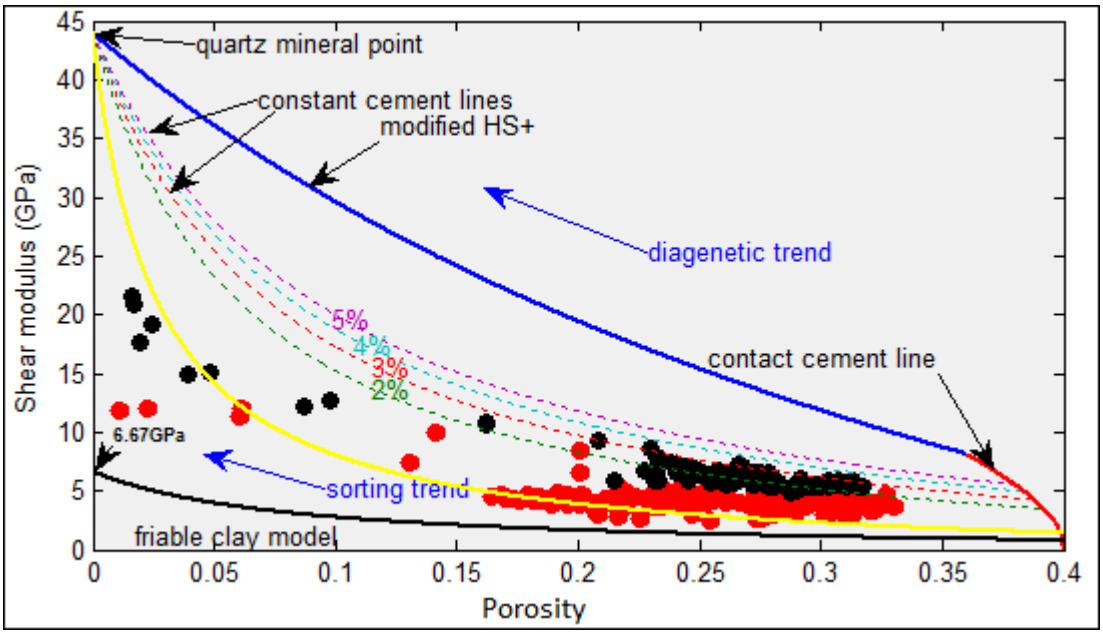

Figure 48: Shear modulus versus porosity at pay-zone in well-B using in situ data. The dash lines are the constant cement lines. The modified Hashmin – Shtrikman lower bound for unconsolidated sandstone is represented by the yellow line after application of the slip factor. High porosity end members of the cement lines were computed from the contact theory model (bold red line). Black data points are oil sands from 2084.6m to 2105.5m while the red data points are oil sands from 2084.7m to 2132.5m. The former are more massive and fall nicely on the constant cement line of 2% while the latter have been described as herolithic (NPD) and we notice that they plot closer to the HS lower bound.

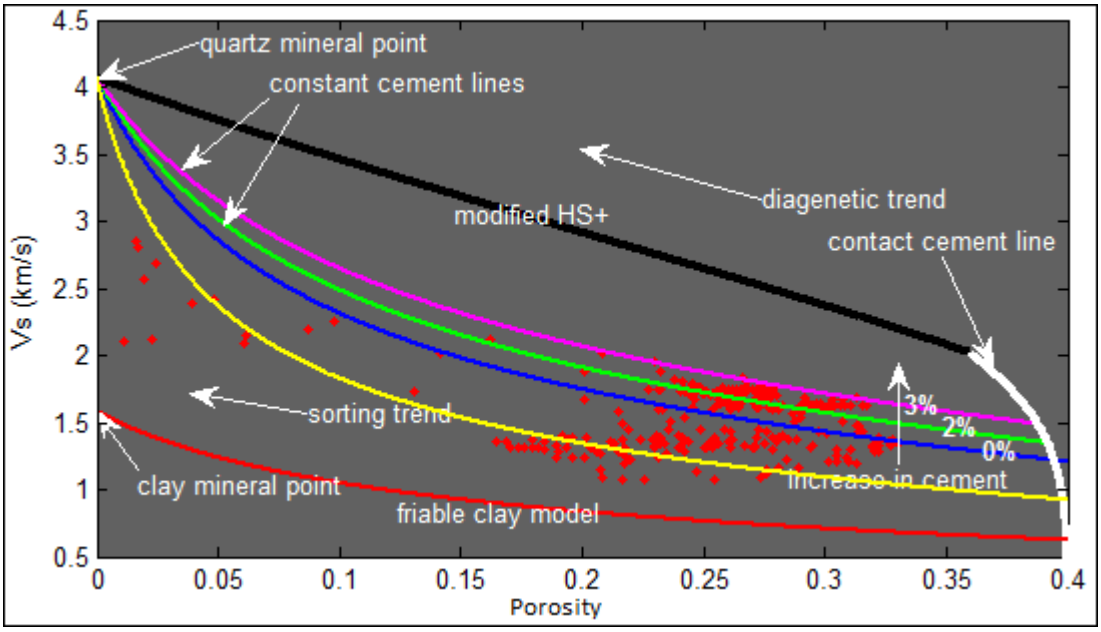

Figure 49: Vs versus porosity at pay zone in well-B using in situ data. Magenta, green, and blue lines represent constant cement lines with 3%, 2%, and 0% respectively. The black line is the HM plus modified HS^{+} bound for unconsolidated sandstone while the white line is the contact cement model from which the high porosity end-members of the constant lines are computed. The yellow line represents the HM plus modified HS lower bound for unconsolidated sanstones after slip correction. The red line represents the friable clay line. One interval shows some cementation of the sandstones of about 2% (similar to well-A) while another interval shows unconsolidated sandstones. Temperature and pressure for the cement lines are 70 ^{0}C and 20MPa respectively and those for the friable shales are 50 ^{0}C and 18MPa respectively.

Impedance characteristic I

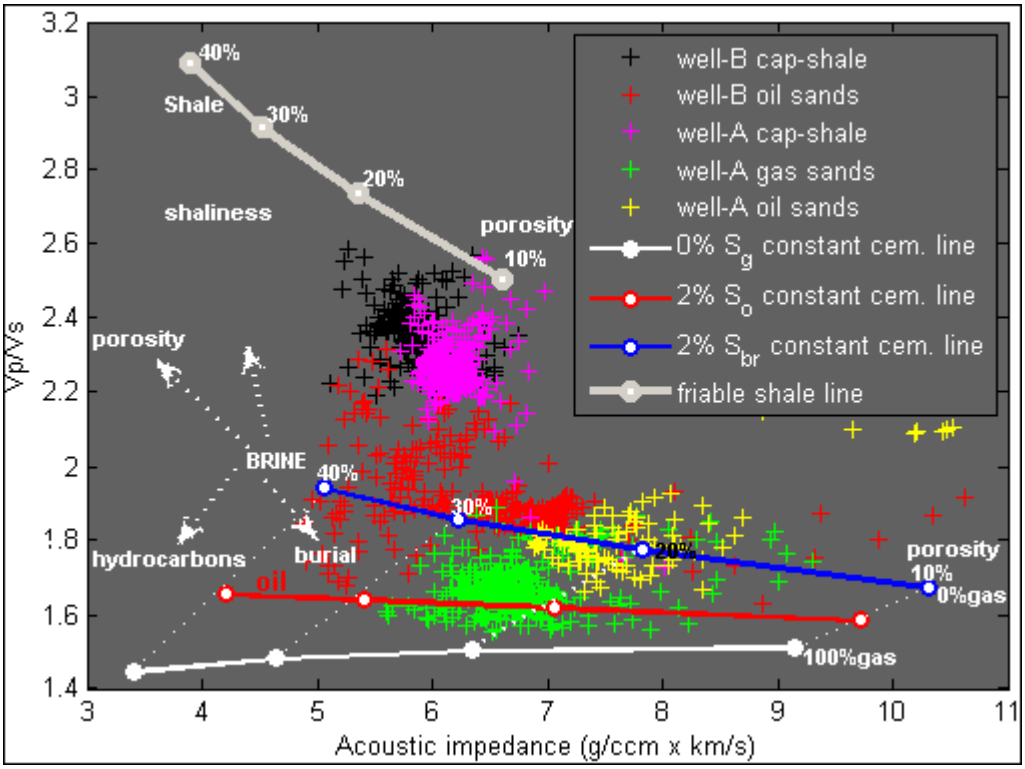

Figure 50: comparison between well-A and well-B on a rock physics template of acoustic impedance versus Vp/Vs using in situ data. The constant cement lines for brine saturation (blue) and oil saturation (red) are 2% cemented while that of gas saturation (white) is cement-free. The grey line at the top of the figure represents the friable shale line. All the lines are the identical to the AI vs. Vp/Vs RPT in section 4.8. We notice that well-A shales (magenta crosses) plot at relatively lower porosity and greater depth than well-B shales due to compaction as we earlier suggested. They also contain a greater fraction of quartz (probably) than well-B shales as they slightly trend towards the sands. The figure also confirms the higher porosities of the oil sands in well-B compared to the oil and gas sands in well-A. Notice the separation of two zones shown by well-B sands. On one hand, there is a seemingly friable zone at lower depth that is relatively not affected by cement and on the other hand, we see a more cemented zone at greater depth. We observe that the more buried well-B sands may contain about similar cement volume with the gas sands but shows higher ratios.

From figure 50, we see that without understanding some of these trends and possible mineralogic differences, wrong models can be applied on the area of study of which a misleading interpretation would arise. Such differences include; clay and silt contents, water saturations, cement volume, porosity, and burial depth. During this study, we found it challenging to figure out the most appropriate porosity to employ when modelling porosity cross-plots for the cap-rock shales. By using such an RPT, it makes it easier to account for the shale characteristics with respect to the geologic trends.

5.2.The Fram Well 35/11-10

Petrophysical analysis II

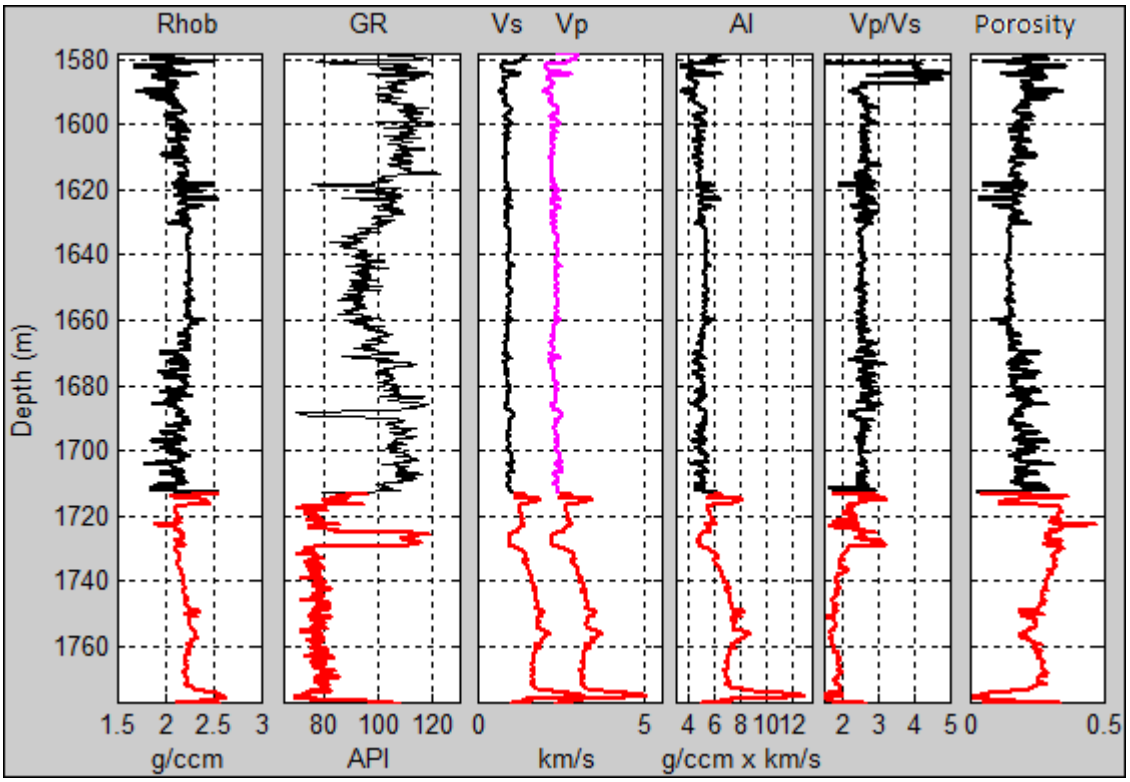

Figure 51: Well logs of well-C within the Lista formation (1578m-1713) and Heimdal formation (1713m-1777m). Shear wave velocity was predicted using Greenberg-Castagna empirical relations for sandstones and shales within their respective lithologies. The red plot below represents the Heimdal formation interval which is water saturated. Porosity is computed from bulk density and shows an increase from the Lista Formation into the Heimdal sandstone. We notice from the gamma ray that the Lista Formation is dominated by shales (assuming the gamma ray is indicative of clay content) while the Heimdal formation is dominated by sandstone with very high gamma ray reading from about 1725m-1730m (a similar characteristic in well-A).

Lista Formation cap-rocks II

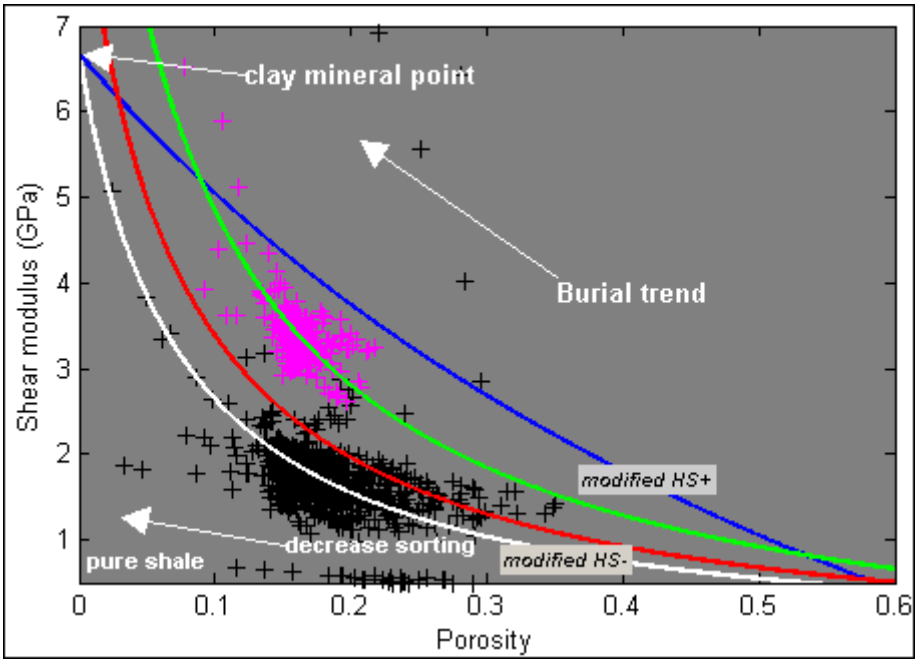

Figure 52: Comparison between cap-rock shales for well-A (magenta crosses) and well-C (black crosses) on the shear versus porosity plane with superimposed rock physics models for clean shales on in situ data (white line; friable shale line) , sandy shales of 25% silt (green line) and sandy shales of 15% silt (red line). The upper blue line is the modified Hashmin – Shtrikman upper bound + Hertz-Mindlin theory, HS^{+}, for clean shales. The models for clean shales were computed at initial porosity of 60% while models for sandy shales were computed at initial porosity of 55% and 50% for silt fractions of 15% and 25% respectively. Respective temperatures and pressures were estimated at 70 ^{o}C and 18MPa for well-A, and 50 ^{o}C and 15MPa for well-C. Well-A cap-rock shales fits well on the 25% quartz content of the shales lines while the well-C cap-rock shales fits on the modified Hashmin – Shtrikman lower bound for clean shales. however, the fact that some of the well-C cap-rock shales plot above this lower bound close to the red line tells us these shales are only very clay-rich but not made up of entirely 100% clay. It is also clear as the models suggests, that well-A shales are more buried than well-C shales.

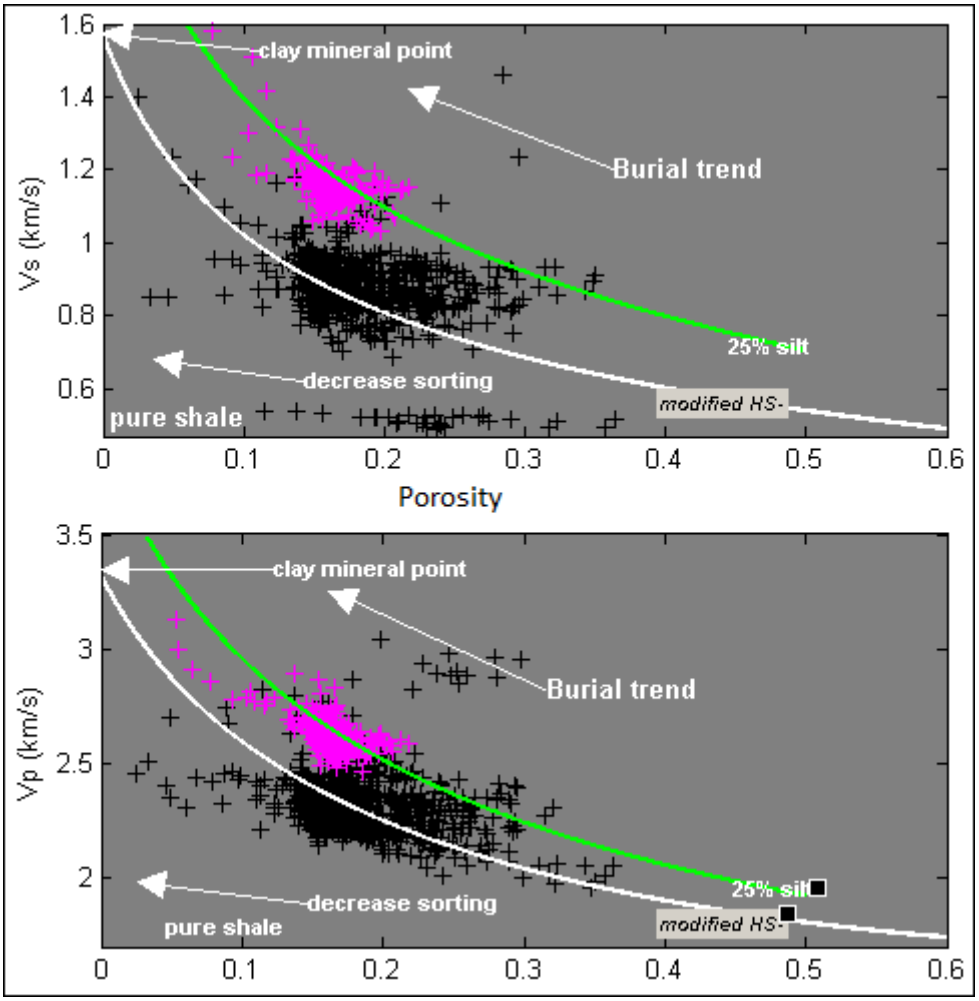

Figure 53: Comparison between cap-rock shales for well-A (magenta crosses) and well-C (black crosses) on the velocity versus porosity plane with superimposed rock physics models for clean shales. (white line; modified Hashmin – Shtrikman lower bound + Hertz – Mindlin theory) and sandy shales of 25% silt (green line). The models for clean shales were computed at initial porosity of 60% while model for sandy shales was computed at initial porosity of 55%. Temperatures and pressures were estimated at 70 ^{o}C and 18MPa for well-A, and 50 ^{o}C and 15MPa for well-C. Decreasing sorting (and porosity) in well-C shales seems to show little variation in the velocity while the well-A shales, the change seems to be a little bit more with decrease sorting (and porosity). We think well-C cap-rock shales are probably more silty.

Our interpretation of the Lista formations in well-A and well-C from figure 53, is that the cap-shales in well-A located at a greater depth, has probably been subjected to a higher degree of compaction than the cap-rock shales in well-C. Since clay minerals have intrinsic porosity and are water-bound in the mineral structure, the water is released as compaction increases and the mineral would be altered as well as the elastic properties of the shales that contain the minerals (as discussed in the depth trends in section 4.3). Such a process would lead to an increase in the bulk modulus and the rock loses more of its porosity which results to a velocity increase.

Although we are not very certain of the precise silt volume in well-A cap-rock shale (because we found it a bit challenging to model the sandy shales) the models however give us an idea of the difference between them. We suggest that cap-rock shales in well-A may contain

some amount of quartz more than well-C while the cap-rock shales in well-C seemingly are very clay-rich. This addition of quartz in well-A shales (reduced the clay content) tends to stiffen the rock.

As we saw from the depth trends, porosity reduction in very clay-rich shales subjected to compaction would show a very little variation in velocity (which we can observe on figure 53 by well-C shales). The reduction of sorting may be due to the lamination of the clay minerals. However, core sample analysis may show that this zone is not mainly made up of pure clay as rocks at subsurface depth, are seldom monominerallic.

A possible setback of our interpretation is that we may not have accurately estimated the initial porosity for these shales since the depositional porosity of shales is uncertain. Some very clay-rich shales may even exhibit depositional porosity of up to 80% (Avseth et al., 2005).

Heimdal Formation sandstones II

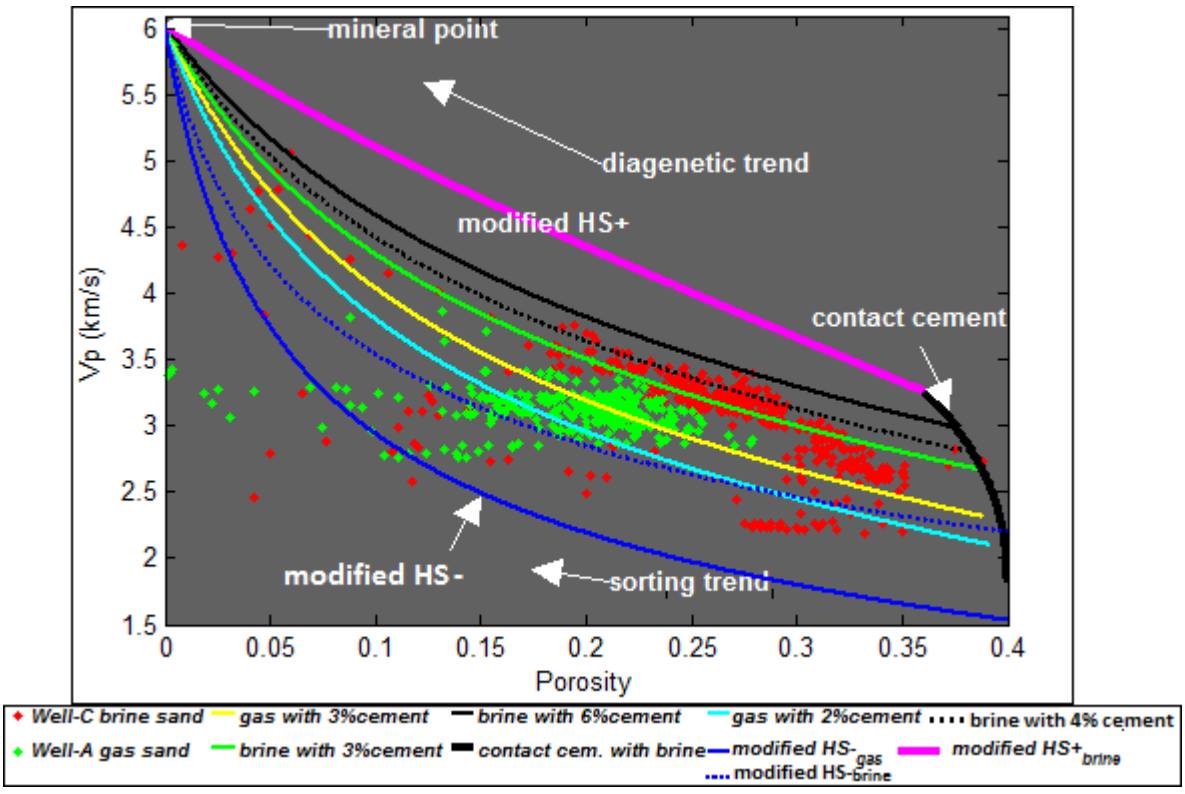

Figure 54: Vp versus porosity cross-plot comparing the Heimdal Formation sandstones in wells-A and C with rock physics models superimposed on in situ data. Respective temperatures and pressures were estimated at 70°C and 20MPa for well-A, and 60°C and 16MPa for well-C. We think that the lines that fit on the respective well data contain about the same amount of cement. i.e., well-A sandstones correlate approximately with the gas-saturated constant 3% cement line (yellow) and well-C sandstones better correlate approximately with the brine-saturated constant 3% cement line (green) than the 4% line (black-dotted line). The contact cement model (black line indicated by white arrow) is brine saturated. The Hertz – Mindlin plus modified Hashmin – Shtrikman upper bound is represented by magenta color while the modified lower bounds are represented by

the blue dotted line (water-saturated) and blue line (gas-saturated). The modified lower bounds are slip-factor corrected.

Figure 54 shows that most of the data from both wells contain some amount of cement in them as indicated by the constant cement lines.

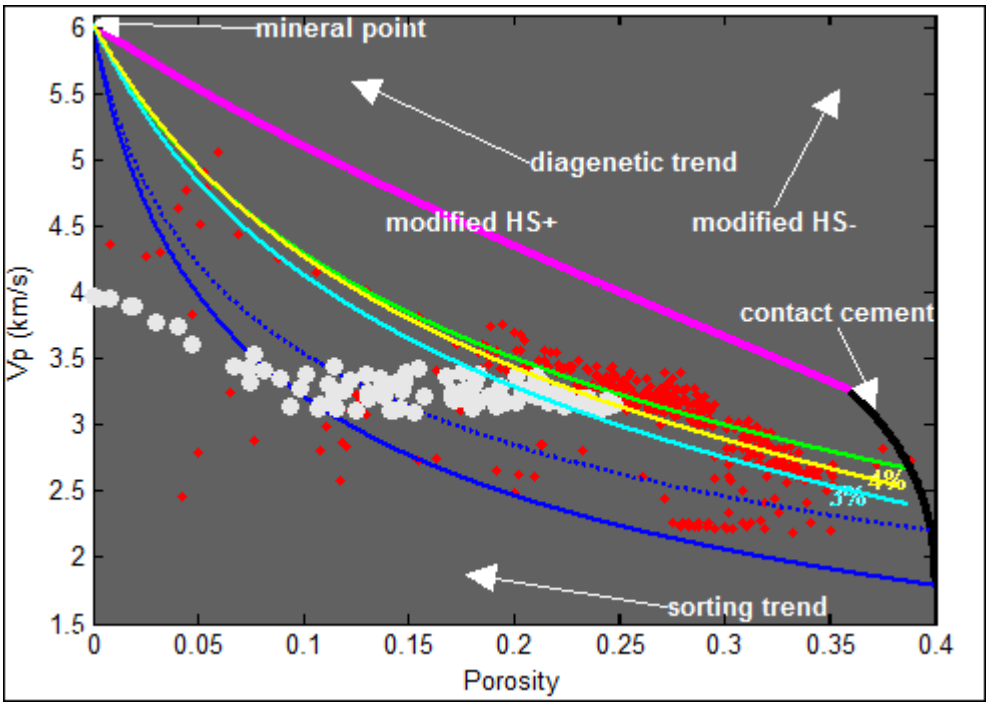

Figure 55: Vp versus porosity cross-plot comparing the Heimdal Formation oil sandstones in wells-A and brine sandstones in well-C with rock physics models superimposed on in situ data. Unlike the previous plot, the blue dotted line here represents the modified HS lower bound (+ HM with slip factor) while the cyan and yellow lines represent 3% and 4% constant cement lines saturated with oil respectively. The green line still represents 3% cement line and all other lines are identical to the previous figure. The grey data points represent the oil sands in well-A. There is a good match between the oil sands and the oil-saturated lines.

Impedance characteristic II

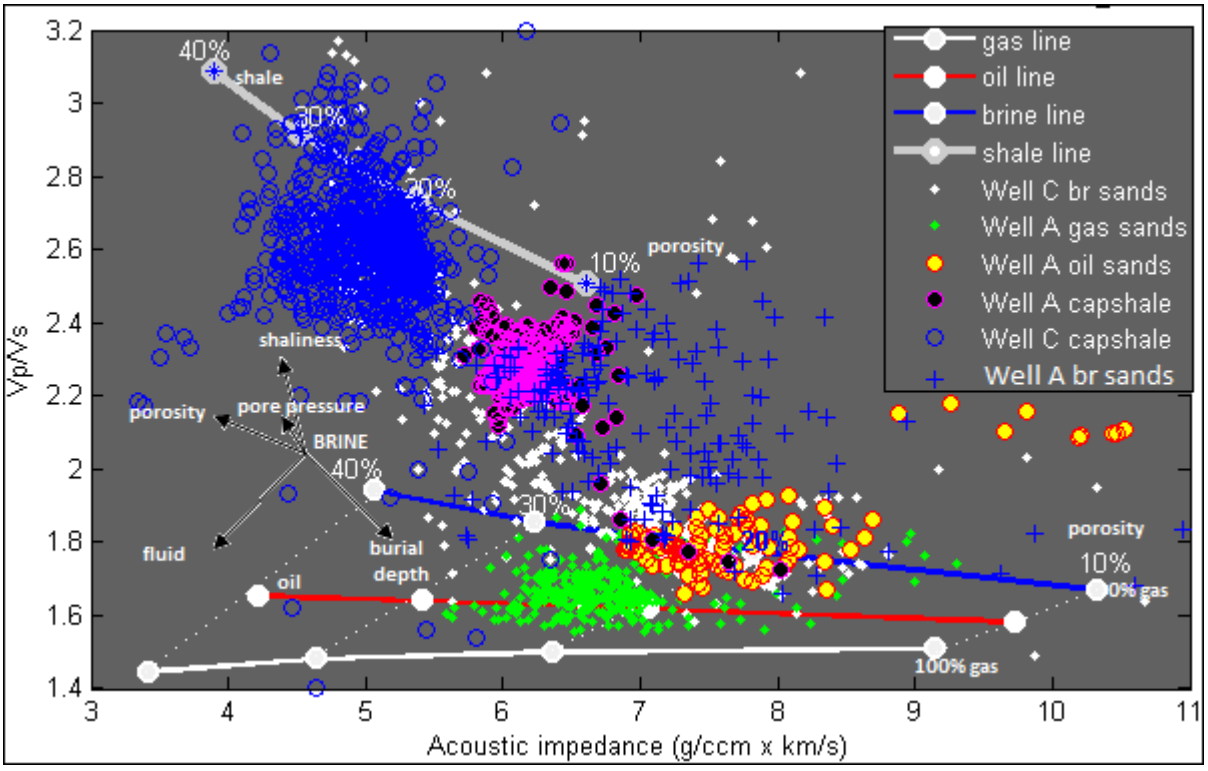

Figure 56: A rock physics template of an acoustic impedance versus velocity ratio (Vp/Vs) cross-plot with rock physics models superimposed on in situ data from of well-A and well-C. The template includes gas sands (green), oil sands (yellow and red balls), and cap-rock shales (magenta and black balls) from well-A. The blue crosses represent the water zone below the reservoir sandstones in well-A between 2210m-2240m depth. In situ data from well-C are; brine sands (white) and cap-rock shales (blue balls). Constant cement lines (2%) are saturated with brine (blue line), oil (red line), and gas (white line). Respective temperatures and pressures for sandstones were estimated at 70 ^{o}C and 20MPa while for the clean shales line (grey line), they were estimated at 50 ^{o}C and 15MPa respectively.

On figure 56 we notice that well-C brine sands fit better on the brine line than well-A brine sands and by inference, are located at shallower depth (and higher porosity) while well-A brine sands show more scattering effects than the former possibly due to a relatively higher clay content.

It is obvious from observation that the cap-rock shales in well-A are located at greater depth and lower porosity than the cap-rock shales in well-C .

CONCLUSIONS

From our study, we have been able to make some conclusions based on our observations. We would like to mention that, these may not be very accurate as they are not based on core sample analysis which would be more accurate.

- The well-log data for the wells in this study were good with those of the main well with more information than the other two wells. Neighbouring wells showed very similar characteristics in both the Heimdal and Lista Formations while they differed from the Fram well in that the Fram well seems to have undergone less compaction and mineralogical changes.
- Our rock physics study show that rock physics models are useful in diagnosing fluid and lithology as the interpretations tie with core analysis earlier carried out in the same area. For instance, the confirmation of a few cement in well-A from core samples collected at 2154m.
- It is important to properly investigate the target depth to be able to estimate the effective pressures at this depth interval. Failure to accomplish this would be a pitfall during analysis as model responses would not be representative of the area of study.
- From the use of the rock physics template of acoustic impedance vs. Vp/Vs, impedance interpretation seems to give us a lot more information about lithology and fluids than the conventional seismic interpretation that images boundaries. With impedance technology we are able to detect geological trends that will aid in seismic interpretation.
- Of all the parameters use in modelling our reservoir, Vp/Vs seems to be more reliable in discriminating fluids and lithology. This study confirms that it is a very useful tool for this purpose.
- Vp versus Vs also shows a good degree of fluid discrimination but would not be sufficient for final interpretation.
- The higher the rock bulk modulus relative to the shear modulus, the higher the Vp/Vs ratio. Hence, the shale line plots at higher ratios. This means that for the same lithology substituted with different fluids, the fluids with higher bulk modulus plot at higher Vp/Vs ratios. Hence the gas sands are lower than the oil sands, and the oil sands are lower than the brine sands.
- For different lithologies of the same fluid, the shalier lithology will plot at relatively higher Poisson's ratio than the sandier lithology.
- Increase in cement within sandstones reduces the sensitivity of fluids and very much reduces the effect of effective pressure on velocities as cementation fills up the pores between the mineral grains.
- Understanding rock physics trends is vital for a proper analysis of AVO signatures as they would very much affect AVO signatures which may lead to misinterpretation of data and wrong decision-making.

- The trends observed can be used as a guide during seismic interpretation as failure to understand these trends could be a pitfall in interpretation.
- The use of RPT's such as impedance versus Vp/Vs proved to be very reliable as we could interpret features which were not very clear during cross-plot analysis. Impedance interpretation therefore has an edge over conventional seismic interpretation that images boundaries while the former images layers.

RECOMMENDATION

Following this study, we would recommend that more detail AVO analysis should be carried out in the same area and use these results with those of AVO analysis. We also recommend study of other wells that could not be covered during this study to better understand the mineralogical composition of the whole area.

ACKNOWLEDGEMENTS

I would like to give special thanks to my supervisor, Dr. Per Avseth, for his guidance during this study and for the attention he has given me during this period. I appreciate every iota of time he put into the realization of my studies. I also thank the Norwegian University of Science and Technology administration for giving me the opportunity to further my studies abroad. It has been a great time studying in 'The place to be!'

Thanks also go to my family, the Taju's and the Malafa family for the support they gave me and the love they have always shown me which has driven through to the end of these 2 years of studies.

Last but not least, I thank my special friends, Samuel Malafa and Anja Michel.

REFERENCES

Avseth, P., Mukerji, T., and Mavko, G., 2005. Quantitative Seismic Interpretation: Applying Rock Physics Tools to Reduce Interpretation Risk.

Avseth, P., Dvorkin, J., Mavko, G., and J. Rykke, 1999. Rock Physics Diagnostics of North Sea Sands: Link Between Microstructure and Seismic Properties.

Avseth, P., Dvorkin, J., Mavko, G., and J. Rykke, 1999. Diagnosing High-Porosity Sands for Reservoir Characterization Using Sonic and Seismic. SEG 66 Annual Meeting, Expanded Abstracts, 1024 – 1025.

Avseth, P., Jørstad, A., Wijngaarden, A.J., and Mavko, G., 2009. Rock Physics Estimation of Cement Volume, Sorting, and Net-to-gross in North Sea Sandstones, Special Edition. Rock Physics, The Leadiing Edge.

Bachrach, R. and Avseth, P. 2008. Rock Physics Modeling of Unconsolidated Sands: Accounting for Nonuniform Contacts and Heterogeneous Stress Fields in the Effective Media Approximation with Applications to Hydrocarbon Exploration.

Dvorkin, J., and Nur, A., 1996. Elasticity of High Porosity Sandstones: Theory for Two North Sea Datasets. Geophysics, 61, 1363 – 1370.

Dvorkin, J., and Nur, A., 2000. Critical Porosity Models. Department of Geophysics, Stanford University, Stanford, CA 94305 – 2215.

Han, D., 1986. Effects of Porosity and Clay Content on Acoustic Properties of Sandstones and Unconsolidated Sediments. Ph.D. dissertation, Stanford University.

Smith, T. M., 2011. Practical Seismic Petrophysics: The Effective Use of Log Data for Seismic Analysis. *The Leading Edge*, **30,** 1128 – 1141

Norwegian Petroleum Directorate (npd.no)

APPENDIX

Computing volume of shale:

$$V_{sh}(linear) = A = \frac{GR_{\log} - GR_{\min}}{GR_{\max} - GR_{\min}}$$

where $GR_{\log}$ =the gamma ray log,

$GR_{\min}$ =minimum gamma ray reading within reservoir (assumed sand),

$GR_{\max}$ =maximum gamma ray reading within the reservoir (clayey zone).

$$V_{sh\_Tert}(non-linear) = 0.083*(2^{3.7A} - 1)$$

Converting slowness (DTCO and DTSM) to velocities (km/s):

Vp=304.8/DTCO; Vs=304.8/DTSM.

Matlab code

```
function result = Cem(varargin)
%function result = Cem(Phic,C,Gs,nus,Gc,nuC,Kf,scheme)
%Calculates the water-saturated elastic moduli versus porosity
lines
%using Dvorkin's contact cement model
%Inputs are by input dialog box, if called without input
arguments.
%     PhiC: critical porosity
%     C:    coordination number
%     Gs:   grain shear modulus
%     nus:  grain Poisson's ratio
%     Gc:   cement shear modulus
%     nuC:  cement Poisson's ratio
%     Kf:   fluid bulk modulus
%     scheme: (1 or 2) Cementation scheme 1: cement at
contact, 2: on surface
%Outputs returned in result matrix.
%result=[porosity, M-modulus, shear-modulus];
%Plots effective moduli vs. porosity when called with no
output arguments.


%Written by Jack Dvorkin
%I/O modifications, Tapan Mukerji, 6/1999.
%ref. Dvorkin & Nur, 1996, Geophysics, 61, 1363-1370
```

```
%     Rock Physics Handbook, section 5.2

prompt={'PhiC','Coord.#','Gs (GPa)','Nus','Gc (GPa)','Nuc','Kf
(GPa)','Cem. Scheme (1 or 2)' };
defans={'.38','8.5','45','.064','45','0.064','0.','2'};

if nargin==0
getpar=inputdlg(prompt,'Contact Cement Model',1,defans);
for k=1:length(getpar), param(k)=str2num(getpar{k}); end;
PhiC=param(1); C=param(2); G=param(3); nu=param(4);
Gc=param(5); nuC=param(6);
Kf=param(7); schopt=param(8);
else
PhiC=varargin{1}; C=varargin{2}; G=varargin{3};
nu=varargin{4};
Gc=varargin{5}; nuC=varargin{6}; Kf=varargin{7};
schopt=varargin{8};
end;
format short

K = G.*2.*(1.+nu)./(3.*(1.-2.*nu));
Kc = Gc.*2.*(1.+nuC)./(3.*(1.-2.*nuC));
%Porosity loop Cement
i = (1:100)';
      Phi0 = PhiC-(i-1).*(PhiC-0.15)./100;
%Fraction of cement in the rock
      fc = PhiC-Phi0;
%Fraction of grain in the solid
      fgs = (1-PhiC)./(1-Phi0);
%Fraction of cement in the solid
      fcs = (PhiC-Phi0)./(1-Phi0);
%Bulk modulus of the solid
      Ks = (fgs.*K+fcs.*Kc+1./(fgs./K+fcs./Kc))./2;
%Shear modulus of the solid
      Gs = (fgs.*G+fcs.*Gc+1./(fgs./G+fcs./Gc))./2;
%M-modulus of the solid
      Ms = Ks+4.*Gs./3.;
%Kframe and Gframe at Phi=Phi0, Cementation Scheme 1
      if schopt==1
      a = 2.*(((PhiC-Phi0)./(3.*C.*(1.-PhiC))).^0.25);
      end;
%Cementation Scheme 2
      if schopt==2
      a = sqrt((2.*(PhiC-Phi0))./(3.*(1.-PhiC)));
      end;
%Capital Lambdas
      alam = (2./3.14).*(Gc./G).*(1.-nu).*(1.-nuC)./(1.-
2.*nuC);
      alamtau = (1./3.14).*(Gc./G);
%Effective bulk modulus
      r1 = Kc+4.*Gc./3;
```

```
      r2 = C.*(1.-PhiC)./6;
      r3 = -0.024153.*(alam.^(-
1.3646)).*(a.^2)+0.20405.*(alam.^(-
0.89008)).*a+0.00024649.*(alam.^(-1.9864));
      Kframe = r1.*r2.*r3;
%Effective shear modulus
      r1 = Gc;
      r2 = 3.*C.*(1.-PhiC)./20;
      a1t = -0.01.*(2.2606.*nu.*nu+2.0696.*nu+2.2952);
      a2t = 0.079011.*nu.*nu+0.17539.*nu-1.3418;
      b1t = 0.05728.*nu.*nu+0.09367.*nu+0.20162;
      b2t = 0.027425.*nu.*nu+0.052859.*nu-0.87653;
      c1t = 0.0001.*(9.6544.*nu.*nu+4.9445.*nu+3.1008);
      c2t = 0.018667.*nu.*nu+0.4011.*nu-1.8186;
      r3 =
(a1t.*(alamtau.^a2t)).*a.*a+(b1t.*(alamtau.^b2t)).*a+c1t.*(ala
mtau.^c2t);
      Gframe = 0.6.*Kframe + r1.*r2.*r3;
      Mframe = Kframe+4.*Gframe./3;
%Gassmann
      Ksat = Ks.*(Phi0.*Kframe-
(1+Phi0).*Kf.*Kframe./Ks+Kf)./((1-Phi0).*Kf+Phi0.*Ks-
Kf.*Kframe./Ks);
      Msat = Ksat+4.*Gframe./3;
      nuSat = 0.5.*(Msat./Gframe-2)./(Msat./Gframe-1);
      VpVs = (Msat./Gframe).^0.5;
      Msat2 = Ms.*(Phi0.*Mframe-
(1+Phi0).*Kf.*Mframe./Ms+Kf)./((1-Phi0).*Kf+Phi0.*Ms-
Kf.*Mframe./Ms);

if nargout==0
subplot(1,2,1)
plot(Phi0,Msat,'r-')
axis([0.1 0.4 0 45])
set(gca,'fontname','bookman','fontsize',9)
xlabel('Porosity','fontname','bookman','fontsize',11)
ylabel('M-Modulus (GPa)','fontname','bookman','fontsize',11)
hold on
subplot(1,2,2)
plot(Phi0,Gframe,'r-')
axis([0.1 0.4 0 20])
set(gca,'fontname','bookman','fontsize',9)
xlabel('Porosity','fontname','bookman','fontsize',11)
ylabel('G-Modulus (GPa)','fontname','bookman','fontsize',11)
hold on
end;
result=[Phi0 Msat Gframe];
```